

UNIVERSITÀ DI PISA

FACOLTÀ DI SCIENZE MATEMATICHE FISICHE E NATURALI

CORSO DI LAUREA SPECIALISTICA IN SCIENZE FISICHE

ANNO ACCADEMICO 2009 – 2010

TESI DI LAUREA SPECIALISTICA

**Validation study of the online signal
reconstruction in the ATLAS
hadronic Tile Calorimeter**

Candidato:
Federico BERTOLUCCI

Relatrice:
Dr.ssa Chiara RODA

Contents

1	Overview	3
1.1	Physics motivation of the Large Hadron Collider and ATLAS	3
1.2	The Large Hadron Collider	7
1.3	Experimental environment and detector constraints	11
1.4	The ATLAS experiment	13
1.4.1	Detector description	14
1.4.2	Trigger and data acquisition system	16
2	Basic concepts of calorimetry	19
2.1	Calorimetry overview	19
2.2	Electromagnetic showers	21
2.3	Hadronic showers	24
2.4	Linearity and energy resolution	25
2.5	Calorimeter segmentation and hermeticity	26
3	The Tile Calorimeter design	29
3.1	Tile Calorimeter layout	29
3.1.1	TileCal basic requirements	30
3.1.2	TileCal environment	31
3.2	TileCal mechanics and optics	32
3.3	TileCal front-end electronics	34
3.3.1	PMT blocks	35
3.3.2	Motherboards	37
3.3.3	Digitizer card	37
3.4	TileCal back-end electronics	38
3.4.1	The Read Out Driver boards	38
3.5	TileCal calibration methods	39
3.5.1	The Charge Injection System	40
3.6	TileCal synchronization	43
3.7	TileCal signal generation	45
3.7.1	Physics signal	45
3.7.2	CIS signal	46
3.8	Noise and time structure of TileCal signals	47

4	The Optimal Filtering method	49
4.1	The Optimal Filtering signal reconstruction	49
4.1.1	Physical requirements of Optimal Filtering	49
4.1.2	Optimal Filtering weight calculations	52
4.2	Signal reconstruction methods in TileCal	55
4.3	The Calibration Constants	59
5	Validation study	61
5.1	Conditions and data used in the analysis	61
5.2	Online and offline reconstruction	62
5.3	Fit linearity and resolution	66
5.4	Comparison between amplitudes	69
5.4.1	Understanding the CIS behavior	70
5.4.2	The reverse correction	72
5.5	Systematics	74
6	A proposal to monitor the time setting	79
6.1	Timing behavior	79
6.2	The Timing Monitor for TileCal	84
6.2.1	Quantification of TileCal timing stability	86
6.3	The Time-Line Monitor	88
7	Conclusions	91
	Appendices	93
A	Precision errors due to digit truncation	93

Preamble

The Large Hadron Collider (LHC) that is operating at the CERN laboratory is a proton-proton collider that will provide one bunch collision each 25 ns at a nominal center-of-mass energy of 14 TeV and at a peak luminosity of $10^{34} \text{ cm}^{-2}\text{s}^{-1}$. These conditions allow to investigate the Standard Model predictions and to test many critical areas like the Higgs Boson mechanism in the framework of a wide range of scenarios.

Currently the LHC is being tuned and produces collisions at $\sqrt{s} = 7 \text{ TeV}$ with a luminosity of about $10^{31} \text{ cm}^{-2}\text{s}^{-1}$.

The optimal experimental conditions for discovery searches however impose severe constraints on the detector structures, electronics and performances in order to cope with the huge amount of data and to be able to select the interesting events with reasonable precision at the Bunch Crossing frequency of 40 MHz.

ATLAS is a detector situated on the LHC ring. This thesis deals with its central hadronic calorimeter, TileCal, which is a sampling calorimeter with steel as absorber material and plastic scintillator tiles as active medium; groups of tiles and steel plates form the TileCal cells. The cells are coupled to wave-length-shifter fibers, which transport the scintillation light to two photomultipliers. The output signals are then properly shaped and digitized by the front-end electronics, which is composed of about 10000 channels. The Tile Calorimeter is complemented by a triple calibration system that allows equalization and monitoring of the signal at various stages.

Up to now (October 2010), being the acquisition rate low enough to allow to output the full digital information, the standard method for the TileCal signal reconstruction is an offline iterative Fit method. With increasing luminosity this will no longer be true and a fast signal reconstruction will be performed to propagate only the signal time and amplitude in order to minimize the information to be transmitted.

A dedicated algorithm, the Non-Iterative Optimal Filtering method (OF-NI), is executed in Digital Signal Processors and is responsible for the on-line reconstruction of the signal time and amplitude. The reconstruction rate for the whole calorimeter must cope with the Level 1 Trigger output rate of 100 kHz. This is far from a simple effort due the large amount of background events.

In this thesis the focus is on validation aspects of the OF-NI reconstruction for the TileCal signal, mainly using data provided by a Charge Injection System and preliminary analysis of the signal reconstruction in proton-proton collisions.

It will be shown that a good understanding of both the hardware and the algorithm implementation is required in order to validate the reconstruction and to evaluate the systematics induced on the signal amplitude and time.

In the last part of the thesis a timing monitor is presented which allows to control the stability and the performances of the signal reconstruction.

This work is part of the contribution to the TILE SIGNAL RECONSTRUCTION AND VALIDATION TASK FORCE, a group dedicated to the validation of the on-line signal reconstruction in TileCal.

Chapter 1

Overview

The Standard Model currently provides the best theoretical description of the elementary particles and their interactions. It has been carefully verified in the last 40 years by many experiments and its basis rest on well trusted theories.

However the Standard Model fails in the descriptions and previsions of some critical points and does not furnish any mechanism or justifications for particle masses. This last problem had been solved with the hypothesis of the existence of a new particle, the Higgs boson in the Standard Model, responsible for all particle masses. The LHC had been build to verify the Higgs existence and to search for new Physics at an energy scale never probed before.

The required luminosity and energy drive the detector design to be ready to investigate the possible scenarios through different channels. Experimentally the different investigated channels are affected by different backgrounds depending on the physical processes under study and on the detector characteristics (performances, resolution, mis-calibrations, systematics. . .) which have to be studied, understood and controlled.

1.1 Physics motivation of the Large Hadron Collider and ATLAS

The Standard Model [1; 2] is the best theory we have at the present to describe the structureless constituents of matter, the elementary particles, and their interactions. Elementary particles are divided in leptons and quarks (fermions) whose interaction is mediated by gauge bosons (photons, W, Z and gluons). The Standard Model has been tested and its predictions have been verified at the precision level of 0.1% or better with data produced by the accelerators LEP, SLC and Tevatron [10; 3]. Nonetheless some important issues such as the origin of the mass, the nature of the dark matter and the need of a complete theory for all force unification still have no answer. The search for a justification for the origin of the mass, and in general for the mass hierarchy of leptons, quarks and gauge bosons, was one of the leading motivations that have driven the LHC and ATLAS design.

The Higgs mechanism, based on spontaneous electroweak symmetry breaking, introduces in the Standard Model the mass terms without spoiling the gauge invari-

ance that constitutes the foundation of the theory. The interaction of fermions and bosons with the Higgs field generates the particle masses, which depend on the coupling constants between the fields. This mechanism should be experimentally proved by the presence of a new neutral boson particle, the Higgs boson.

The Standard Model does not predict the mass of the Higgs boson, nor its coupling with the other fields, however it allows to calculate the decay widths and the production cross sections as functions of its unknown mass.

In general the Higgs partial decay widths increase as the masses of the final state particles increase, within the constraints of the available phase space. Its decay width to fermion pairs is proportional to the fermion mass squared:

$$\Gamma(H \rightarrow ff) \propto m_f^2 \beta^3 m_H$$

while the decay width in two vector bosons is:

$$\Gamma(H \rightarrow VV) \propto m_H^3$$

The Higgs branching ratios for various decay channels, as a function of its mass, are shown in Figure 1.1 for $\sqrt{s} = 7$ TeV: for $m_H < 140$ GeV, the largest branching ratios are those into two fermions, while at higher energies the decays into vector bosons have dominant BR.

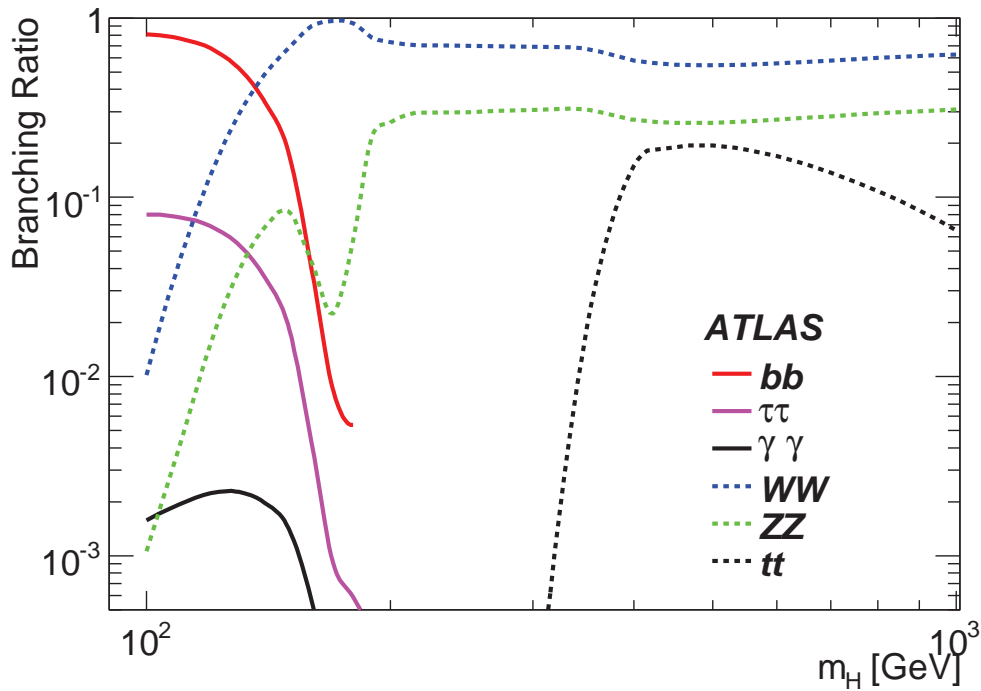


Figure 1.1: Higgs decay channels as a function of a Higgs mass between 100 GeV and 1 TeV. The relative contributions change with the Higgs mass, therefore also the signatures and the backgrounds are different.

The current limits on the Higgs mass have been obtained both from indirect and direct searches. Indirect experimental bounds to the Higgs mass are obtained

from fits to precision measurements of electroweak observables, sensitive to the Higgs mass. As an example, the Higgs boson contributes to the W , Z and top quark masses through loop corrections, hence they depend on m_H . The fit to the experimental results collected mainly at LEP, Tevatron and SLC, including also the top quark mass measurement, sets an upper limit of $m_H < 186$ GeV at 95% CL.

The current limits set by direct searches on the Higgs mass obtained combining the results from Tevatron and LEP experiments are shown in Figure 1.2 [4]. The 95% Confidence Limit on the Higgs cross section production, normalized to the Standard Model expectations, is shown as a function of the Higgs mass for the Tevatron experiments at an integrated luminosity of ~ 6 fb $^{-1}$.

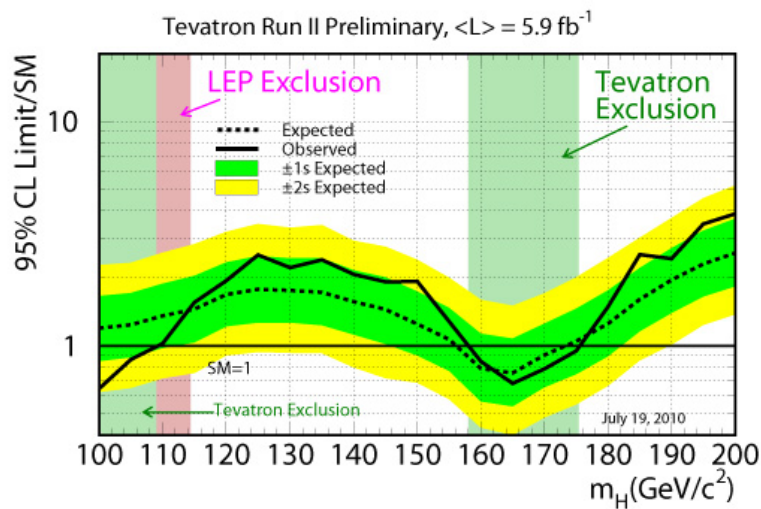


Figure 1.2: Higgs exclusion regions combining results from Tevatron and LEP experiments. The exclusions are consistent with the absence of signals from various channels.

The two mass regions excluded by LEP and Tevatron analysis are shown as vertical bands in the plot.

LHC and ATLAS have been designed to give a definitive answer to the Higgs boson hypothesis.

Figure 1.3 shows the most important production channels for the Higgs particle as a function of its mass, in the range from 100 GeV to 1 TeV, for proton-proton collisions at $\sqrt{s} = 7$ TeV.

The gluon fusion process is the most probable production process in the whole energy range, and, together with the Higgs decay in a couple of Z , it provides spectacular signatures of four leptons in the final state for Higgs masses larger than 200 GeV.

At lower masses, the analysis strategy is not so clear, since there is not a unique clean signature for the Higgs; the best sensitivity is obtained by using many different

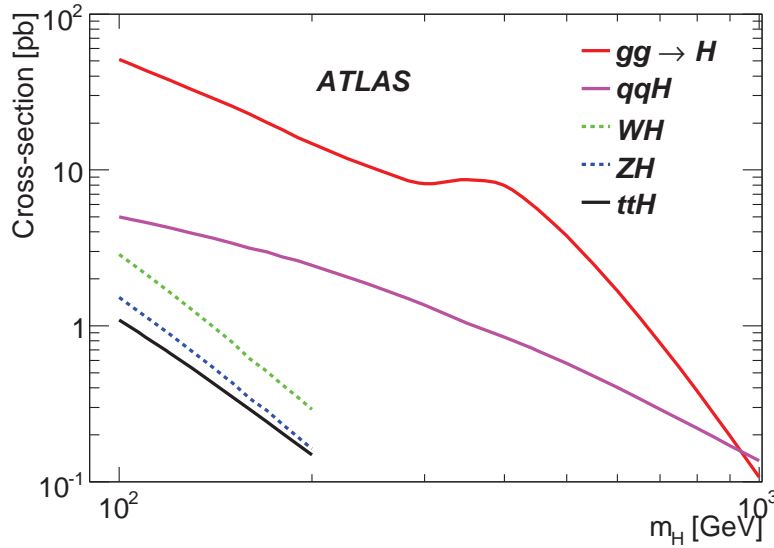


Figure 1.3: Higgs production channels as a function of a possible Higgs mass between 100 GeV and 1 TeV. The most important channels for what concern the detection are the associated Higgs production; the gluon fusion process is flawed due to the difficult tagging.

production and decay processes each contributing in a particular range of masses. The potential of Higgs discovery in a definite region depends both on the Higgs branching ratios and on the ability to reject the background. For example, the $H \rightarrow b\bar{b}$ decay, favoured at low masses, is not usable since it is overwhelmed by the huge QCD background. This situation is summarized in Figure 1.4. In these plots the expected significance for Higgs discovery for various topologies and for combined analysis is shown as a function of the Higgs mass for an integrated luminosity of 10 fb^{-1} .

The shown sensitivity plots are the result of detailed analysis that have been performed in the last ten years to determine the best signatures to be experimentally searched for, in the various Higgs mass ranges. They all rely on very good detector performances that can be summarized by the following requirements:

- good vertexing capabilities for b -tagging and τ -tagging;
- very good calorimetric resolution, both in the electromagnetic ($H \rightarrow \gamma\gamma$) and in the hadronic (efficient jet reconstruction) sectors;
- very precise lepton identification and momentum measurements.
- almost complete calorimetric coverage for E_T^{miss} detection;

The LHC and detector performances will be illustrated in the next Sections.

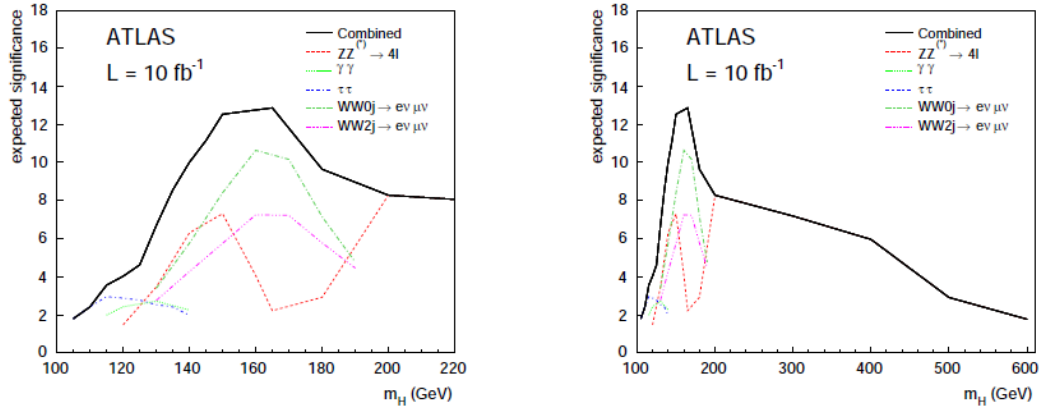


Figure 1.4: Expected discovery significance for various channels in the ATLAS experiment with 10 fb^{-1} of collected data as a function of the Higgs mass. The coloured lines refer to the different channels, the black line is the combined sensitivity. On the left: sensitivity in the low-mass region; plot on the right: Higgs masses up to 600 GeV. Between 150 GeV and 180 GeV the most promising channel is the Higgs decay in two photons; at higher masses the contribution of the Higgs decay in a couple of Z tagged by 4 leptons is dominant.

1.2 The Large Hadron Collider

The Large Hadron Collider (LHC) [5] at CERN is a superconducting synchrotron in which beams of protons or heavy ions collide in four points, corresponding to the positions of four different detectors. Figure 1.5 is a summary layout of the accelerator systems and shows the positions of the various detectors: particles are accelerated up to 450 GeV and then are injected into the LHC. In counterclock order, the four experiments are ALICE, CMS, LHC-B and ATLAS. The detector frames are the rest frames for the collisions, so that the center of mass energy is proportional to the incoming particle energies. A selection of the LHC design parameters are listed on Table 1.1. Since LHC has been installed in the 27 km LEP tunnel, the limiting

LHC parameters	$p - p$
beam energy [TeV]	7
center of mass energy [TeV]	14
bunch frequency [Hz]	$4 \cdot 10^8$
low luminosity [$\text{cm}^{-2}\text{s}^{-1}$]	10^{33}
high luminosity [$\text{cm}^{-2}\text{s}^{-1}$]	10^{34}
luminosity lifetime [h]	10
magnetic field [Tesla]	8.2

Table 1.1: A selection of the LHC parameters; value are intended to be the project ones.

factor to the achievable center of mass energy is the bending power needed to keep the beams on the correct orbits. This point is well understood by means of the

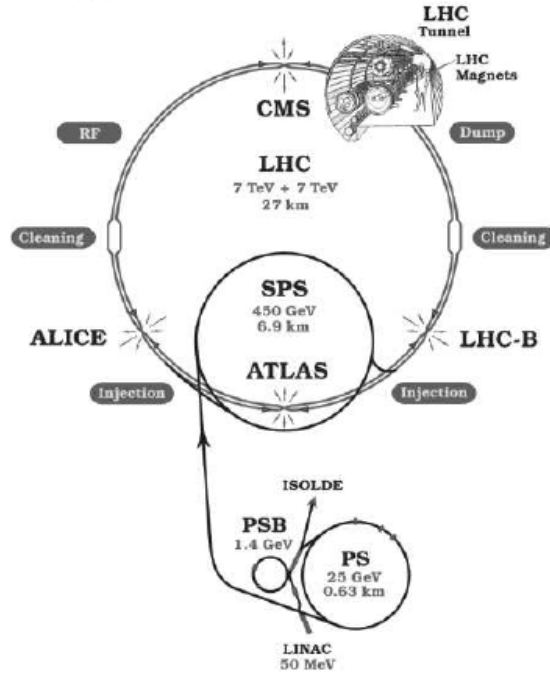


Figure 1.5: Schematic LHC layout; four experiments are installed in correspondence of four collision points.

Lorentz force for unit charged particles, $p[\text{TeV}] = 0.3B[\text{Tesla}] \cdot \rho[\text{Km}]$, where p is the beam momentum, B the magnetic field and ρ is the radius of curvature. In order to achieve a beam momentum of 7 TeV, the bending field is about 5.4 Tesla, in case the LHC could be completely filled with magnets along its circumference. Since this is not the case, the required bending power is achieved by using 8.2 Tesla magnetic fields. Such intense fields have been a technical challenge, and the adopted solution is based on superconducting magnets.

The number of interactions with given initial and final states is proportional to the probability for the single process to happen, to the number of initial states available and to the integration time of the measurement; therefore, the rate of a process is proportional to a parameter that depends on the Physics process involved, and to another one which determines how often the conditions for this process to happen are produced. These two quantities are respectively the process cross section and the machine luminosity, and the main goal of LHC is to provide bunches¹ of particles colliding at high luminosity and high energy.

The luminosity is defined as the physical measurement of the density of colliding centres for unitary incoming projectile flux, therefore it is proportional to the number of particles in each bunch (n_1 and n_2), to the number of bunches (b) and to the revolution frequency (ν), and it is inversely proportional to the beam effective surfaces (σ_x and σ_y): $L = \frac{n_1 n_2}{4\pi\sigma_x\sigma_y} b\nu$. The luminosity is measured in picobarn⁻¹ sec⁻¹ or

¹The word *bunch* refers to the phase space available for acceleration: particles which are in a wrong position with a wrong momentum when entering a Radio Frequency cavity are most likely lost[6].

$\text{cm}^{-2} \text{sec}^{-1}$ units. The higher the luminosity, the larger the number of interactions at a given time. Therefore a high luminosity is one of the necessary ingredients for the experiments that aim to study rare events.

On the other hand, the probability for a process to happen is measured by its cross section². The cross section is a measurement of the number of processes from the initial state to the final state occurring for unit incoming particle flux. It is composed by two contributions: one is the probability of transition from the initial state to the final state dictated by the dynamics of the involved interactions; the second is the phase space density for the final products, that counts the number of available phase space configurations for the same initial states under the hypothesis of energy and momentum conservation. Thus, the cross section is a complete characterization of the physical processes; classically it reduces to the effective surface for a collision to take place, and it is measured in units of barn or its submultiples. When the energy increases, new phenomena may appear or become dominant, and others can be suppressed, so that new interactions are possible, or new particles are created. This is usually said as *a given channel opens or closes at a given energy*. New channels may therefore open at energies not yet investigated, giving the possibility of studying new phenomena foreseen by the Standard Model or by new theories such as SuperSymmetry.

The design luminosity will be reached after a so called *low luminosity* period, while the nominal center of mass energy will be achieved as soon as a final upgrade needed to assure the best beam control will be in place. Currently the LHC is running at $\sqrt{s} = 7$ TeV with a peak luminosity of $\sim 10^{31} \text{ cm}^{-1}\text{s}^{-1}$ (Figure 1.6). If the delivered luminosity is integrated over the time the result is called *integrated luminosity*, and it is used as an estimate of bunch delivered by the collider to the experiments. Figure 1.7 shows the integrated luminosity from the end of March 2010 until the end of September 2010. The integrated luminosity dimensions are $[L^{-2}]$ and its values are usually reported as pb^{-1} . Currently, the LHC has delivered about 6.90 pb^{-1} .

The choice of protons as colliding objects inside the LHC has been driven both by Physics motivations and by technical problematics.

From the point of view of Engineering, it would be impossible to build a synchrotron with such high energies and luminosities using electrons as interacting particles because of the costs and of the required technology. Due to the fact that accelerated charges lose their energy by means of the emission of synchrotron light, the energy lost in unit time is proportional to the particle squared charge and to its squared acceleration module: $\frac{dE}{dt} \propto \frac{q^2}{m^2} \left| \frac{d\vec{p}}{dt} \right|^2$ (see [7] for a derivation), where E , q , m and p denote respectively the energy, the charge, the rest mass and the momentum of the particle. The energy lost during a single lap per particle in a circular orbit is $\delta E \propto e^2 \cdot \frac{E^4}{m^4 \rho^2}$: if energy is fixed, electrons lose $1.6 \cdot 10^{12}$ times the energy lost by protons.

Another subtle point is the vacuum system performance. Describing the residual gas in the pipe as a perfect gas and denoting with σ the cross section for some inter-

²Strictly speaking, in the case of decay the involved quantity is the decay width, for which the definition is slightly different. In the following the stress is upon the cross section, but the point is the same: cross sections and decay widths are physical quantities that characterize completely and unambiguously the processes they refer to.

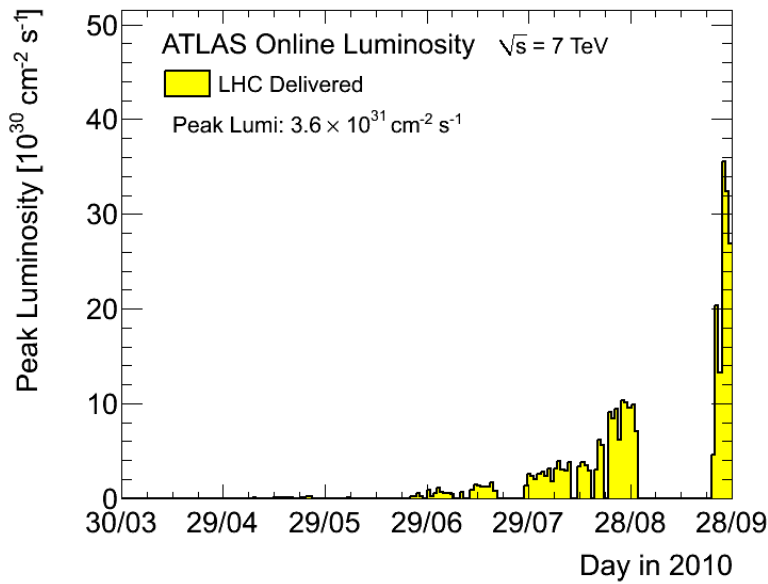


Figure 1.6: LHC peak luminosity as a function of time, from end of March 2010, recorded by the ATLAS experiment. Current peak luminosity is about $\sim 3.5 \times 10^{31} \text{ cm}^{-2} \text{ s}^{-1}$

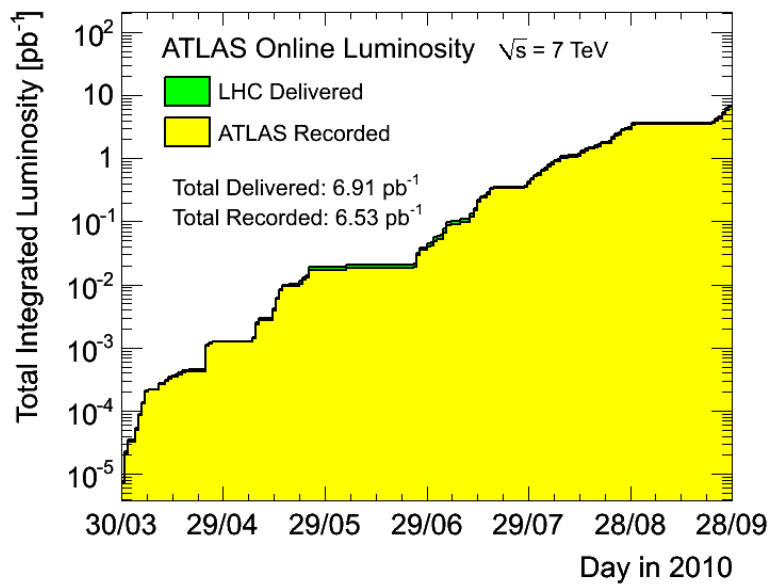


Figure 1.7: LHC integrated luminosity as a function of time, from end of March 2010. The green histogram refers to the integrated luminosity delivered by LHC, the yellow one to the integrated luminosity recorded by the ATLAS experiment.

action between the beam particles and the gas, the beam mean lifetime is inversely proportional to the cross section multiplied by the gas density; thus the pressure

inside the beam pipe should be smaller than some critical value: $P \lesssim \frac{0.47 \cdot T [^\circ K]}{\tau [hour] \cdot \sigma [barn]}$ [6]; since it is reasonable to have a beam mean lifetime of the order of 10 – 20 hours, it turns out that in case of proton beams (σ is in this case σ_{strong}) the pressure is of the order of 1 nanoTorr (1 *torr* $\sim 10^{-3}$ *atm*).

In the case of electron beams, the gas density is not constant if measured in a time comparable to the average beam lifetime, since a large number of electrons and positrons are radiated and created in subsequent electromagnetic processes. The electron cloud moves within the pipe following and degrading the beam³.

For what concern the Physics, electron-positron annihilations or even lepton-hadron processes offer for sure a cleaner environment than hadron-hadron collisions. In electron-positron colliders, the center-of-mass energy of the interaction corresponds to the center of mass energy of the machine; protons instead are non-elementary particles, hence at hadron colliders the available energy for the interaction is smaller than \sqrt{s} . The interactions are between partons inside hadrons, and each parton carries a fraction of the total hadron momentum. This fraction follows a so-called parton distribution function, thus it is not possible to know the exact center of mass energy of each interaction.

The advantages of hadron-hadron colliders⁴ rely undoubtedly on the wide variety of the final states. Most events at the LHC are due to small transferred momentum for the interacting partons and large angle scattering is suppressed. These collisions are called *soft*. The collisions characterized by a large transferred momentum are called *hard* collisions and imply that a deep interaction has undergone between partons. Hard scattering events are the most interesting, since at very short distances the proton constituents could exchange or produce heavy particles. At the LHC energies, these masses may be of the order of a hundred GeV.

1.3 Experimental environment and detector constraints

The experiments positioned along the LHC ring have to cope with many difficulties. The problems are related to the machine luminosity and to the intrinsic nature of the proton-proton collisions at such high energy. The results are specific-designed detectors.

First of all, the most probable events at the LHC are soft collisions, in which a large part of energy in the final states is lost along the beam pipe. This implies a very high radiation rate, especially for detectors close to the beam pipe. The technical solution has been sufficiently radiation resistant detectors to be placed close to the beam pipe.

Figure 1.8 shows the production cross sections for some final state in proton-proton collisions as a function of the center-of-mass energy. It can be seen that at

³The gas density is then the sum of the initial density (no electron cloud) and the contribution of the electron cloud, which in its turn is proportional to the probability for a particular process to happen multiplied by the number of initial states, that is, multiplied by the number of electrons: $n_{eff} = n_0 + a \cdot N_e$. The gas density increases linearly with the number of electrons, thus the vacuum system is much more complex, problematic and expensive when dealing with electrons rather than with protons with the same energy.

⁴The difference between particle-particle and particle-antiparticle colliders is mainly in the production and in the beam maintenance mechanisms. The LHC are technically two colliders which share the same set of magnets.

$\sqrt{s} = 7$ TeV the cross section for Higgs signals is of the order of a picobarn or even less. It is therefore clear the need for a very high luminosity that allows to produce a large number of interesting events which could exclude or confirm the existence of a particular signal.

The requested high luminosity of the LHC design poses a further complication since at a center of mass energy of 14 TeV the total inelastic cross section is about 70 mb. When running at high luminosity, each bunch crossing at the LHC generates about 25 soft interactions. This means that each detector measures simultaneously the signals of soft and hard scatterings; the overlapping of events is called *pile-up*, and the higher the luminosity, the more important is the pile-up contribution to the signal.

The described pile-up is defined *in-time* pile-up, because it occurs during the same bunch crossing; if events from different bunch crossings overlap, the effect is called *out-of-time* pile-up.

Pile-up is a serious background to the interesting events, and detectors can cope with it mainly with two expedients. The first one is the fast response of devices, in order to limit the number of bunch crossing collisions whose events are integrated. The second solution is the design of high-granularity detectors, in order to be able to recognize particles produced by different collisions. This in its turn results in very large event dimensions for data processing and storing, and in delicate calibrations and maintenance work.

A second problem caused by the very high luminosity and by the nature of the proton-proton collisions is the very high interaction rate to be handled. As previously stated, the total proton-proton inelastic cross section is about 70 mb, mainly consisting of QCD jet production. The cross section ratio between typical discovery signals and background is about 10^{12} . It is therefore clear that a very fast and efficient trigger selection is a necessary ingredient to cope with the high event rate and low signal-to-background ratio. Moreover QCD jet production remains the most important background to all the physics searches, there is therefore no hope to detect rare events for which detectable final states are only jets; it is needed at least a non-QCD final states, that is, finally, at least one detectable lepton in the final state. The example of the W particle is very helpful to understand this point. The most probable decay mode for W according to [8] is into hadrons ($\Gamma_h/\Gamma \simeq 68\%$); in the LHC environment it is almost impossible to detect the W production isolating a $W \rightarrow jj$ sample of events, due to the huge QCD background ($\sigma_{jj} \approx 10^5 \sigma_W$, see Figure 1.8). The interesting channel at the LHC is represented by $W \rightarrow l\nu$, where l is a lepton and ν its corresponding neutrino. The relative width for this decay channel is about 10%, thus the detectable W events at the LHC are largely reduced because of QCD background. Generalizing from the example above, since QCD jet production dominates over the rare searches processes, Physics analysis must be provided with the possibility to have stringent lepton/photon identification and precise measurement of missing transverse energy and secondary vertexes.

In other words, the QCD background forces the detector structures to be hermetic and to provide very precise energy measurements.

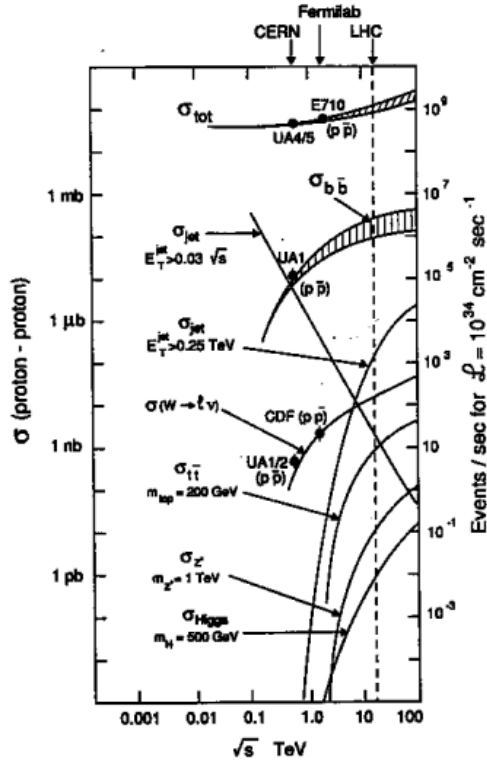


Figure 1.8: $p - p$ cross sections for various final states as a function of the center of mass energy; on the vertical axis, left, cross section values; right, the number of events per second calculated assuming a $10^{34} \text{ cm}^{-2} \text{ s}^{-1}$ luminosity.

1.4 The ATLAS experiment

ATLAS (a pun for *A Toroidal LHC Apparatus*, [11; 12]) is one of the four experiments approved to run at the LHC, and it has been designed to be a *general-purpose* detector, meaning it should be versatile enough to detect Physics signals with a wide range of signatures.

The ATLAS experiment is housed in a hall about 100 metres underground, in correspondence of the LHC ring; the detector reference system is a cylindrical system with the z -axis coincident with the beam direction; the ϕ axial angle is the angle between the z -axis and the particle direction; the θ angle is measured from $z = 0$ is the θ angle, positive for positive z .

At collider experiments it is quite common to introduce the pseudorapidity variable η in place of θ . The pseudorapidity is related to θ as $\eta = -\ln[\tan(\theta/2)]$, but it is more useful since it approximates the rapidity when it is possible to neglect the mass with respect to the energy.

1.4.1 Detector description

The ATLAS detector is divided in three longitudinal regions, one is central, the other two lateral; sub-detectors in the central part are named with the *Barrel*-prefix, the others with the *Extended Barrel* or *End-Cap* prefixes. In Figure 1.9 ATLAS and its sub-detectors are depicted: in the central part, near the beam line, is housed the most internal sub-system, the tracker, embedded into the solenoidal magnetic field; the solenoid is the structure around the tracker and holds the electromagnetic

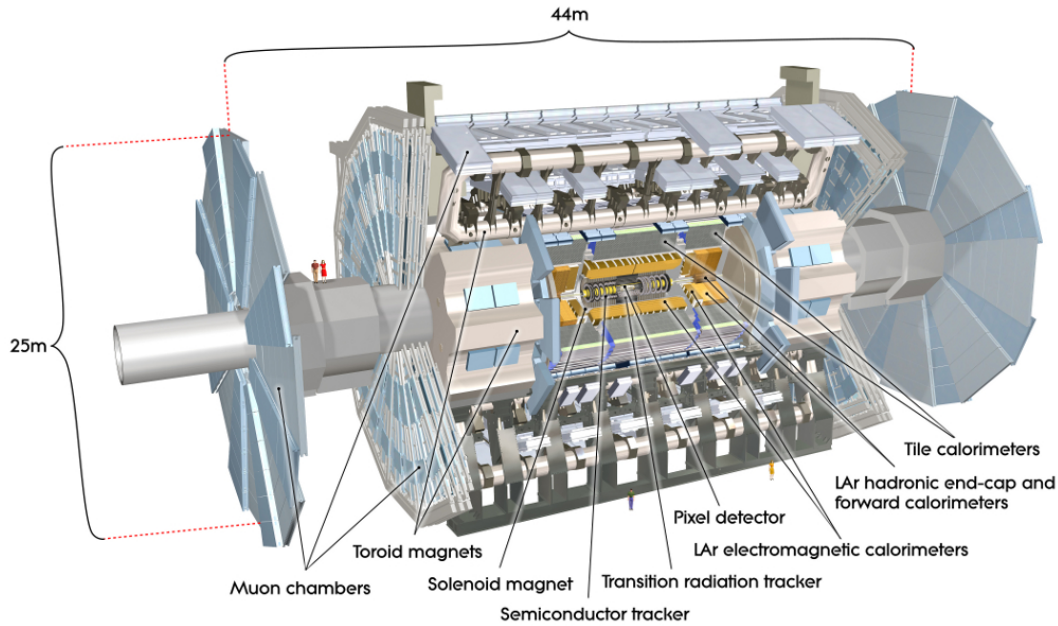


Figure 1.9: schematic Atlas layout; the main subdetectors are depicted.

calorimeter; this is surrounded by the hadronic calorimeter, whose support structure acts as return flux for the solenoidal field. All around are eight giant coils providing for the toroidal magnetic field (from which the name for ATLAS): its goal is to bend the escaping muons, measured by the external muon chambers. Table 1.2 summaries the general goals for the ATLAS sub-detectors and their coverage.

subdetector	resolution	η coverage
tracking system	$\sigma_{p_T}/p_T = 0.05\% \oplus 1\%$	± 2.5
EM calorimeter	$\sigma_E/E = 10\%/\sqrt{E} \oplus 0.7\%$	± 3.2
Central Hadronic calorimeter	$\sigma_E/E = 50\%/\sqrt{E} \oplus 3\%$	± 3.2
Forward Hadronic calorimeter	$\sigma_E/E = 100\%/\sqrt{E} \oplus 10\%$	$3.1 < \eta < 4.9$
μ -spectrometer	$\sigma_{p_T}/p_T = 10\%$ at $p_T = 1$ TeV	± 2.7

Table 1.2: Required resolution and coverage of the main ATLAS sub-systems.

In the following a brief description of each sub-detector is given.

MAGNETIC SYSTEM: the ATLAS magnetic system is composed by a central superconducting solenoid for the inner tracker and an external toroidal field for muon momentum measurements.

The solenoid provides a central magnetic field of 2 Tesla and coils have been positioned between the tracker and the electromagnetic calorimeter, and in order to achieve the desired compactness and minimize the dead material amount the solenoid is placed in the same vacuum vessel of the electromagnetic calorimeter.

Height air-core coils disposed with radial symmetry in the external Barrel region ($|\eta| < 1$) and two End-Cap coils ($1.4 < |\eta| < 2.7$) create the toroidal magnetic field; the peak magnetic field is about 4 Tesla and it is needed by the muon spectrometer;

INNER DETECTOR: due to the high track density expected at the LHC, the ATLAS tracking system has been projected in order to be a high granularity detector; this results in a huge number of electronic channels, and thus a very dense system. Different technologies have been applied in order to minimize the dead material and to provide at the same time the reconstruction algorithm with redundant information for tracking and vertexing.

The inner detector is immersed in the 2 T magnetic field generated by the central solenoid; in the barrel region the different technologies are arranged in a cylindrical configuration around the beam axis. At inner radius, the high-density track information are furnished by silicon pixel and microstrip layers (SCT), which offer high granularity and pattern recognition capabilities. At larger radius, the transition radiation trackers (TRT) provide almost continuous tracking and improve the momentum resolution in combination with the SCT layers.

CALORIMETERS: The calorimeter system covers the region $|\eta| < 4.9$ and is composed of detectors using techniques in order to exploit the best performance while maintaining a sufficient radiation resistance in each region. The calorimeter segmentation is such that several shower samplings are provided both in the longitudinal and in the transverse direction. The main calorimeter components are:

- **electromagnetic calorimeter:** a lead-liquid Argon calorimeter with accordion geometry to minimize the read-out cables and at the same time to prevent the channeling effect; the global coverage is $|\eta| < 1.475$ in the Barrel, $1.375 < |\eta| < 3.2$ for the End-Caps. Between the Barrel and the solenoid a Pre-Sampler homogeneous electromagnetic calorimeter is housed; this helps the estimate of the energy losses in the internal volumes. It is highly segmented and longitudinally divided in three layers, which allows for electron and photon identification and measurement in combination with the inner tracker;
- **hadronic calorimeter:** the ATLAS hadronic calorimeter is composed by three parts:
 - the Barrel and the Extended-Barrel parts, which cover the pseudorapidity region $|\eta| < 1.7$; the Barrel supporting frame is used to close

the solenoidal magnetic field. It is a sampling calorimeter, with plastic scintillator tiles as active medium and steel as passive medium; signals are read out by wavelength shifting fibres, which are grouped in pseudo-projective towers which form the cells. Each cell is coupled to a photomultiplier;

- Hadronic End-Cap Calorimeters (HEC), cylindrical structures which cover the region $1.5 < |\eta| < 3.2$. They are housed in the electromagnetic End-Cap cryostats and are based on the liquid Argon technology with copper plates devices;
- **forward calorimeters:** the Liquid Argon Forward Calorimeter (FCal) extend in the region $3.1 < |\eta| < 5$ and uses copper and tungsten as absorbers; again, the choice of liquid Argon is due to the radiation hardness required for this critical region.

Altogether, the calorimetric structures offer high hermeticity and granularity. The central hadronic calorimeter, TileCal, is the most important detector for this work and will be briefly described in Chapter 3;

MUON CHAMBERS: the need for a precise and standalone measurement of muon momentum is fulfilled by the toroidal field and high-precision tracking chambers. This apparatus is at all the effects a muon spectrometer, and supply for the low-quality information from the inner tracker in the case of very energetic muons. The magnetic configuration provides a field which is orthogonal to the muon trajectories, while minimizing the resolution degradation due to multiple scattering. In the barrel region the tracks are measured by chambers disposed on three cylindrical layers, while in the end-cap sections the chambers are installed in layers perpendicular to the beam axis.

1.4.2 Trigger and data acquisition system

The ATLAS Trigger and Data Acquisition (*TDAQ*) is implemented with three levels: *LVL1*, *LVL2* and Event Filter. Each trigger level refines the previous one, using more and more information from the whole detector and have larger latencies. This allows for fast and precise reconstructions of the interesting events within the allowed time constraints.

The input frequency for the *LVL1* trigger is the bunch crossing rate of 40 MHz; the initial selection is based on raw information from various sub-detectors but using low granularity. The main criteria are high p_T muons, photons, electrons and jets, τ s decays in hadronic channels and missing transverse energy. The *LVL1* trigger latency is $2.0 \mu s$; in case an event has been marked with the *LVL1* accepted flag, the event signals stored in pipelines in the front-end electronics is passed at the *LVL2* trigger at a maximum frequency of $75 kHz$. *LVL2* refines the previous choices making use of more complete information and takes decisions in about ~ 40 ms, reducing the output rate to $3.5 kHz$. The third trigger level, the so-called *Event Filter*, uses the whole detector information to create the raw-data to be recorded for permanent storage at $\sim 100 Hz$ frequency. Approximately each ten seconds ATLAS produce $\sim 1 GB$ raw-data flow to be reconstructed and analysed offline. Such a goal

is achieved by means of a multi-tier structure, ideal for distributing, computing and data storage; such an effort is the basis for the *grid* distributed technology.

Additional prescales can be applied during latency between the three trigger levels in order to reduce selectable event rates.

The Read-Out Drivers (RODs) are detector-specific elements installed at the detector back-end. After an event is accepted by the Level 1 trigger, the data flow from front-end pipelines to the RODs for formatting and reconstruction, which must occur at the *LVL2* acceptance frequency. Part of this work is related to the algorithm executed inside the TileCal RODs and is described in the next Chapters.

Chapter 2

Basic concepts of calorimetry

A brief introduction to calorimeters is presented, in order to highlight the interesting points and the basic concepts that lead to the structure and organization of these devices.

A calorimeter is a block of matter used to absorb the particles passing in it. Its aim is to measure the particle energy, and this is achieved in a destructive way: the energy is degraded by means of subsequent interactions in the calorimeter. Such a degradation generates signals of different nature, and the collection of these information is summed up to construct the particle energy.

2.1 Calorimetry overview

A calorimeter[13; 14; 15] is a block of matter which intercepts particles. Its goal is to measure the particle energy by total or quasi-total absorption of its energy, therefore its thickness must be sufficient to completely contain the primary and the secondary particles within the detector volume.

When energy increases, the process of energy absorption involves the formation of a cascade, or *shower*, of lower energy particles. Showers are related to the multiplication processes induced by the incoming particles during their passage through matter. The initial energy is degraded by means of different interactions, electromagnetic or strong ones, which produce secondary particles with progressively less energy. The shower reaches a maximum, when the particle energies start to fall under threshold for producing other particles; at this point the multiplication stops and particles dissipate their energy mainly releasing it to the calorimeter medium.

The interactions of particles with matter are the basis of the signal generation. In calorimeters, a fraction of the deposited energy, which depends on the detector material and particle interactions, is detected in form of a signal proportional to the deposited energy. The signal can be produced by various effects, such as scintillation, Čerenkov effect or ionization.

Calorimeters can be divided in two large groups: homogeneous and sampling detectors, the difference being in the absence or in the presence of passive materials. Passive materials are block of matter in which particles interact but the interaction products are not detected, in contrast to active materials that provide also the detector signal.

Homogeneous detectors use almost exclusively active materials, and particles deposit all their energy in it. In sampling calorimeter, on the other hand, the active medium is interleaved with a high percentage of passive absorber material, thus particles interact mostly in the passive layers, and only a small fraction of energy is deposited in the active medium and is available for signal generation.

A different classification is also useful considering the kind of the particle that are to be detected. Electrons and photons, that lose their energy through the electromagnetic interactions, are measured with *electromagnetic* calorimeters. The devices dedicated to the measurement of hadrons (pions, protons, neutrons) are instead indicated as *hadronic* calorimeters. Sometimes the term *hadronic calorimeter* is used to indicate only the outer sectors of the calorimeter that absorbs the last part of the hadronic shower. It will be shown that the different nature of the interaction of particles with matter define the characteristics of electromagnetic and hadronic calorimeters.

In summary, calorimeters are very attractive devices to measure the particle energy:

- they are sensible to the released energies; this in its turn means that they are able to detect charged as well as neutral particles, and often this is the only achievable method to detect the presence of the latter;
- the energy measurement is based on the total absorption of the incident particles. This is achieved by means of different inelastic collisions which degrades their energy; the shower develops producing secondary particles with lower energy;
- the energy measurement in calorimeters may be described as a stochastic process: the average number \bar{n} of secondary particles is proportional to the energy E of the incoming particle: $\bar{n} = E/W$, where W is the average energy needed to create a secondary particle. Therefore, the uncertainty in the energy measurement carries the contribution due to the statistical fluctuations of \bar{n} : the intrinsic energy resolution $\frac{\sigma(E)}{E}$ of calorimeters improves at first sight as $1/\sqrt{E}$;
- the perfect calorimeter should contain the whole shower. As a consequence, the total calorimeter depth should match the longitudinal and the lateral shower profile in order to prevent energy leakages
- calorimeters can be segmented, both longitudinally and transversely, which allows to perform precise measurements of the shower shape;
- the energy information may be available on a relatively fast time scale, however it strongly depends on the detection mechanisms.

To a certain extent, muons are an exception. In a large range of energies, from about 150 MeV until ~ 100 GeV, muons lose their energy by means of ionization processes in the absorber medium; the energy loss amounts at a few MeV g^{-1}cm^2 in this range.

Above 100 GeV, also δ -ray and μ -bremsstrahlung effects must be taken into account, but the energy losses are greater than 10 MeV g^{-1}cm^2 only for $E_\mu > 1$ TeV.

Therefore muons easily escape detection at collider calorimeters and are the most fitting example of *mip* (minimum ionizing particles) that can be found in Nature. The signals they generate in calorimeters are normally not sufficient for their identification and measurement, hence special devices, called muon spectrometers, are needed.

A drawback in using calorimeters is that the response to electrons or photons and hadrons is different, hence corrections must be taken into account. Moreover, services, cables and electronics are non-active mediums which degrade the signal and their presence is to be considered when the energy is reconstructed: calorimeters are not completely hermetic devices, and this in its turn degrades the resolution. These *dead materials* due to services are usually placed in the furthest part of the calorimeter with respect to the interaction point in order to minimize the energy degradation.

2.2 Electromagnetic showers

Electromagnetic showers are produced by the particles that interact electromagnetically with matter, such as electrons and positrons, photons and also π^0 s, which decay in couples of prompt photons.

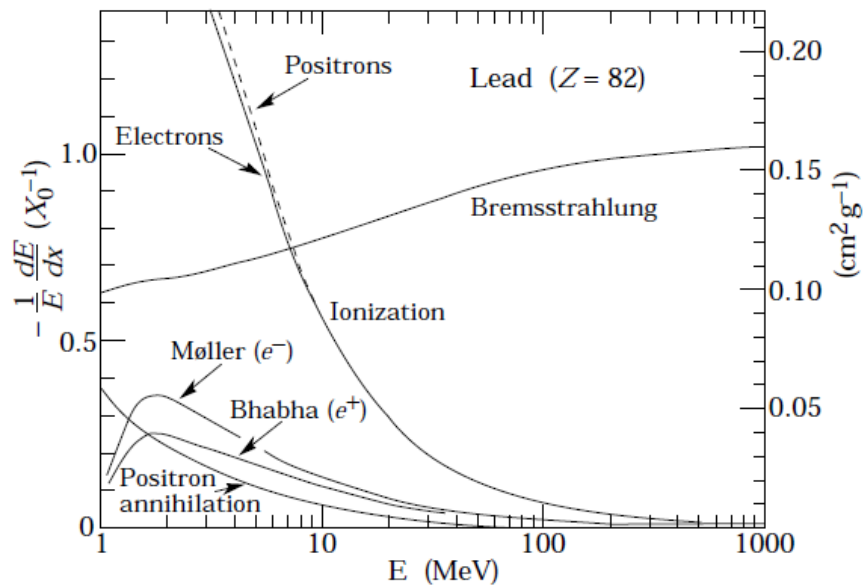


Figure 2.1: Energy loss mechanisms for positrons and electrons in lead. On the vertical axis is reported the fractional energy loss per radiation length (see later in the text) as a function of the electron or positron energy. The rate of energy loss for all the processes but bremsstrahlung falls down as the energy increases.

The contributions to the shower formation by the single processes depend on the particle type and energy; however, at high energy the picture is quite simple.

Figure 2.1 shows that for electrons and positrons of high energy ($E > 100$ MeV in lead) the energy loss is dominated by the bremsstrahlung radiation emission; Figure 2.2 instead shows that the photon cross sections for energies above $E > 10$ MeV n

lead is dominated by the pair production. The rate of these processes depends on

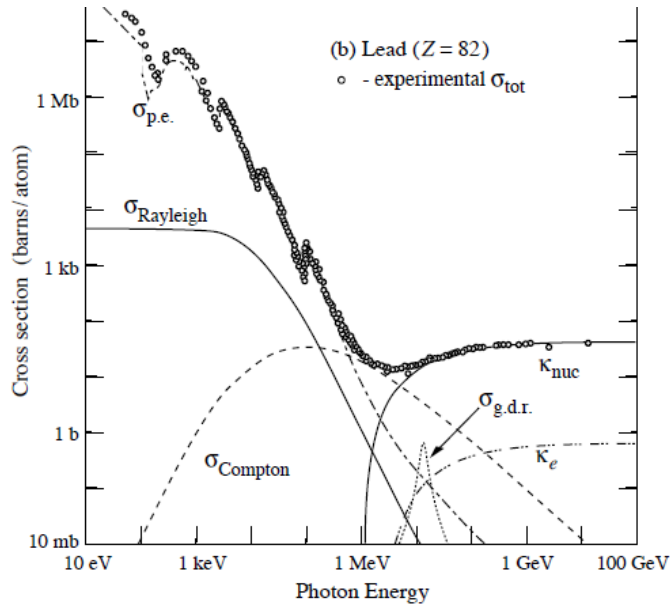


Figure 2.2: Loss mechanisms for photons in lead. The cross sections for various process are shown as a function of the photon energy. Open circles are experimental results. k_{nuc} and k_e refer to the pair production in the nuclear and electronic field respectively.

the particle energy, but at high energy they can be considered constant due to their weak dependence on E .

Another important consideration is about the absorber atomic number: the electromagnetic processes are sensible to the number and density of charge in the ab-

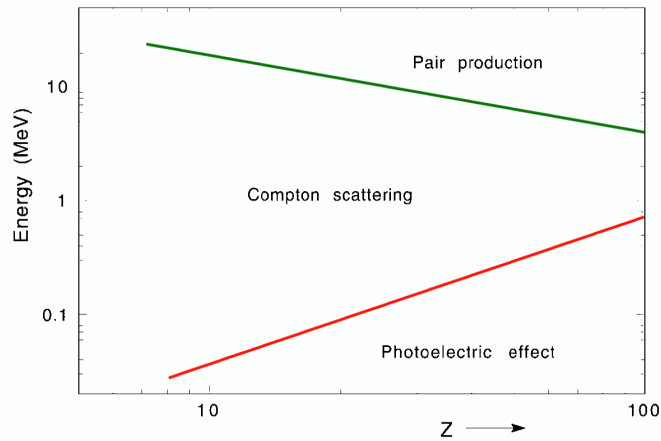


Figure 2.3: The energy domains in which the most important photon interactions for electromagnetic shower are important as a function of the absorber Z .

sorber medium, and at fixed energy different processes are dominant when Z increases. Figure 2.3 shows in this respect the energy domains for which photoelectric

effect, Compton scattering and pair production become dominant as a function of the absorber atomic number. This confirms that at higher energies and in high- Z material the dominant process is the pair production. Figure 2.4 shows that the higher the absorber Z , the most important becomes the low-energy electron and positron contributions to the signal generation, since the multiplication process continues until very low energies. This is an important factor to understand the energy resolution behavior as discussed in Section 2.4

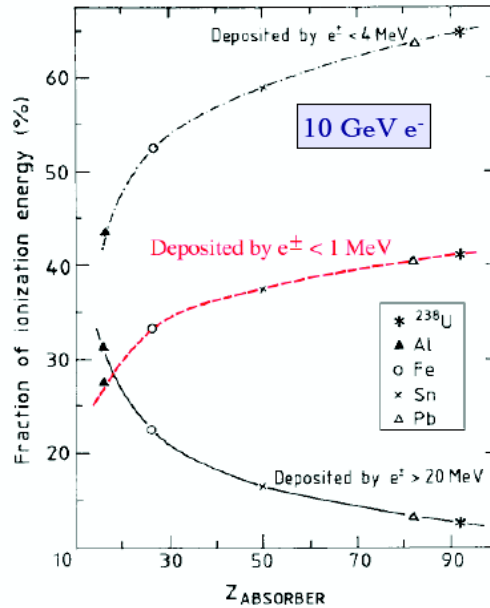


Figure 2.4: The fraction of the deposited energy in various media as a function of their atomic numbers for 10 GeV electronic showers. It is shown also the great deposited energy fraction by very low-energetic electrons and positrons ($E_{e^\pm} < 1$ MeV). Simulation results.

In order to describe the structure and the dimension of the electromagnetic calorimeters, two quantities are usefull:

- the radiation length X_0 , that is defined as the mean depth of the material over which the electron energy is reduced by a factor e by means of bremsstrahlung losses only. X_0 is usually normalized to the material density and is approximated by $X_0[\text{g} \cdot \text{cm}^{-2}] \simeq 180 \cdot \frac{A}{Z^2}$, where A is the mass number, and Z the atomic number of the transversed material. X_0 set also the scale of the interaction length for photons: at higher energies photons travel on average $\frac{9}{7} \cdot X_0$ in material before an interaction happens;
- the critical energy E_c is defined as the energy at which the electron and positron loss rate for bremsstrahlung and ionization are equal on average¹. For solids and liquids it can be roughly parametrized by $E_c = \frac{610 \text{ MeV}}{Z+1.24}$, where Z is the atomic number of the absorber.

¹A non-exactly equivalent definition for E_c is the one by Rossi: E_c is the energy at which the ionization losses per radiation length are equal to the electron energy.

As the shower develops, more and more particles are produced by radiation and pair production processes, and the average particle energies decrease. When the average energy of the shower particles reach E_c , the ionization losses become dominant. Therefore the shower reaches a maximum after which the number of particles decreases gradually. The longitudinal development can thus be described in terms of X_0 , at least for high-energy showers. This argument also shows the logarithmic energy dependence of longitudinal profiles: a photon with energy $2E$ travels $9/7X_0$ on average before converting a $E + E$ electron-positron couple: twice the energy is contained longitudinally in a little more amount of material.

For what concern the transverse shower development, it is mainly influenced by the multiple scattering of electrons and positrons and by the emission angle of bremsstrahlung radiation for photons. After the shower maximum, isotropic processes like the Compton scattering and the photoelectric effect become more important both for photons and electrons. The transverse size of the shower can be parametrized by the Molière radius $\rho_M[\text{g} \cdot \text{cm}^{-2}] = X_0 \frac{21 \text{ MeV}}{E_c[\text{MeV}]}$. 99% of the shower energy is contained within a cylinder of radius $R \simeq 3.5\rho_M$.

2.3 Hadronic showers

Hadrons passing through matter interact strongly with the nuclei. Due to the strong interaction nature, a large variety of channels are available for hadronic shower development, thus predictions are more difficult with respect to the case of electromagnetic showers.

Two main effects should be taken into account to understand the hadronic shower characteristics:

- in each hadronic collision about 1/3 of the produced pions are π^0 , that decay almost immediately in two photons, thus no further nuclear interactions happen, and this part of the shower develops electromagnetically;
- a large part of the energy lost by charged hadrons is converted in nuclear excitations or nuclei break-up; moreover neutrons interact later in the medium. Only a small fraction of this energy is detectable and a great part is definitely lost.

The first consequences are the richness and complexity of the hadronic cascades; the second one is the relation between the hadronic and electromagnetic components of the shower. In particular, the average shower hadronic fraction F_h can be parametrized as $F_h = (E/E_0)^k$, where $E_0 \sim 1 \text{ GeV}$ is a cutoff for the hadronic processes, $E > E_0$ is the initial energy, and $k \sim -0.2$ is the power which describes the suppression of the hadronic components [14]. The higher the energy, the lower is the average hadronic fraction of the shower, hence the ratio between the visible signals induced by electromagnetic and hadronic showers is $(\frac{\epsilon}{\pi})^{-1} = 1 - \left(1 - \frac{\eta_h}{\eta_e}\right) F_h$, where η_h and η_e are the efficiencies for detecting the hadronic and electromagnetic components respectively.

A calorimeter for which $\eta_e/\eta_h \neq 1$ is said to be *non-compensating*. The main effect of non compensation is that the calorimeter hadronic response is a non-linear function of the energy, due to the fact that the electromagnetic component

in hadronic shower increases with the shower energy. The hadronic shower fraction not only varies with the energy of the incident particle, but it has large fluctuations too. The hadron-induced showers fluctuate between highly electromagnetic, yielding a signal close to that of an electron-induced shower, and highly hadronic, with a maximum of invisible energy. The energy deposits at fixed energy broaden the detector response, which is no more gaussian. In conclusion, non-compensation affects both the calorimeter linearity and resolution.

The hadronic shower shape is different from the electromagnetic case due to the fluctuations in the electromagnetic fraction and to the nature of the strong interactions.

The distance that sets the scale for hadronic showers is the interaction length λ , the mean free path of energetic hadrons in the absorber material; as a rough approximation, σ_{nucl} is proportional to the effective area available for the interaction, which scales as $A^{2/3}$; therefore the typical interaction length λ is proportional to the number of scatterers and inversely proportional to the σ_{nucl} . A numerical approximation is given by $\lambda[\text{g} \cdot \text{cm}^{-2}] \simeq 35A^{1/3}$.

Hadronic calorimeters have to be designed in order to contain the whole shower, that is, they must be composed by a sufficient number of interaction lengths: for example, in the LHC environment hadronic calorimeters could have a typical thickness of about ten interaction lengths.

The shower depth also depends on the shower energy, but there are also differences related to the type of primary particles. For example protons and charged pions behave differently in hadronic calorimeters. In particular, $\lambda_{\pi^\pm} > \lambda_p$, hence it is important to consider the case in which a particle, the pion in this example, escapes detection because it exits the calorimeter without any sort of nuclear interaction, while protons are fully contained. The probability for this to happen is usually called *punch-through* and it is a source of degradation in the signal resolution.

For what concern the transverse energy deposit profiles, in the case of hadronic showers are much wider than the radial electromagnetic ones. They show a collimated electromagnetic core, due to the π^0 production, surrounded by a large hadronic halo, and develop more deeply in the medium.

2.4 Linearity and energy resolution

The main goal of calorimetry is the energy measurement of the incoming particles. The nature and the energy of the particles passing through a calorimeter is unknown a priori, and depends on the experimental conditions and the kind of interactions that take place. Therefore, in general a calorimeter should assure a good response over a large energy range. The quality of a calorimeter is mainly measured by two important quantities: the linearity and the resolution.

The calorimeter linearity is a scaling property with the energy: given that a particle of energy E generates a signal S , the calorimeter is linear if the same particle with energy kE generates a signal kS . This important propriety is therefore a function of the energy range in which the calorimeter operates and also of the considered particle. Non-linearities in calorimeters need special care.

The second important parameter is the resolution. The resolution is a measurement of the precision with which the energy of the showering particles can be

measured by the calorimeter. Hence a calorimeter could be almost perfectly linear, but with poor resolution, that is, the average energy releases are linear, but their spread is huge; or it could have a very good resolution, but non-linearities make the signal not to be proportional to the released energy over the calorimeter range of sensibility.

The resolution can be described as a squared sum of independent terms related to the different effects that degrade the measurement of energy:

$$\frac{\sigma(E)}{E} = \frac{a}{E} \oplus \frac{b}{\sqrt{E}} \oplus c$$

Each term may be dominant or negligible in particular energy ranges:

- instrumental effects: these are energy-independent, so contribute with a constant term which is the ultimate limitation on the resolution at high energies;
- the electronic noise contributes to the resolution as $\sim 1/E$;
- sampling term: the fluctuation in the number of the produced secondary particles is governed by the Poisson statistics; therefore the contribution to the resolution is proportional to the $1/\sqrt{n}$, where n is the number of produced particles in the shower. Assuming that the calorimeter is linear, the sampling term is proportional to $1/\sqrt{E}$.

A good resolution is an important goal at least for two reasons. The first one is that it allows for recognition of the signal structure; the second one is that the signal-over-background ratio can be improved with increasing resolution.

In sampling calorimeters the main contribution to the energy resolution is due to the sampling fluctuation. Since a large part of the signal is generated by low-energy electrons in high- Z material (Figure 2.4), at least for electromagnetic showers, the resolution can be in principle improved by decreasing the absorber thickness: the number of shower particles increases and then the resolution decreases.

Fluctuations in hadronic showers are greater if compared to those in electromagnetic showers. This is mainly due to the strong interactions during the early stages of the shower development: the electromagnetic fraction of energy in hadronic showers varies event to event, thus contributing to the fluctuation term.

The third term in the resolution expression is important too, and it represents the resolution limit at higher energies: for example, this term takes into account the calorimeter non-uniformities contribution.

2.5 Calorimeter segmentation and hermeticity

In order to measure the shower shape, calorimeters are segmented. The segmentation helps in particle identification and improves the linearity of hadronic calorimeters. In general, being the hadronic showers broader than electromagnetic ones, the hadronic calorimeter segmentation is wider.

In collider experiments calorimeters are often segmented in projective towers, in a way that allows for η - ϕ measurements for the signals, and the granularity is expressed in terms of $\Delta\eta \times \Delta\phi$. The tower structure defines the calorimeter lateral

segmentation. A longitudinal segmentation can be achieved by dividing each tower in segments. Such a segmentation allows to reconstruct the longitudinal shower shape. This is a very important information that can help in jet calibration.

Each segmentation volume requires a dedicated read-out electronic channel. This in its turn implies the insertion in the detector volume of cables and structures through gaps that may degrade the calorimeter hermeticity. Special care should be taken not to affect the resolution.

An hermetic calorimeter is to be preferred, especially when dealing with collider experiments and weak interactions, from which neutrinos may emerge. The more hermetic the calorimeter, the more precise is the estimate of the missing E_T , and therefore the more powerful is the ν detection.

Chapter 3

The Tile Calorimeter design

TileCal is the central section of the ATLAS hadronic calorimeter. It is a sampling calorimeter using steel as passive material and plastic scintillator as active medium. The light produced by the scintillators is collected by photomultipliers by means of wave-length shifting fibers; after photoelectrons are produced, the front-end electronics shapes and digitizes the signals, which are sent to the back-end electronics boards for amplitude, pedestal and timing reconstruction.

The fundamental role of the back-end boards is to provide the signal reconstruction within the very tight time constraint set by the acquisition rate.

The main characteristics of TileCal are the good enough resolution and linearity over a wide range of energies and its hermeticity. The resolution and linearity goals are obtained by means of a very powerful calibration and monitoring system.

3.1 Tile Calorimeter layout

The Tile Calorimeter [16] is a hadronic sampling calorimeter with steel plates as absorber material and scintillating tiles as active medium.

It consists of a cylindrical structure with an inner radius of 2280 mm and outer radius 4230 mm, for a total length of about 12 metres. It is subdivided in three cylinders: a 5640 mm long central barrel, covering the $|\eta| \lesssim 1$ region, and two extended barrels for $0.8 < |\eta| < 1.7$ coverage. The lateral cylinder are referred to as *EBA* and *EBC*; the barrel region to is considered split in two different parts called *LBA* and *LBC*; Figure 3.1 shows the module division and the η coverage.

Each cylinder consists of 64 independent modules wedge-shaped, with an angular size of $\Delta\phi = 0.1$ rad. The ~ 60 cm gaps between the cylinders provide the Inner Detector and the Liquid Argon electromagnetic calorimeter with services and electronics; the Tile Calorimeter embraces all the sub-systems but the muon spectrometer, thus its iron structure is responsible for supporting all the inner weight. The provided solution is a self-supporting structure with no connections with the muon system.

Part of the gaps between the cylinders is used for Tile Calorimeter extensions: in particular two scintillator wheels extend in the regions $1.0 < |\eta| < 1.2$ and are used in the early LHC periods as simple trigger scintillators (*Minimum Bias Scintillators*).

The tiles are perpendicular to the beam axis and are read-out by wavelength shifter fibres, which transport the light to the photomultipliers. The fibres are grouped in order to form cells with the desired granularity of $\Delta\eta \times \Delta\phi = 0.1 \times 0.1$ for the first two longitudinal samples, and $\Delta\eta \times \Delta\phi = 0.2 \times 0.1$ for the third one. The total number of interaction lengths of a tower at $\eta = 0$ is 7.2λ , for a total amount of 10λ including the material in front of TileCal. Each cell is read-out by two photomultipliers to provide redundancy; each PMT is followed by its electronics channel, for a total number of ~ 10000 channels.

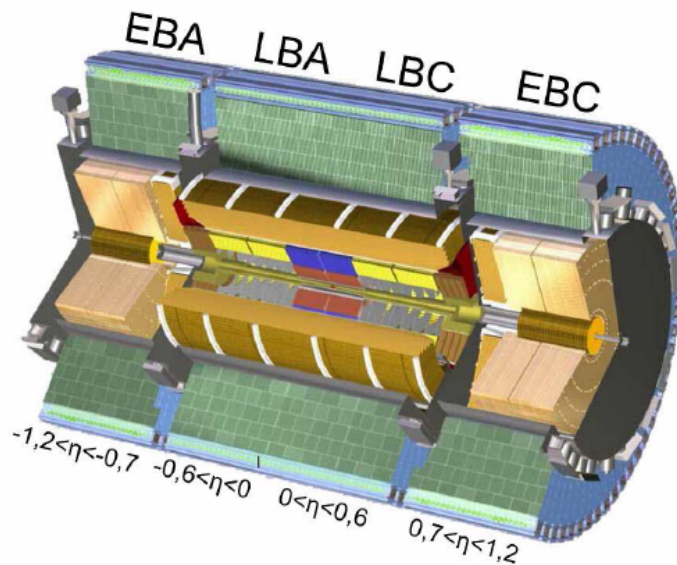


Figure 3.1: TileCal (green and blue structure) and inner detectors; the central Barrel is treated as two different Barrels.

TileCal components are described in the following Sections, in which the significant details used in this thesis are presented.

3.1.1 TileCal basic requirements

The main role of the Tile Calorimeter is to contribute to the jet reconstruction and to the measurement of the missing transverse momentum. The energy deposited in the tile calorimetric cells by the particle produced in collisions at $\sqrt{7}$ TeV ranges from a few tenth of MeV, corresponding to the signal of a minimum ionizing particle, to a few TeV. It is therefore important to have a good performance over a wide energy range. Moreover, the limitations imposed by the pile-up require a fast signal integration and a good granularity.

To achieve these goals, TileCal has been designed following (at least) five guidelines [17]:

- percentage of energy resolution of the order of $\frac{\Delta E}{E} = \frac{50\%}{\sqrt{E}} \oplus 3\%$;
- linearity within a few per cent from hundreds of MeV to few TeV;

- uniformity in η and ϕ directions;
- high hermeticity;
- radiation hardness.

A last subtle point is the TileCal intrinsic non-linearity. The Tile Calorimeter is non-compensating: the signal produced by charged pions of a given energy produce a signal that is much smaller than the corresponding one produced by an electron.

Non-compensation makes the calorimeter non-linear also for hadrons and degrades its energy resolution. The non-linearity measured during test-beams is $\sim 30\%$ in the energy range $10 \div 300$ GeV for Tilecal. The compensation is obtained with offline algorithms, by the application of weights to the signal measured in the different sampling depths. This procedure allows to restore the linearity and to improve the energy resolution of the showers generated by hadronic particles or jets.

A 5 % uncorrected non-linearity would be critical: it could for example increase the jet cross section at high p_T , and thus fake or simulate new Physics. The request for TileCal is to recover non-linearity at a level of 1-2 %, therefore it is very important the understanding of both the detector and algorithms, as well as each sort of signal degradation.

3.1.2 TileCal environment

Due to its position, TileCal has to face different problems related to the experimental environment:

DEAD MATERIAL AND DETECTOR THICKNESS: a very important contribution to TileCal performance is related to the amount of dead material particles encounter before entering the hadronic section. In particular, the Liquid Argon cryostat is 2-3 radiation length thick, thus an energy correction is needed in order to recover resolution and linearity, especially for what concern jet energy measurements. Figure 3.2 shows the material distribution for the ATLAS detector in terms of interaction lengths as a function of pseudorapidity: the mean interaction length is about $\sim 10\lambda$ for the Barrel region. This is enough to contain hadronic showers and to reduce the punch-through.

RADIATION DAMAGE: most of the particles produced in the proton-proton collisions are absorbed in the calorimeters and in particular in TileCal. Neutrons form an uniform and almost isotropic gas of low-energy background that has no time structure of the LHC bunch crossing time scale because of the large number of scattering they are involved in before they stop. The annual dose for TileCal is below 40 Gy per year.

Such a rate is responsible for damaging the optical structures of TileCal, but the energy resolution and the jet signal degradation are negligible even if running ten years at high luminosity.

MAGNETIC FIELD SHIELDING: the TileCal layout is also the return path for the flux of the solenoid and is influenced, even if to a small extent, by the toroidal field. There are two major implications: the influence on scintillator light and on photomultipliers.

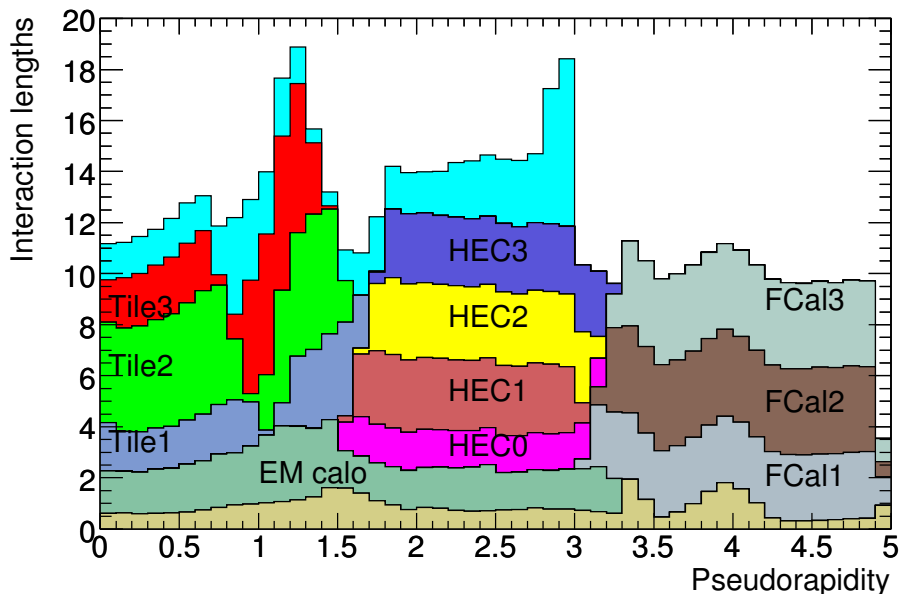


Figure 3.2: Total thickness in term of interaction lengths as a function of pseudorapidity for the ATLAS calorimetry. *Tile1*, *Tile2* and *Tile3* refers to interaction lengths of the three longitudinal TileCal sections.

As a consequence of the magnetic field, the scintillation light is increased of about $\sim 1\%$, but this value is within the cell-to-cell intercalibration accuracy and is then negligible.

The PMT blocks are shielded by means of two cylinders in which they are housed, one of soft iron and the other of a μ -metal. This shielding limits the signal degradation to the level of 1% .

3.2 TileCal mechanics and optics

TileCal is composed by a Long Barrel and two Extended Barrel cylindrical structures, each divided azimuthally in 64 modules of trapezoidal shape, and each module is further divided in submodules. In Figure 3.3 a typical TileCal module structure is shown: tiles, fibers and photocathods compose the optical read-out system.

Steel trapezoidal plates are assembled in order to create pockets in which the scintillating tiles are inserted. The ratio in volume of steel and scintillator is 4.67 : 1.

On the trapezoid axis of all the plates are located holes where, during the final TileCal assembly, calibration tubes have been inserted for the Cesium hydraulic system. The optical read-out fibres run radially from the scintillating tiles towards the larger end of the structure.

Each fibre collects the light from different tiles belonging to the same cell; the cell-scheme in Figure 3.4 is the basis for such a choice and defines the cell structure of TileCal.

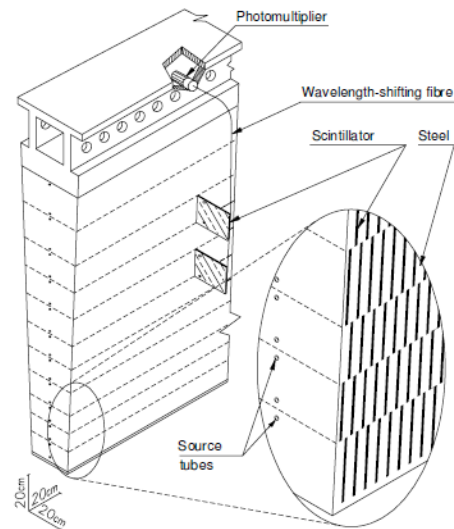


Figure 3.3: Standard TileCal module structure. The main optical components are depicted: scintillating tiles, fibers and photomultipliers; the holes are reserved for Cesium calibration, see Section 3.5.

One of the most evident TileCal features is the tile orientation: the design is such that the scintillators are placed in planes perpendicular to the beam axis, and this in its turn results in a good sampling homogeneity.

Cells are defined by the fibres collecting the light to the photomultipliers. Figure 3.4 clearly shows this arrangement: for example, looking at the Barrel module, cells of type *A* (the nearest to the interaction point) consists of three rows of spacers and

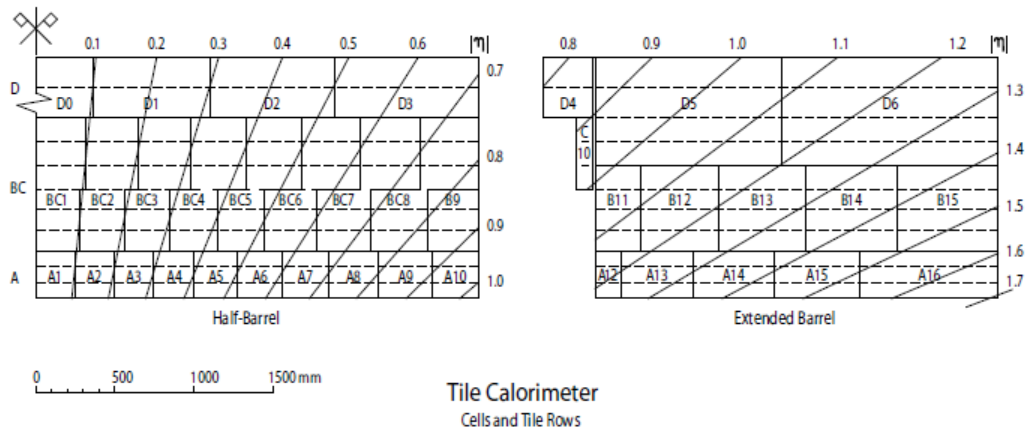


Figure 3.4: A layout of cells and tile rows: cells are named *A*, *BC* and *D* followed by an identifying number; rows are represented by the dashed lines. The half-Barrel, the Extended Barrel and the ITC (cells *C10* and *D4*) are presented. TileCal signals refer to cells and η towers, not to tiles.

tiles (the horizontal dashed lines); cells of type BC^1 consist of 6 rows, D type of 2 rows. The Figure 3.4 also shows that each cell shape is singular and different from others: the reason is that group of cells define projective calorimetric towers.

The module structure ends to the external side with the girder components. It plays a double role in supporting the module and in providing the space for photomultiplier tubes and the front-end electronics. In order to assure fast and easy access to the TileCal read-out system, a movable drawer is inserted inside the girder (Figure 3.5 shows a drawer and its components); such a drawer contains both the front-end electronics and the photomultipliers.

The girder is also responsible for a partial shielding of the drawer instrumentation from the return magnetic flux.

3.3 TileCal front-end electronics

The TileCal front-end electronics is responsible for converting the fast light signals from scintillating tiles in electronics signals and for their digitization [19]. All these processes are performed by electronics modules contained in the drawer structure (Figure 3.5). The main instrumentation parts are the photomultiplier block (PMT block), the MotherBoard and the Digitizer card.

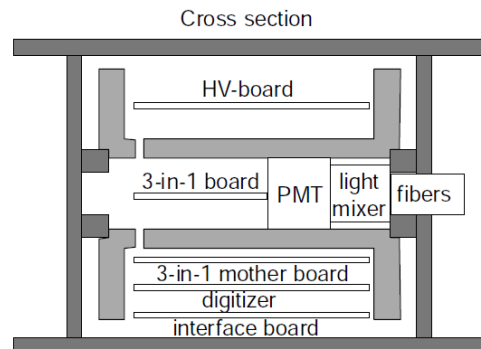


Figure 3.5: A girder and drawer cross section. The girder is the darker, surrounding structure, the drawer and its components are housed inside.

The PMT block contains two components: the photomultiplier and an electronic board called *3-in-1 card*. The photomultiplier is responsible for providing the electronic signals from the light pulses received from the fibres; the *3-in-1 card* provides the pulse shaping.

The MotherBoard is responsible for controlling the *3-in-1* (see Section 3.3.2).

The output signals are sent to the digitizer board, which perform the digital conversion, a first elaboration, quality check and send the information in specific format through optical links to the counting room.

¹ BC cells had been considered at the very beginning to be separated ones; after that, the name has been maintained, but nothing else: the optical and electronic read-out for these cells are the same as the other types.

Figure 3.6 shows the main components of the Front-End electronics and their connections: each MotherBoard controls two Digitizer modules; each Digitizer is composed by the DMU units; each DMU receives the data samples from three PMT blocks. Therefore a MotherBoard controls up to 12 channels, and each Digitizer 6 channels. These components will be described in the following.

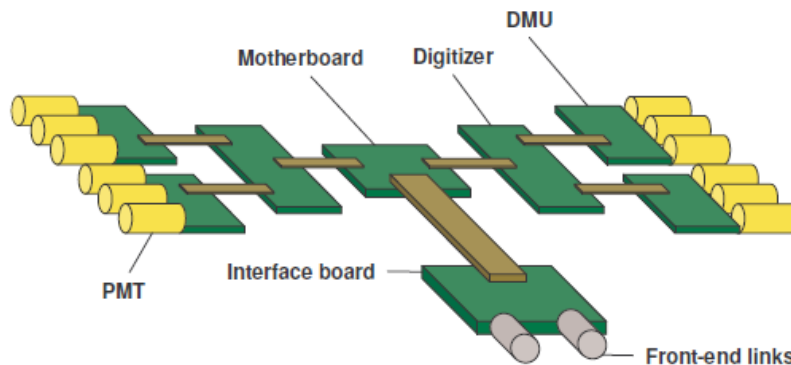


Figure 3.6: Schematic view of the hierarchical structure of the TileCal read-out chain in a module.

The hardware scheme is very important for at least three reasons. First of all, such a division is useful because it limits data corruption to the smaller elements; on the same time, noise is reduced if couplings between parts are reduced to a minimum; third, it allows to set up hardware configurations in a hierarchical way.

It will be shown in Chapter 5 that an appropriate synchronization is to be achieved for all these parts in order to work properly to ensure that the TileCal signals are correctly reconstructed.

3.3.1 PMT blocks

Each cell is read by two photomultipliers, for a total of 45 and 38 PMT blocks in half-Barrel and Extended Barrel respectively. For technical reasons the module structure is composed of 48 PMT blocks, and missing photomultiplier boxes are left empty. The PMT and its relative electronic chain are called *channel*. TileCal is equipped with almost 10000 channels.

The PMT block is installed in a dedicated hole inside the drawer (see Figure 3.5). In Figure 3.7 is shown the arrangement of the elements inside a PMT block: the light mixer is responsible for coupling the fibers with the photomultiplier, so that the output signal is independent of the fiber location; the electronic signal is then received by the 3-in-1 board which provides three basic functions: shaping and amplification, charge injection control for electronic calibration (see Section 3.5.1) and slow integration of the PMT signals for monitoring and calibration purposes.

The 3-in-1 board diagram is depicted in Figure 3.8: the PMT signal is shaped in a passive Bessel filter, closed on a divider (2 : 1 ratio); the two shaped signals have a width of about ~ 100 ns and are sent to two independent amplification chains

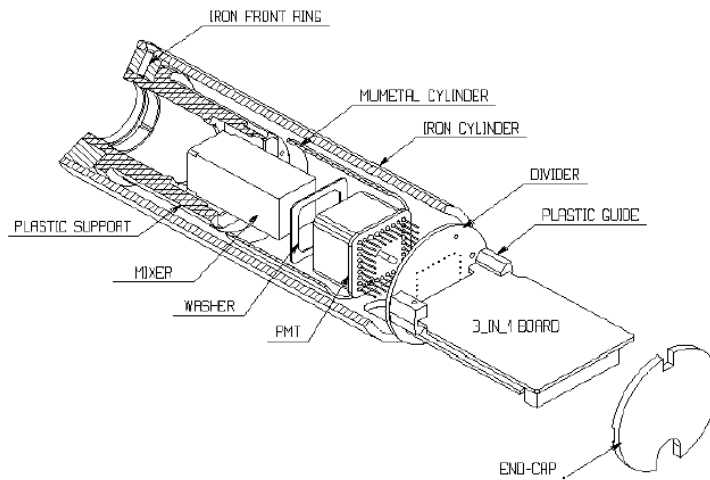


Figure 3.7: Arrangement of a PMT block: fibre bundles arrive from left and are coupled with the mixer to the PMT; the photoelectrons are then collected and the signal is shaped in the 3-in-1 card. The whole structure is shielded in a iron and a μ -metal cylinder.

and the resulting outputs have a gain ratio of 64. The two chains are referred to as

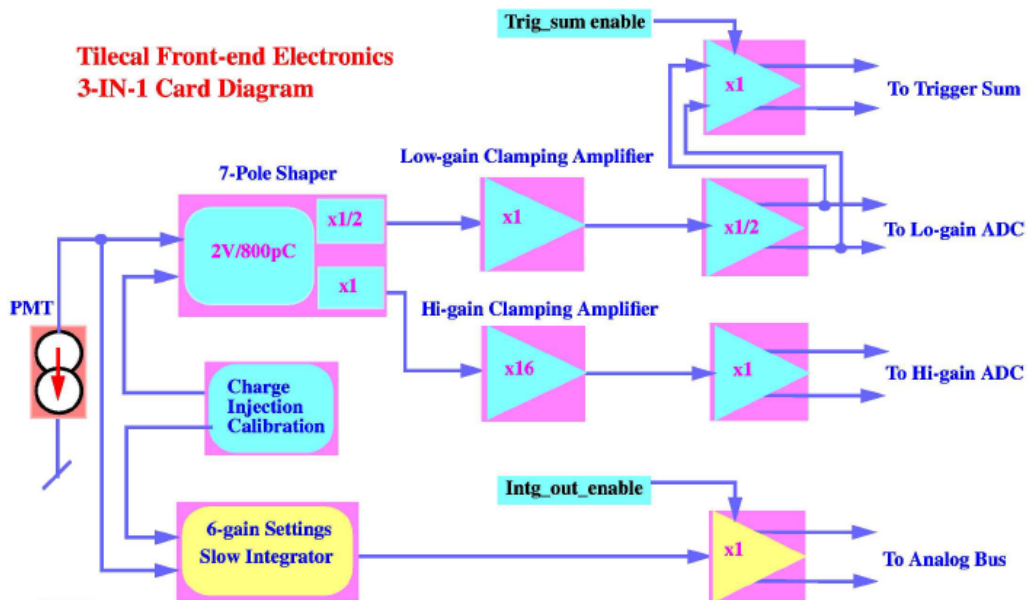


Figure 3.8: The 3-in-1 board diagram. The various parts are described in the text, just note the three functionalities of the card: in the central region the shaping and amplification chain with the signal for the *LVL1* trigger on the top; on the bottom the slow integrator for Cesium calibration; the CIS device that inject a known charge into the shaper in order to calibrate the electronics.

Low Gain and *High Gain* branches, and are sent to the Digitizer board for further elaboration; from the Low Gain branch a differential signal is also sent to the *LVL1* trigger system. The multi-gain structure allows to measure the cell signals from a few tenth of MeV up to ~ 1 TeV, maintaining a high enough resolution in the whole energy range.

The second function of the 3-in-1 board concerns the possibility to control and inject at the input stage of the shaper circuit a known signal of programmable amplitude. This device, called *Charge Injection System* (CIS) is part of the calibration of TileCal and is described in Section 3.5.1.

The last function implemented in the 3-in-1 card is the slow integrator, used by the Cesium system, a further components of the calibration system (Section 3.5).

3.3.2 Motherboards

Signals and services are transmitted along the drawers with a three-layer structure, called the Motherboard, below the PMT block structure (see Figure 3.5).

The upper layer is the *3-in-1 MotherBoard* and carries the low voltage power and the digital control signals for the PMT block. In particular, it is responsible also for the synchronization of the CIS for the controlled channels. MotherBoard timings can be set-up with a granularity of half nanosecond.

The middle layer (the *Digitizer Board*, see Section 3.3.3) is connected to the analog output signals from the 3-in-1 card in the PMT block and is responsible for digitizing the signals.

The outer layer is the *Interface Card*; this layer is important since it transmits the sampled signals to the back-end modules.

3.3.3 Digitizer card

The shaped and amplified signals generated by the two amplification chains (High Gain and Low Gain) in the 3-in-1 boards are sampled, every 25 ns, and digitized by 10-bit ADCs in dedicated CPUs, the *TileCal Data Management Unit* (TileDMU), inside the Digitizer board. Each Digitizer board contains two TileDMU units.

For each channel two ADCs are required, one for each gain branch. The default samples are the ones from the High Gain branch, unless saturation in the HG-ADC has occurred, in which case the Low Gain samples are passed.

The saturation in the High Gain branch occurs for charge above 12.5 pC, while the Low Gain region ends for input above 800 pC; being the overall electromagnetic scale calibration constant ~ 1.05 pC/GeV within 2% [22], the HG and LG regions are limited by energies of 13 GeV and 850 GeV respectively.

The samples are stored temporarily inside the TileDMUs in pipeline while waiting for the *Level 1 Accepted Signal* (*L1A*); the latency time for the pipelines is 2.0 μ s. If the event does not satisfy the *LVL1* trigger conditions, the samples are rejected, otherwise they are transferred to buffer memories. The number of consecutive samples to be pushed in the buffers is programmable up to 16, but usually in Physics and Calibration mode this number is set to 7.

In Figure 3.9 a Digitizer Board is shown with its components. The data flows from top to bottom, entering the light green part that defines the *analog part* of the board; the six black input connectors collect the signals from six PMT blocks,

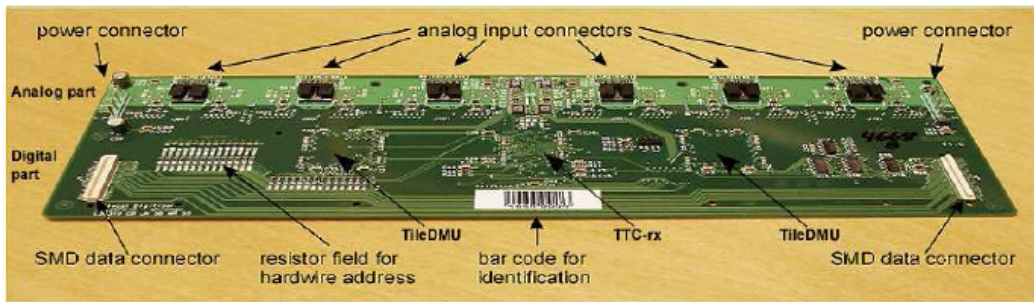


Figure 3.9: The Digitizer board. The analog part described in the text is the light green one on the top, the darker part is the digital part. Data enters from top and exits to the bottom-right part where a data connector is placed.

thus represent the channels controlled by the Digitizer. In the lower darker part, the *digital part*, two TileDMUs are housed and each of them controls three channels. The digital and analog parts are separated from the point of view of power and ground in order to reduce the noise contribution.

The third important part on the Digitizer Board is the *TTCrx* chip, which is responsible for synchronizing the Digitizers.

Each DMU allows for a double clock choice. The first one (*clock40des2*), sets the digitizing clock in steps of one LHC bunch crossing, the other (*dskew2*) set the fine tuning in step of 106 ps. Formally, the *clock40des2* is synchronous but delayed with respect to the LHC clock, while the *dskew2* is a tunable correction to the *clock40des2*. Since there is only one TTCrx per Digitizer cards, the timing settings are applied to all the 12 ADCs, that is, the synchronization is at the level of 6 channels at this stage. This is an important point, since it will be shown (Chapter 5) that synchronization is critical for energy reconstruction in TileCal. The strategies adopted to reach the TileCal synchronization are briefly described in Section 3.5.

3.4 TileCal back-end electronics

While waiting for *L1A* trigger signal, the samples are stored in pipelines in the Digitizers. If the *LVL1* Trigger System accepts the event, the samples are sent to the back-end electronics located outside the experimental area for signal reconstruction and further analysis. The structure responsible for signal reconstruction is the *Read Out Driver* board (ROD).

3.4.1 The Read Out Driver boards

The ROD motherboards are the core of signal reconstruction [24]. The four partitions *LBA*, *LBC*, *EBA* and *EBC* are read-out by four ROD-crates, and each board receives 8 input links from 8 TileCal modules, thus 32 ROD boards are required to read-out TileCal.

Each board is supplied with 4 slots for *Processing Units* (or PUs). It consists of a mezzanine card with two input connectors, hence each Processing Unit handles up

to 192 channels, that correspond to 48 channels in 4 TileCal modules.

Input data is formatted and error check is performed inside the the PU, then the information is passed to the *Digital Signal Processor* (DSP). The DSPs are microprocessors specifically designed for fast digital signal processing: the signal rate at this level is about ~ 80 MHz, and this imposes severe limitations to the bandwidth and therefore to the data format chosen for the reconstructed signals.

Output data are organized in fragments and pushed in buffers for *LVL2* processing in blocks of 32-bit words. The bit-fields for normal data-taking mode are shown in Table 3.1; in calibration mode, since the event rate is adjustable, the word

G	EEE EEEE EEEE EEEE	PPP PPPP PPPP	F	QQQQ
---	--------------------	---------------	---	------

Table 3.1: The 32-bit data word of ROD for the on-line reconstruction; the most significant bit is on the left. The first bit is the gain (G), then 15 bit are dedicated to the amplitude (E), 11 to the phase (P) and 4 to the quality reconstruction flag (Q).

structure is different and much more information can be extracted and written to disk.

During normal data-taking the pedestal for the reconstructed amplitude is calculated but not propagated.

The input data unit is ADC; the output data may be ADC, pC or MeV. The unit conversion takes into account the gain amplification factor. The conversion is performed using a look-up table in which constants are stored with limited precision. The limitations on performance due to the fixed-point arithmetic are discussed in Chapter 5.

3.5 TileCal calibration methods

The goal of the calibration is to define the energy scale, that is to define the conversion between ADC counts and GeV, in a uniform way for the whole calorimeter. The aim is to reach a good uniformity, so that the constant term in the energy resolution is kept well below 5% and non-linearities are below 2%.

The calorimeter calibration and monitoring is performed using both data produced by a three fold integrated system, described in the following, and test beam data. The integrated system uses three sources: the Cesium source, the laser source and an electronic charge injection (CIS). The CIS system will be described in details in Section 3.5.1, since it has been used for the studies presented in this thesis.

Each TileCal cell can be divided in three sections: the optical part (consisting of scintillator and fibres), the photomultipliers and the front-end electronics. Each source inject a signal at the input stage of one of these parts, allowing to inter-calibrate and monitor all the single components.

The optical system is calibrated and monitored with a Cs^{137} γ -source moved hydraulically inside the calorimeter. This enables the settings of the PMT voltage for each channel and allows for cell inter-calibration. The mean response accuracy for a calorimeter cell is $\pm 0.3\%$.

A laser system is used to control the photomultiplier and the front-end chain responses with an accuracy of better than $\pm 1\%$. The laser generates pulses of ~ 10

ns length and a wavelength of 532 nm. The laser light is split in a service cavern and sent via plastic fibres to each module photocathods; the global photomultiplier non-linearity is found to be less than 0.5% above 80 pC.

The Charge Injection System is designed to calibrate and control the front-end circuits to an accuracy of 1%. It is embedded in the 3-in-1 card and injects a known and settable charge in the electronics chain. This system is described in details in Section 3.5.1.

The overall energy scale is set up by test-beam studies [22]. About 12% of the TileCal modules have been used at test-beams with electrons, with energies between 10 GeV and 180 GeV impinging at different angles in the *A*-cells. The electron showers are almost completely contained in the first cell layer, whose electron response is linear within 1%. These data are used to obtain the calibration factor to convert the electronic signal in GeV units. The *BC*-cell and *D*-cell responses have been studied using beams of 180 GeV muons.

3.5.1 The Charge Injection System

The calibration of the read-out electronics is achieved by means of a device located on the 3-in-1 board which allows to inject a pulse of settable amplitude at the input stage of the electronics chain. The injected pulses and the PMT signals are read-out by exactly the same electronics. Each channel has its own device to calibrate the electronics, thus resulting in a double calibration per cell.

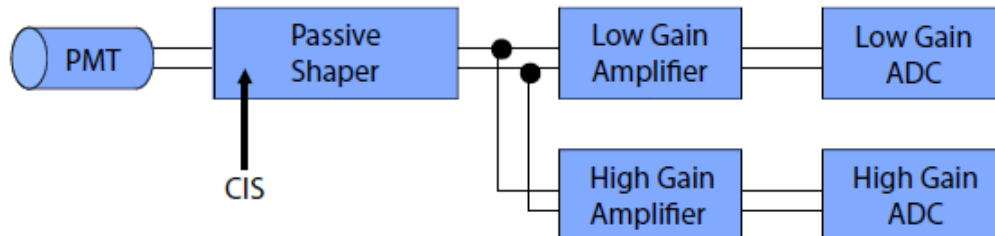


Figure 3.10: Read-out electronic chain at the 3-in-1 board level. The PMT and the CIS signal differ only in the way they are generated, but they both follow the same electronic chain.

The *Charge Injection System* or CIS [25] is the device responsible for such a calibration. A simplified sketch of the read-out chain including the CIS is depicted in Figure 3.10.

The CIS uses two calibration capacitors with capacitances 5.2 pF and 100 pF charged by a high precision voltage source, controlled by a 10-bit DAC for each channel. A FET switch enables the charge and discharge of the selected capacitor into the electronic chain simulating a fast signal from the PMT. The differences between the shaped pulses generated by the Physics signals and by the CIS injections are known and taken into account when reconstructing the signals into the DSPs.

Being the DAC word 10-bit long, the switch settable values run from 0 to 1023 and hence signals with a large spectrum of amplitudes may be used; Table 3.2 summaries

the CIS characteristics: the relation between the DAC setting and injected charge, the minimum and maximum injectable charge for each capacitor, the High Gain and Low Gain energy range covered by the CIS.

	5.2 pF	100 pF
Q_{inj} [pC]	$D \times 0.0416$	$D \times 0.801$
Q_{inj}^{MIN} [pC] ($D = 1$)	0.0416	0.801
Q_{inj}^{MAX} [pC] ($D = 1023$)	~ 40	~ 1400
HG saturation [pC]	~ 12.5	~ 12.5
HG range [DAC]	$0 \leq D \leq 300$	$0 \leq D \leq 15$
LG saturation [pC]	~ 800	~ 800
LG range [DAC]	$300 \leq D \leq 1023$	$15 \leq D \leq 998$

Table 3.2: CIS characteristics. D is the value set for the switch to control the injected charge. The two capacitors span the two gain branches with different charges and resolutions.

The maximum injectable charge is large enough to test both gains up to saturation; furthermore, each gain branch is spanned by both capacitor but in different sampling units, in particular the small capacitor cannot cover the whole LG region but offers a great resolution for low injected charge.

Another very useful feature of the CIS system is the possibility to set the timing of the charge injection with respect to the 40 MHz clock in steps of 104 ps; usually this is referred to as the *CIS phase*; it is not a calibration feature, it is a tool that CIS offers in order to be free to set different injection timings without any change in the electronics or in the Condition Database.

There is an important drawback in using the CIS to calibrate the read-out chain. Due to the residual capacitances, the FET switch injects a bipolar signal together with the requested charge into the shaper; the supplementary signal is called *leakage pulse*.

Therefore it is important to understand the leakage nature and to control it during calibration time. A proposal for this is presented in Chapter 6.

The leakage pulse has been isolated by injecting a zero charge in the shaper and scanning the phase for both the capacitors and the gains. The results are presented in Figure 3.11, and it can be seen that the two gains are affected by leakages with relative amplitude of 64.

The leakage pulse is supposed not to scale with the injected charge, hence it affects more the low charge injections than the higher ones. Moreover, the leakage pulse is always synchronous with the calibration signal.

The assumption above have been verified to a certain extent in [25]; in Chapter 6 it is shown that they are consistent with the obtained results.

The CIS allows to define a conversion factor from ADC to pC over the whole energy range. The conversion factors depend on the reconstruction method used to obtain the signal amplitude from the digital samples; the standard method is an iterative Fit algorithm, implemented offline and briefly described in Chapter 4.

In Figure 3.12 the full circles show the ratio ADC/pC as a function of the injected charge for the Low Gain branch using CIS events. Above ~ 300 pC the response is

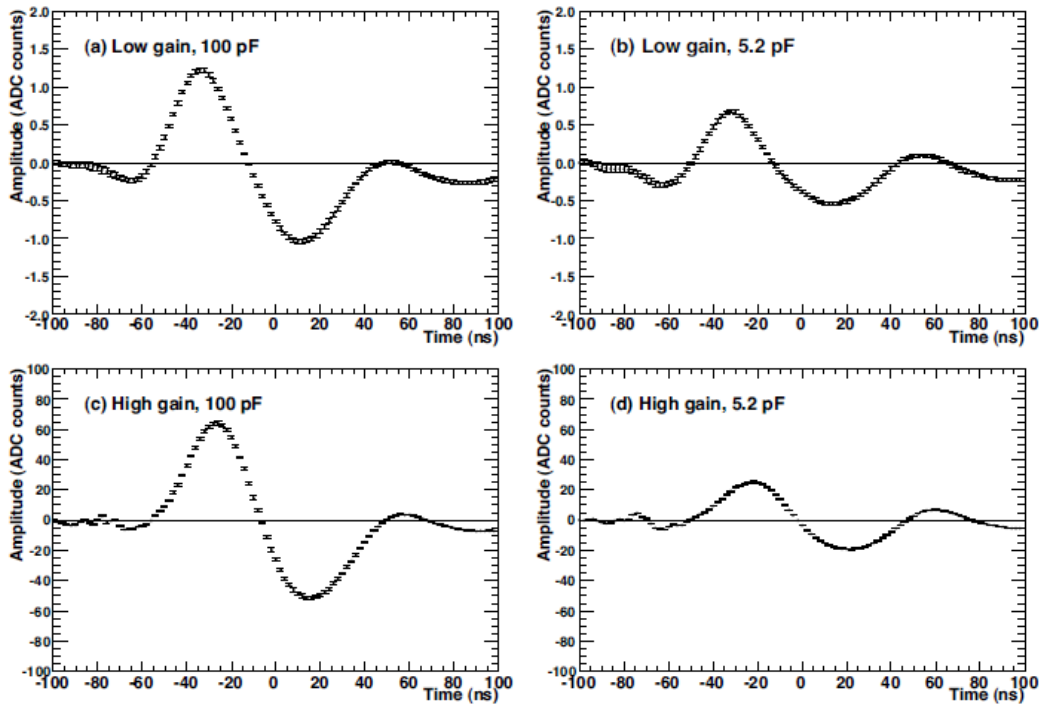


Figure 3.11: The evidently bipolar shapes of the leakage pulse for both gains and capacitors.

linear, but for lower Q_{inj} a non-linearity of about $\sim 2\%$ affects the reconstruction. In Figure 3.12 a region for which the points align within a few percent are considered², then the mean value is taken. This is called the *calibration constant* for the given channel; the average value for High Gain is 81.3 counts/pC with a 1.5% spread, for the Low Gain is 1.29 counts/pC with a 1.4% spread.

The drop in the Fit reconstruction in Figure 3.12 has been understood and it is due to the fact that when injecting charges around 40 pC the high gain branch starts to saturate. The two branches are connected by a common source, thus the operational amplifier for the high gain may shift the offset voltage for the low gain branches. This suggestion has been verified (open circles in Figure 3.12), and the corrections needed to achieve a constant linearity for the Fit method are applied in a so-called *second-order correction*.

The calibration constants are loaded inside the DSPs for the on-line reconstruction for each channel; if a reconstruction in pC units is requested for the on-line results, they are applied soon after the standard ADC amplitude has been computed³. Another choice are MeV units, for which the relation $1\text{pC} \simeq 1\text{ GeV}$ holds. The second-order calibration is later applied offline.

The achieved linearity with the whole procedure is of order of few per mille [25]

²Namely, the region above 300 pC is considered to exclude any significant contribution to the non-linearity

³A second kind of application is possible, called *off-line pico Coulomb*. In this case the second-order corrections are not applied.

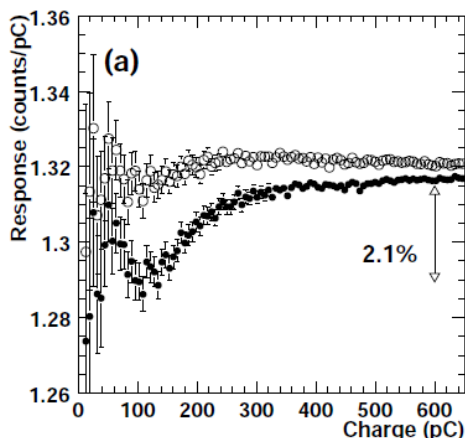


Figure 3.12: Response non-linearity: full circles are the measured low gain response when the High Gain branch is connected; open circles represent the same response when the branch is not connected.

for the Fit method.

It is worthwhile to note that the change in units causes a small precision loss when it is applied online. As stated in Section 3.4.1, the number of bit per word when propagating the information after DSP reconstruction limits the precision to the least-significant-bit value. Amplitude are multiplied by the calibration factors and the error propagates to the second level trigger. This effect is described in detail in Chapter 4 and quantified in Chapter 5.

3.6 TileCal synchronization

In order to correctly process and analyse the Physics interactions occurring at the LHC, synchronization [23] is a fundamental requirement.

A distinction has to be done among events generated in the same bunch crossing and the events from other bunch crossings [18]. A bunch crossing corresponds to the overlap of two bunches in the LHC and it is well defined by the LHC clock signal and an identifying number, the BCID (*Bunch Crossing Identifier*). The BCID is propagated to all the experiments on the LHC ring by means of optical links.

The TTC (*Timing, Trigger and Control*) system takes care of the synchronization between the trigger and the front-end electronics: TTC receives the *LVL1* accept signals, the LHC clock and other setting options.

For what concern TileCal, all the calorimeter deposits and track information must be synchronized. Each channel is characterized by its electronics, delays and noise and the different fibers length, therefore a time synchronization must be performed for each channel. A monitor to check the time setting stability will be presented in Chapter 6. The TileCal timing synchronization is obtained by acting both in hardware and software comparts.

A first cell synchronization is made with the so called *splash events* from first LHC beam data [26]. Special collimators along the beam pipe in the neighbourhood of

the ATLAS detector are closed when the beams are circulating. This causes millions of high energy particles to reach the ATLAS detectors simultaneously. The signals are reconstructed in Tilecal, corrected for the Interaction Point coordinate and the particle time-of-flights, then the reconstructed time is compared for each cell with its z -coordinate. This allows for a global re-setting of the time origin for each Digitizer.

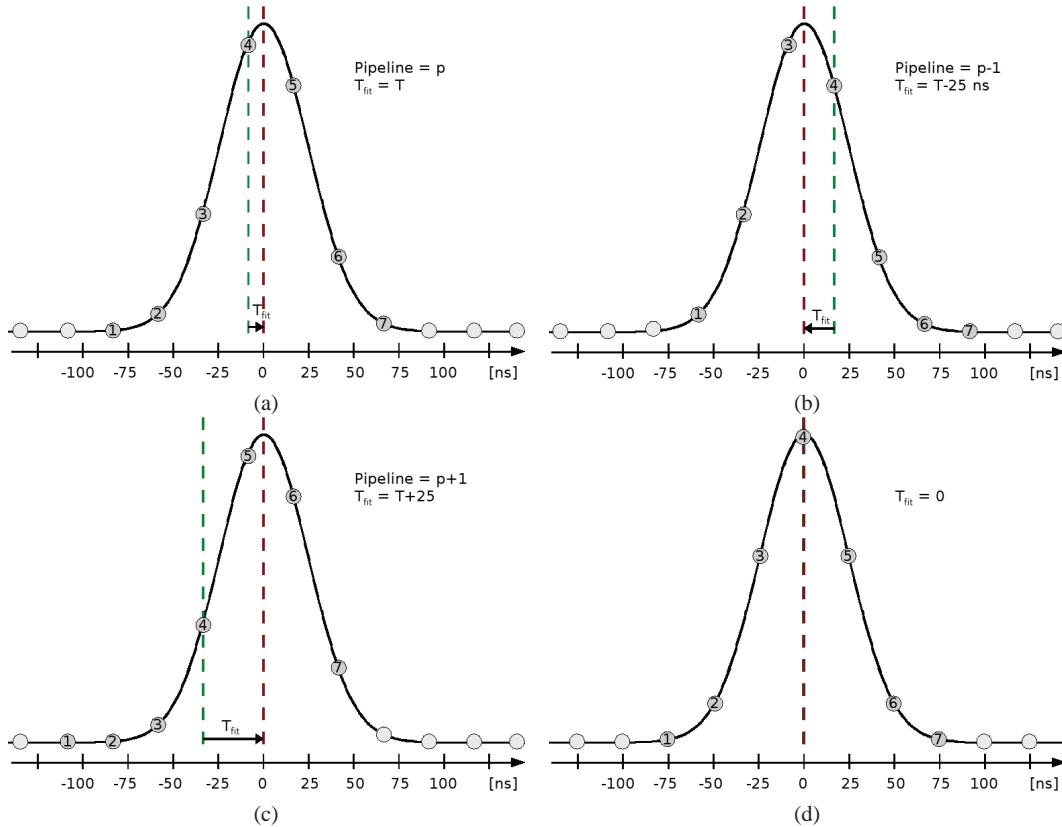


Figure 3.13: The procedure for TileCal signal synchronization in the Digitizers. The sample number 4 is the sample that sets the time origin, the T_{fit} refers to the time calculated using the Fit method briefly described in Chapter 4. In (a) the pulse peak is delayed with respect to the sampling time, therefore the sampling can be shifted, acting on the *clock40des2* clock, by +25 ns as in (b), or by -25 ns, as in (c). In case the time delay is small, it can be adjusted using the *dskew2* clock, (d). This allows for the synchronization on average of the channels in the Digitizer.

It has been demonstrated [23] that the best time and energy estimates are obtained if the signal is sampled within 2 ns from the top of the analog pulse. This means that with 7 samples, the fourth should be within 2 ns from the peak. The TileDMUs are used to synchronize the samplings and the signals, acting on groups of 6 PMTs. Figure 3.13 shows the effect of changing the two TileDMU clocks for the average signal of the group of channels. The time origin is the time of the fourth sample and it is set by the *clock40des2*, while the fine tuning is obtained with the

dskew2 clock.

The result of this setting is that on average the pulses in channels belonging to the same Digitizer are sampled at the right time. The residual delays are calculated offline channel-by-channel using the Fit method described in Chapter 4, and the results stored in the a *Conditions Database*, (the COOL database) and loaded inside the DSPs for each channel and both gains; these numbers are called T_{COOLS} , and are used by the online reconstruction algorithm (Chapter 4).

For what concern the CIS signals, they need an alternative reference clock, since no bunch is circulating during the calibration time. The time needed by the CIS is the injection time, and it is supplied by the Fit method for each MotherBoard, which controls two Digitizers boards and establishes the instant of charge injection in steps of 0.5 ns.

These are the three most important timing settings for this work; they are of different nature and apply at different levels in the hierarchical scheme of Figure 3.6).

3.7 TileCal signal generation

A brief path of TileCal signal generation is presented here, in order to highlight the differences and similarities between the Physics and the CIS signals.

3.7.1 Physics signal

The Physics signal is formed at the scintillator level by means of disexcitations of the scintillating atoms. Different scintillating tiles contribute to the light for a single photomultiplier and the number of photons is proportional to the released energy. The photons are converted in electrical signal at the level of the photocathode.

The required resolution forces the number of photoelectrons produced to be at least 1 photoelectron yield of 0.5 photoelectron/mip at normal incidence per tile. This is the same to require about 40 pe/GeV.

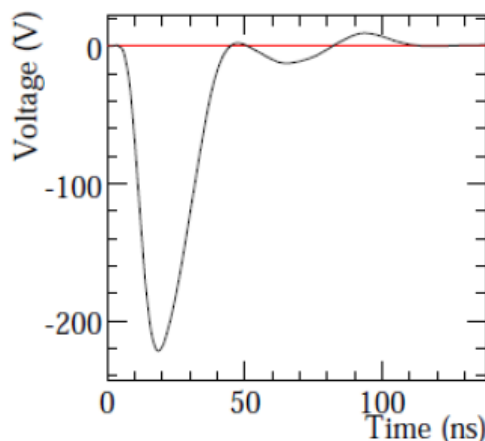


Figure 3.14: A sample pulse from a TileCal photomultiplier. Note the very fast structure of the signal.

Figure 3.14 shows a typical PMT output signal: the signal is almost completely contained within 2 bunch crossing and the surface is proportional to the number of photoelectrons, that is, to the released energy.

After shaping the signal is similar to the one depicted in Figure 3.15: the pulse shape is constant and well-known both for High Gain and low Gain branches; the signal integral over time carries the amplitude information plus the pedestal contribution; the signal duration is several bunch crossing long and its shape is simil-gaussian with a longer tail and the rising edge much steeper than the falling one.

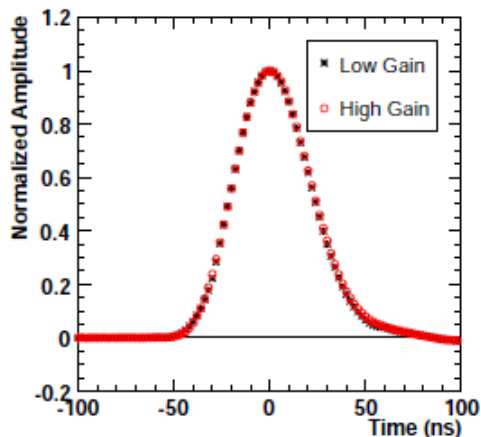


Figure 3.15: The reference CIS pulse shapes for 100 pF capacitor, corresponding to $Q_{inj} = 410$ pC for Low Gain (black points) and to $Q_{inj} = 8$ pC for High Gain (red points). The leakage pulse have been subtracted to the CIS pulse presented. The Physics signal is slightly slower than the CIS, and the differences are taken into account during reconstruction.

For the *LVL1* trigger only the Low Gain information is used, and analog summation of different cells in η towers is performed; in the meanwhile the signal is sampled and the samples are stored in pipelines waiting for the *L1A* signal and eventually sent to the RODs for reconstruction.

3.7.2 CIS signal

The selected capacitor in the 3-in-1 board is charged and then discharged at the input stage of the shaper electronics; the whole analog and electronic range can be swept, and signal timing can be set-up in order to study reconstruction performances or to understand the signal behavior. It is worthwhile to note that it is not exactly true that the CIS signal shape is constant, even subtracting the leakage pulse. It will be shown in Figure 6.1 that a slight signal variation occurs when injecting different charges at fixed phase in the same channel. The effect given on calibration will be evaluated.

After injection, the CIS signal follows exactly the same path as the Physics one. The shaped pulse result a bit sharper than the Physics one, but this differences are known [28] and correctly taken into account inside the reconstruction methods.

3.8 Noise and time structure of TileCal signals

TileCal signal generates from light emitted by the scintillating material, hence the intrinsic response of the active material is very fast. Therefore the TileCal signal generation is very fast and based on light collection and the pulse shape is always negative. A typical photocathode output is shown in Figure 3.14, and the signal peak is always contained within 50 ns since its fall-time. This is a remarkable fast signal if compared, for example, to signals based on charge collection.

In Figure 3.15 is depicted a typical CIS output signal after shaping: the signal is positive and sweeps about 5 bunch crossing, with peak around 50 ns after signal rise. The shaper is such that it keeps the time structure of signal coming from the photomultiplier, thus it only rise in amplitude with increasing photoelectron numbers and does not expand in time. This assures that the pulse shape is constant apart its pedestal, amplitude and a timing translation: these are the only free parameters needed to properly reconstruct the signal. Hence, TileCal signal reconstruction is based on some algorithm for which the pulse shape is well-known. After shaping, the signal is sampled and then eventually sent to the ROD.

More complications appear when considering the signal distortion and the noise level. Even assuming that cables and fibers are completely perfect, many other noise source appear and some of them are strictly related to the LHC environment and the experimental conditions.

The first source of noise is the possible crosstalk between the analog signals in TileCal, mostly at the very beginning of the signal chain. Signal crosstalk may fool seriously the trigger system. A level of about less than 1% is considered acceptable when using the BCID and timing information for the trigger system.

Saturation is a possible source of information loss: the pulse shape is fixed, so nothing can be inferred when three or more ADC counts are saturated. This is a very rare situation, since the huge QCD background is not expected to cause such events. In some cases a signal recovery is possible (see [29]).

Also the boards voltage has to be controlled, and links are tested in order to reduce electromagnetic interference and current loops. In this respect the coupling with optical fibres has helped to reduce this noise source.

The last two noise sources are the main ones and the noise they generate is incoherent: the thermal noise of amplifiers and cables and the pile-up. Thermal noise is reduced as much as possible by careful design and installation.

The pile-up noise increases with luminosity and with the number of samples, reducing the BCID cut efficiency. Also, a very high noise level force the use of strongest cuts in trigger since the calorimetric towers are seriously affected.

In Chapter 4 the Optimal Filtering method is introduced as the prince method that meets TileCal and *LVL1* trigger requirements and can deal with large amount of noise in signals.

Chapter 4

The Optimal Filtering method

The adopted method for signal reconstruction for both the LAr electromagnetic and the TileCal hadronic calorimeters is the implementation at the DSP level of a fast and precise algorithm, called the Optimal Filtering method. The most noticeable advantage of Optimal Filtering with respect to a traditional Fit method is the reduced numerical effort needed for the parameter extraction, that makes it suitable to be implemented in fast Digital Signal Processors.

In this Chapter the Optimal Filtering method and its implementation in TileCal are briefly presented; the importance of the synchronization as described in Section 3.6 is also highlighted.

4.1 The Optimal Filtering signal reconstruction

The Optimal Filtering method [30] - *OF* in the following- was developed as a software signal processing method for liquid ionization calorimeters operating in noisy conditions. As briefly depicted in Figure 3.14, the analog TileCal signal is very fast due to its nature and do not rely on charge collection, however the very high rate acquisition forces the choice of a very fast and, at the same time, robust signal reconstruction algorithm. Moreover, the noise produced by pile-up events also makes the *OF* a very suitable algorithm. The Optimal Filtering method provides the signal parameters as linear combinations of data samples with opportune weights. It is also stable, since it mimics the traditional Fit method, if some conditions discussed below are met.

4.1.1 Physical requirements of Optimal Filtering

The OF method is based on a few quite general assumptions about the signal shape and on at least two reasonable requests on the calculated parameters.

The first assumption is that the signal shape is known function of the parameters. A reasonable and quite general expression for the waveform is:

$$S(t) = A \cdot g(t - \tau) + p + n(t)$$

where $S(t)$ is the value of pulse at time t , A is its amplitude, τ is a temporal translation, $g(t)$ is the theoretical pulse shape at time t , p is a constant pedestal and $n(t)$ is a noise term measured at time t .

The $g(t)$ theoretical pulse shape is normalized and known for each value of t , while A , τ and p are unknown parameters.

The detector response without real input signal, that is, the pedestal distribution, is expected to be distributed as a gaussian variable, and its average and RMS are in general different from channel to channel. By collecting a large number of events with no real signal, the pedestal distribution can be built and the two parameters extracted for each channel. The mean value is the expected mean response with no real signal and in the following it is called pedestal, while the RMS is the expected spread around the mean, and it is interpreted as the noise RMS. Figure 4.1 schematically depict this

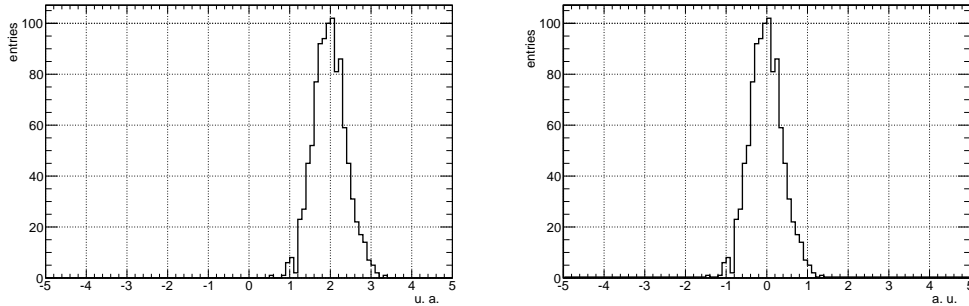


Figure 4.1: An hypothetical detector response to no real signal events: on the left the gaussian distribution of the entries, with mean value $\mu = 2$ and $\sigma = 0.4$. On the right the same distribution after pedestal subtraction. The resulting entries are gaussian distributed around zero with $\sigma = 0.4$

process: the mean is subtracted from the distribution, and it is taken as the pedestal value for the considered channel; the σ is instead used as an information of the spread due to noise around the pedestal for that channel. Since in calorimeters based on light collection the main source of noise are the electronics and thermal noises, the spread is taken the same for all the channels. Therefore, in the following the pedestal p is defined as an unknown constant, while the noise term $n(t)$ is interpreted as a stochastic contribution with zero mean value.

The waveform will be sampled k times, thus a set of digits will be available for the reconstruction: S_0 at time t_0 , S_1 at time t_1 and so on. The problem is to obtain the A , τ and p as a function of the available S_j .

Thus the sampled waveform is identified by the set of

$$S_j(t_j) = A \cdot g_j(t_j - \tau) + p + n_j(t_j) \quad \text{assuming : } \langle n_j(t_j) \rangle = 0$$

since the pedestal is constant.

If the samples S_j are used as input of a standard Fit method, the unknown parameters are retrieved by finding the minimum of the sum of the deviations weighted with the weight matrix, with elements $v_{i,j}$, as a function of the unknown parameters. The last step is the system inversion.

In the Optimal Filtering method the reconstructed quantities are expected to be on average the best estimators of the true unknown values, that is the same request for the minimum- χ^2 algorithm. It is demonstrated that the minimum- χ^2 estimates

of the parameters have minimum variances; hence the OF method too asks for such a plausible hypothesis.

The real innovation with respect to the standard Fit method is that the parameters are estimated by linear combinations of the samples, while the Fit operates in an iterative way, assuming the previous step results as a prior for the next one.

Thus no additive hypothesis is needed and the weights can be retrieved, if assuming that the τ dependence can be linearized:

$$g_j(t_j - \tau) \simeq g_j(t_j) - \tau \frac{dg(t)}{dt} \Big|_{t=t_j}$$

This in its turn means that the peak sampling time and the τ parameter are *not too distant*, that is, the shift introduced in the waveform is not too large if compared to the expected value. This is a very important hypothesis, because it allows for linearization of parameters, and also because it forces the peak sampling time to be in the neighborhood of τ (Section 3.6).

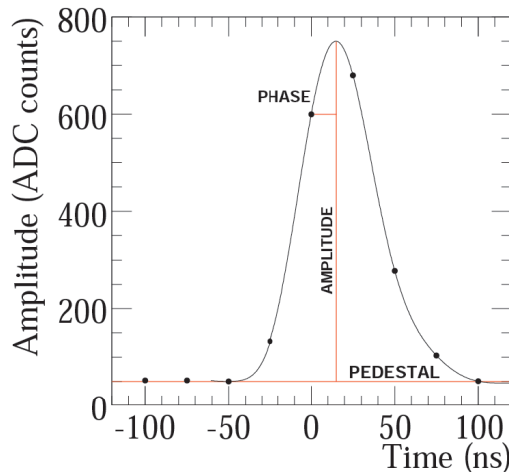


Figure 4.2: Definition of amplitude, pedestal and phase for a typical TileCal signal [31]. The points correspond to the data samples acquired every 25 ns.

Figure 4.2 shows the A , τ and p parameters defined above for a TileCal signal.¹ The τ parameter is described in the Figure as *phase*, and if it is small, in this case a few nanoseconds, the Taylor expansion is applicable.

These are the few and reasonable assumptions, based on quite general criteria. The calculation is then straightforward:

- the waveform is Taylor-expanded and sampled;

¹Figure 4.2 is a bit simplified with respect to the convention adopted in TileCal. In the following (Section 4.2) it will be shown that the τ parameter described is different from the one extracted by the *OF* implementation in TileCal. The TileCal parameter is called *phase*, and only in the very special occasion in which the signal is sampled exactly when expected, then the phase in Figure 4.2 and the TileCal phase are equal.

- for each unknown parameter a linear combination of samples is built with unknown weights;
- the mean values of these combinations are imposed to be the true value of parameters;
- the variance of each linear combination is minimized.

4.1.2 Optimal Filtering weight calculations

A very bare and simple calculation of the OF weights follows; the main idea is the process described in the previous Section. In order to simplify the notation the time dependence will be dropped and it is to be considered always when a sub-script appears: thus S_j will be used in place of $S_j(t_j)$.

Given the sampled and Taylor-expanded waveform $S_i = Ag_i - A\tau g'_i + p + n_i$, which contains three unknown parameters (A , $A\tau$ and p), three linear combinations a , b and c are created and their mean values are imposed to be equal to the three parameters, with $\langle n_i \rangle = 0 \forall i$:

$$\begin{cases} a = \sum_i w_i \cdot S_i \\ b = \sum_i y_i \cdot S_i \\ c = \sum_i t_i \cdot S_i \end{cases}$$

$$\begin{cases} \langle a \rangle = \sum_i w_i \cdot \langle S_i \rangle \doteq A \\ \langle b \rangle = \sum_i y_i \cdot \langle S_i \rangle \doteq A\tau \\ \langle c \rangle = \sum_i z_i \cdot \langle S_i \rangle \doteq p \\ \langle n_i \rangle = 0 \forall i \end{cases}$$

Furthermore, the variances should be the minimum possible:

$$\left. \begin{aligned} \text{Var}(a) &= \langle a^2 \rangle - A^2 \\ \text{Var}(b) &= \langle b^2 \rangle - (A\tau)^2 \\ \text{Var}(c) &= \langle c^2 \rangle - p^2 \end{aligned} \right\} \text{ are minimum if } w_i, y_i \text{ and } z_i \text{ are properly chosen.}$$

Let's concentrate only on the amplitude parameter A and try to solve for the weights w_i . The request that $\langle a \rangle = A$ implies that some constraints are to be put on the linear combinations:

$$\langle a \rangle = A \cdot \left\langle \sum_i w_i g_i \right\rangle - A\tau \cdot \left\langle \sum_i w_i g'_i \right\rangle + p \cdot \left\langle \sum_i w_i \right\rangle + \left\langle \sum_i w_i n_i \right\rangle$$

The mean values are to be intended on the measured samples, thus the sum sign and the w_i weights are constant; since the waveform is known, also the g_i and the derivatives can be thrown out of the mean-sign:

$$\langle a \rangle = A \cdot \sum_i w_i g_i - A\tau \cdot \sum_i w_i g'_i + p \cdot \sum_i w_i + \sum_i w_i \langle n_i \rangle$$

The last term is zero; imposing now that $\langle a \rangle = A$, it turns out that some conditions must hold:

$$\begin{cases} \sum_i w_i g_i = 1 \\ \sum_i w_i g'_i = 0 \\ \sum_i w_i = 0 \end{cases}$$

These conditions also fix the variance term to be

$$Var(a) = \sum_{i,j} w_i w_j \langle n_i n_j \rangle \doteq \sum_{i,j} w_i w_j R_{ij}$$

The noise autocorrelation term is the correlation between noise in sample i and noise in sample j , that is the same to say the correlation of noise measured at time t_i and t_j . It is important to note that the $r_{ij} \doteq \frac{R_{ij}}{\sqrt{\langle n_i^2 \rangle \langle n_j^2 \rangle}}$ are the matrix elements of r , whose inverse matrix, $v_{ij} = (r^{-1})_{ij}$, is the usual weight matrix involved in the minimum- χ^2 calculations. For the moment, the $\langle n_i^2 \rangle$ and the $\langle n_j^2 \rangle$ are assumed to be the same because the samples are extracted from the same noise distribution by hypothesis.

The minimum variance request is equivalent to ask for its first derivative to be null; it should be stressed that the derivative is calculated with respect to the weights, since the minimum has to be found with the appropriate weight choices; also, the result has to satisfy the other constraints. Therefore the minimum variance can be easily requested by means of Lagrange multipliers, one for each of the above conditions²:

$$I_a \doteq \sum_{i,j} w_i w_j R_{i,j} - \lambda \left(\sum_i w_i g_i - 1 \right) - \mu \left(\sum_i w_i g'_i \right) - \epsilon \left(\sum_i w_i \right)$$

The solving equations for the weights are:

$$\begin{cases} \sum_i w_i g_i = 1 \\ \sum_i w_i g'_i = 0 \\ \sum_i w_i = 0 \\ \frac{dI_a(w_i)}{dw_i} = 0 \end{cases}$$

Supposing that the number of samples is N and the number of parameters is k , then there are N weights and k constraints, resulting in a $(N+k) \times (N+k)$ linear system for the weights and the Lagrange multipliers.

The last equation can be then rewritten as $\sum_i w_i R_{i,j} = \lambda \sum_i g_i + \mu \sum_i g'_i + \epsilon \sum_i e_i$, where $e_i = 1 \forall i$, or in matricial notation as:

$$R\vec{w} = \lambda \vec{g} + \mu \vec{g}' + \epsilon \vec{e}$$

where w_i , g_i , g'_i and e_i have been organized in vectors. The R matrix is a symmetrical matrix and is invertible; the inverse matrix is V , and apart a scaling factor it is the same as the v matrix already mentioned.

The system becomes:

$$\begin{cases} \vec{w} \cdot \vec{g} = 1 \\ \vec{w} \cdot \vec{g}' = 0 \\ \vec{w} \cdot \vec{e} = 0 \\ \vec{w} = \lambda V \vec{g} + \mu V \vec{g}' + \epsilon \vec{e} \end{cases}$$

²It would be also possible to write the same equations making use of the $r_{i,j}$ instead of the $R_{i,j}$, but the denominator term is supposed to be a constant, as discussed before, and then can be absorbed in the Lagrange multipliers.

By substitution of the last set of equations in the three constraint relations it is possible to find the Lagrange multipliers by inverting the sub-system:

$$\begin{pmatrix} (\vec{g}^T V \vec{g}) & (\vec{g}^T V \vec{g}') & (\vec{g}^T V \vec{e}) \\ (\vec{g}'^T V \vec{g}) & (\vec{g}'^T V \vec{g}') & (\vec{g}'^T V \vec{e}) \\ (\vec{e}^T V \vec{g}) & (\vec{e}^T V \vec{g}') & (\vec{e}^T V \vec{e}) \end{pmatrix} \begin{pmatrix} \lambda \\ \mu \\ \epsilon \end{pmatrix} = \begin{pmatrix} 1 \\ 0 \\ 0 \end{pmatrix} \quad (4.1)$$

where \vec{g}^T means the transposed vector. Finally the weights \vec{w} are found by the N equations:

$$\vec{w} = \lambda V \vec{g} + \mu V \vec{g}' + \epsilon \vec{e} \quad (4.2)$$

Similar calculations have to be performed to find the $A\tau$ and p parameters.

In view of dealing with the pile-up contribution, one hypothesis should be relaxed to obtain a more general treatment: the $\langle n_i^2 \rangle$ could be different at different time³.

Thus calculations should be updated, but anyway they follow the same ideas as before. In the following, only the thermal and electronic noise are treated, thus it can be assumed that the simplifying hypothesis $\langle n_i^2 \rangle = \langle n_j^2 \rangle$ holds.

There is a subtle point here and it has been hidden in the adopted notation: the R (and therefore the V) matrix is obtained by measuring the noise contributions in different samples, thus it is a function of the sampling time. The g_i and g'_i too are functions of time, and also the Lagrange multipliers. As a consequence, the weights w_i , y_i and z_i are functions of time even in the simplified hypothesis that the mean quadratic noise term is constant.

This is a very important point, because it is true that the *OF* method only requires a linear combination of samples to reconstruct the desired parameters, but it is also true that the needed weights are functions of time, thus the method needs an information for what concern the time at which the weights are to be calculated. This is to be stressed: the *OF* method requires a prior for the τ parameter that it has to find; furthermore, the prior has to be quite precise, otherwise the Taylor expansion does not hold anymore. The iterations in the minimum- χ^2 are replaced by a prior information needed by the *OF*. It seems at this point that the method is completely useless; in the following this conclusion will be relaxed.

It is also true anyway that, given the timing information, the weights are calculated only once and then applied when needed, on condition that the prior on time does not change. In this special case the computational cost for the reconstruction is ridiculous: as an estimate, let's assume that only 3 parameters are needed, and that the number of sample is 7. There are therefore 7×3 weights to be memorized, and the computational cost is linear with the number of samples; thus only 7 multiplicative and 6 additive operations are needed for a single parameter reconstruction; this number is multiplied by 3 and a supplementary multiplication is needed in order to find τ . The total number of operations is ~ 50 for each set of samples, and considering a comparable number of registry shifts the clock cycle order of magnitude is about 100 cycles. A non-dedicated commercial CPU can perform the complete reconstruction at a ~ 10 MHz rate, which fits well to the *LVL2* incoming bandwidth.

³The noise treatment is deeply discussed in [30] and the *OF* method studied in both time- and frequency-domain. The weights are optimal in the sense that the interesting signal can be extracted from a very noise background if the few reasonable conditions above are met.

Therefore the ultimate point relies in the timing prior. There are two alternatives: the algorithm is provided with a reasonable good prior, and then the weights are calculated once; or the prior is just a raw estimate, but the τ parameter extracted is used as a second prior for a consequent iteration.

The first choice is called *Non-Iterative Optimal Filtering (OF-NI)*, the second, normally implemented with a maximum of 3 iterations, *Iterative Optimal Filtering (OF-Iter)*.

A last discussion is above the goodness of the reconstructed quantities⁴. The more accurate reconstruction is achieved when the prior itself is the real unknown value of τ , because in this case the weights are calculated for the same time at which a sample is taken. In this perfect example, the τ parameter is zero, because the g_i are sampled at the same time they are supposed to be. In a more realistic instance the samples will not be taken at the instant they are supposed to be, that is the same to say that the signal is shifted, hence τ should be different from zero; the more the shift, the less correct are the reconstructed parameters, since the weights are no more optimal. Therefore a measure of the parameter distances from the true values is needed.

The most simple and natural distance is the one that mimics the χ^2 , obtained with the *OF* results:

$$QF = \sum_{i,j} (S_i - Ag_i + A\tau g'_i - p) V_{i,j} (S_j - Ag_j + A\tau g'_j - p)$$

and it is itself a function of time. In order to distinguish it from the standard χ^2 it is called *Quality Factor*. In case the reconstructed quantities are gaussian distributed around their true values the *QF* is a χ^2 variable; otherwise, it can be used as a biased indication of the goodness of the reconstruction.

4.2 Signal reconstruction methods in TileCal

The Optimal Filtering method discussed above is the algorithm that reconstructs the TileCal signal from its samples; the *OF* is implemented inside the DSP (described in Section 3.4.1).

In order to validate and control the online *OF* algorithm, two large classes of algorithms are available for TileCal: the Fit and the *OF* classes.

The Fit class includes a Fit method that reconstructs offline the signal pedestal, amplitude and time from data samples; in the peculiar case of the Charge Injection System (CIS) signal the method performs a sample-by-sample subtraction of the leakage pulse, (introduced in Section 3.5.1), before parameter reconstruction, and repeats this at each iteration. This allows for treating the leakage pulse always as synchronous with the injected signals. The performance of the Fit algorithm has been studied in [25] and a few results have been presented in Section 3.5.1. This has to be taken as the reference method, and the main goal of this work is to validate the online *OF* method using CIS with respect to the Fit.

⁴Namely, this is a more general topic and not only peculiar of the *OF*, since every method reconstructs the parameters with a certain accuracy. Here the emphasis is upon the need of a quality-feedback and the way it is naturally suggested by the *OF* method itself under minimal physical and reasonable requirements.

The *OF* class includes the described Optimal Filtering method in many flavours and with different features. None of these versions has been implemented in order to deal with the leakage pulse.

The *OF-NI* and the *OF-I* are both implemented in the DSPs and also offline. This allows to check that the online algorithms behave correctly and the only admitted differences are those due to the digits truncation in the DSP words. The DSP word described in Table 3.1 is reported here:

G	EEE EEEE EEEE EEEE	PPP PPPP PPPP	F	QQQQ
---	--------------------	---------------	---	------

It is evident that a limit is imposed by the finite number of digits for all the reconstructed quantities; Table 4.1 (adapted from reference [31]) shows the resolution limit for reconstructed amplitude when using online *OF-NI* and different units; the unit change is provided by a linear calibration applied to the reconstructed quantities

Gain	ADC	pC	MeV
LG	0.0625	0.03125	32
HG	0.0625	0.00049	0.5

Table 4.1: Resolution limits for the reconstructed amplitudes inside the DSP using different units, for both the High and the Low Gains

at DSP level. For example if the amplitude is reconstructed in MeV units, the amplitude conversion is obtained with the formula:

$$A[\text{MeV}] = a \left[\frac{\text{MeV}}{\text{ADC}} \right] (b[\text{ADC}] + A[\text{ADC}]) \quad (4.3)$$

hence the relative differences between online and offline amplitudes should fall as $1/E$ if no error is due to the application of the constants a and b in equation 4.3. This is not strictly correct and it will be shown in Section 5.2.

The most important point for the *OF-NI* implementation in TileCal is the timing prior, that allows both to satisfy the condition of the Taylor expansion (Section 4.1.1), and to choose the correct sets of weights. In particular, the time prior (T_{COOL}) is obtained, for each channel and gain, by defining $T_{COOL} = \langle T_{fit} \rangle$ using high statistic data sets with a fixed injected charge (see Chapter 5).

This information define the time (with sign) after $t = 0$ (defined in Section 3.6 as the time of the central sample in the Digitizers) for which the peak of the signal is expected to occur. Obviously this cannot true event by event, therefore the time reconstructed by the Fit, T_{fit} , may be different. If this happens, the TileCal implementation of the *OF-NI* algorithm is such that the DSP calculation returns a value T_{dsp} that is the difference between the actual time and the expected time of the peak.

In conclusion, $T_{dsp} = T_{fit} - T_{COOL}$, at least for T_{fit} not too different from T_{COOL} : the weights are appropriate for the reconstruction to be reliable. This is discussed in Chapters 5 and 6.

All these definitions are described in Figure 4.3: the black points are the pulse

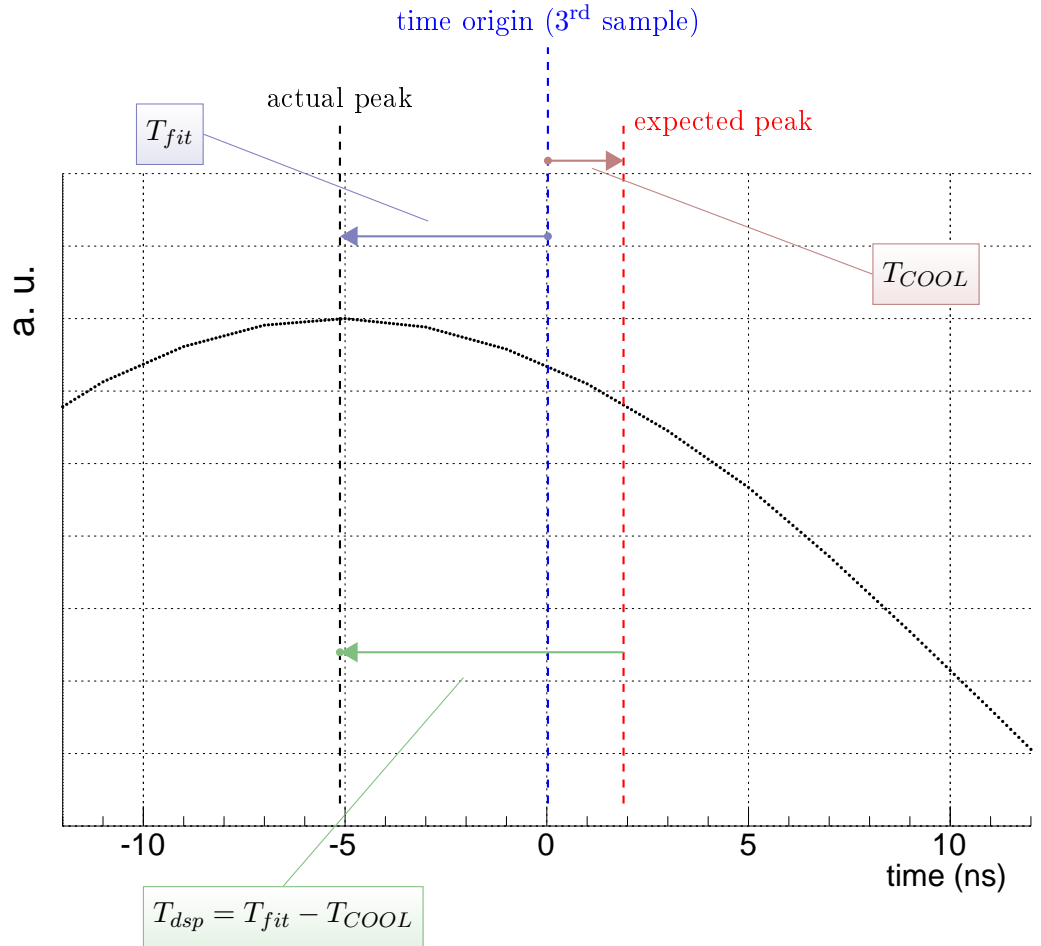


Figure 4.3: Definitions for the *OF-NI* and the Fit methods timings. The black points are a typical CIS signal near the peak, which is expected T_{COOL} ns after the time $t = 0$, that is, after the central sample has been taken; T_{COOL} is calculated during the synchronization described in Section 3.6. For the event depicted, the peak has arrived before than expected, hence the Fit method reconstructs a T_{fit} that is the difference between the time of arrival and the time zero: in this example $T_{fit} < 0$. The *OF-NI*, as it is implemented inside the DSPs, returns the difference between the effective time of arrival and the expected time of arrival: $T_{dsp} = T_{fit} - T_{COOL}$. With reference to Figure 4.2, the τ parameter is different from the TileCal phase; in particular the weights are optimal if and only if $T_{dsp} = 0$.

shape near the $t = 0$, while the dashed lines are the time of the expected peak (in red), T_{COOL} , and the time of the actual peak (in blue), T_{fit} . It is evident that $T_{dsp} \geq 0$ if $T_{fit} \geq T_{COOL}$, that is if the signal injection is delayed with respect to the expected time. Furthermore, the optimal situation occurs when $T_{dsp} = 0$, because there are no residuals.

The T_{dsp} definition is a little puzzling at the beginning, but it is also a good indication of the reconstruction quality: if $|T_{dsp}|$ is too large, the weights are by sure wrong for the data samples, and this can be stated without any knowledge of T_{COOL} . This is first depicted in Figure 4.4 and then described in the next two Chapters.

Furthermore, an offline correction is applied to Physics data in normal reconstruction mode. The origin of this correction relies on the value of the TileCal phase parameter described in the previous Section and on the $OF-NI$ reconstructed amplitude as a function of the phase. Figure 4.4, [32], shows a preliminary study of this kind of corrections. The idea is to recover the results of the offline Iterative Optimal Filtering method for the online $OF-NI$ for events whose reconstructed $OF-NI$ phase is different from zero. The red points clearly show that the Non-Iterative reconstruction is biased if T_{dsp} is different from zero; a second order correction is applied offline and the results are the blue points. Due to the trend of the red points in Figure 4.4, the correction is called *parabolic correction*.

The effect on the energy reconstruction due to a wrong choice of weights can be seen in Figure 4.4, obtained on a data set of proton-proton collisions. The percentage difference between the $OF-NI$ E_{dsp} and the E_{fit} is shown as a function of the t_{dsp} reconstruction: in particular the red points shows that the larger $|t_{dsp}|$, the less accurate the reconstruction.

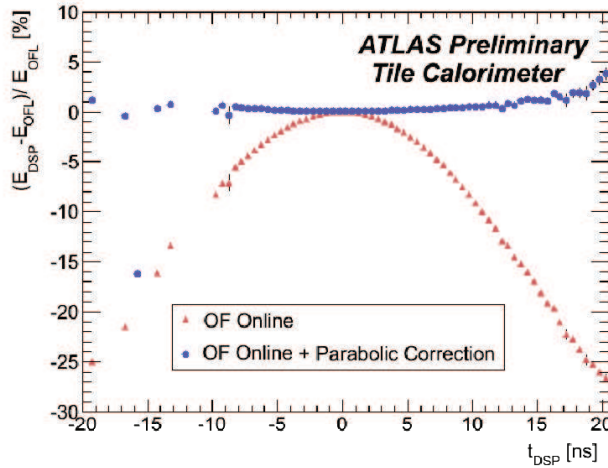


Figure 4.4: Relative differences between Online Non-Iterative and offline Iterative Optimal Filtering amplitudes as a function of the $OF-NI$ phase. The red points refers to the ratio of the amplitudes before the parabolic correction; the blue points are the ratios after the corrections are applied.

4.3 The Calibration Constants

The Fit method has been the standard reconstruction method up to now in TileCal. For this reason the *Calibration Factors* or *Calibration Constants* (the a and b parameters in equation 4.3) that convert the measured signals from ADC to pC or MeV units have been obtained using this method.

A precise calculation of the Calibration Constants is important because they are responsible for the equalization and calibration of the whole calorimeter.

On the other hand, the Optimal Filtering method in its Non-Iterative version is the algorithm that will be used for online reconstruction since it can cope with the very high data acquisition rates. In these conditions the other algorithms are too slow to fit the trigger bandwidths, and data samples cannot be extracted for offline reconstruction. It is therefore vital for TileCal to use the *OF-NI*.

The parameters extracted using the *OF* are in ADC units, hence a conversion is needed to feed the *LVL2* trigger with more appropriate pC or MeV units. The Calibration Constants calculated using the Fit method are therefore applied at DSP level to real data.

The goal of this thesis is the validation of the Non-Iterative Optimal Filtering method and a great effort has been done to quantify the systematics introduced by the application of the Calibration Constants to the online algorithm. The results are presented in the next two Chapters.

Chapter 5

Validation study

In this Chapter the validation study of the Non-Iterative Optimal Filtering using the Charge Injection System data is presented.

The first step is the comparison between the online and the offline implementation of the algorithm, which should differ only for the truncated digits in the ROD words. As a consequence, the degradation in the resolution due to the hardware limitation is evaluated.

The second step is the comparison between the online OF-NI and the Fit methods. The differences between the two are shown, together with the corrections proposed.

The differences between the two algorithms are not completely removed. The residuals are therefore useful to quantify the systematics introduced when the Calibration Constants are applied.

5.1 Conditions and data used in the analysis

The core of this study is the validation of the Optimal Filtering implemented inside the DSP and running in Non-Iterative mode, so it will suffice that the Fit and the *OF-NI* have been implemented consistently. If the equivalence can be demonstrated, it is also demonstrated that, at least in their simplest implementations, the two algorithms are equivalent; if not, the differences between the two are a measurement of the systematics introduced with the application of the Calibration Constants, calculated using the Fit method and used also for the *OF*.

The absence of pile-up has a first important consequence: data samples from a single signal are not too much correlated. Correlation can be anyway present, and it is too be understood¹. As a first step it is assumed that the noise autocorrelation matrix r , introduced in Chapter 4, is a diagonal matrix. Furthermore, the noise contributions in two different samples are supposed to be of the same nature, thus the simplifying hypothesis that $\langle n_i^2 \rangle = \langle n_j^2 \rangle$ is adopted. The r matrix is then a multiple of the identity matrix, and samples are weighted in the Fit method with a constant term, and the *OF* implementation and weight calculations are the simplified version of what described in Chapter 4.

This analysis is usually executed on a set of data, called *run*, which refers to a well-defined period, conditions and options.

¹The correlation between samples is present, and it is easily seen in pedestal data taking.

For what concern the data used in this thesis, two kind of run have been used: the *MonoCis* runs and the *CisRamp* runs. They belong to the set of so-called *calibration runs*. *MonoCis* runs are sequences of CIS injections at fixed charge, gain, capacitor and phase, and are mainly used for the timing synchronization with CIS, as described in Section 3.6. *CisRamp* runs are CIS injections that follow a defined pattern for the injected charge, the capacitor used, the phase. According to [25], the error on the control of the charge injected at the input stage of the shaper using the 100 pF CIS capacitor is below 0.2% for $Q_{inj} \geq 10$ pC, and less than 0.4% for charges above 3 pC.

Both these kinds of runs can be taken applying user-defined options, and units and algorithm parameters can also be chosen. In the following, the adopted options for a set of runs will be explained if needed. The non-linearity corrections illustrated in Section 3.5.1 are never applied to these kind of data; moreover, due to the modest bandwidth needed to store information during calibration runs, also the data samples are available.

Since it has been verified that the small capacitor (5.2 pF) injects the CIS signal with a delay of about 5 ns with respect to the expected time, the data samples acquired with this condition are not taken into account in this work. This choice prevents the *OF-NI* to give wrong results because of the incorrect timing. As a drawback, in this work no analysis will be presented which scans in fine steps the High Gain range.

The runs have been analysed using the ROOT libraries [33], which provide a framework for data processing.

5.2 Online and offline reconstruction

Due to the finite size of DSP words as described in Section 3.4.1 and in Table 3.1, some truncation on the results is occurring. Such a truncation is therefore a limitation to the precision of the online algorithm: the less significant bits for each parameter set the resolution limits. Since a change in units results in a linear function of the amplitude in ADC units, equation 4.3, the resolution can be further degraded during this step. It is important that the reconstruction process does not degrade too much the resolution, otherwise it could dominate any possible systematic effect in some energy range.

The error introduced with the digit truncation inside the DSP can be calculated comparing the online and the offline implementations of the Non-Iterative Optimal Filtering. The offline reconstruction is executed essentially with more precision, thus any difference is interpreted as due to the online algorithm.

A first measurement of this effect can be performed using a *CisRamp* run: this allows to establish a relation between the introduced systematics and the injected charge, scanning the whole energy range.

According to Table 4.1, the last significant bit introduces an error of 0.0625 ADC counts, that is, the differences between the online and offline *OF-NI* implementations should not exceed this number.

Translated to picoCoulomb units this corresponds to a difference at fixed injected charge of ~ 0.00049 pC for the High Gain, ~ 0.03125 pC for the Low Gain (the difference between the two is in this case the 64 amplification factor).

This assumption can be verified with a dedicated CisRamp taken in pC units. For each value of the injected charge an histogram of the quantity $1 - \frac{E_{online}}{E_{offline}}$ is build. The histogram mean is interpreted as the percentage difference between the two algorithms at the chosen injected charge, and its RMS is an estimate of the spread of the distribution².

The procedure is repeated for each channel for a set of different injected charges, in order to test the assumption above with increasing charge. Figure 5.1 shows the result for a single channel. The dashed red lines define the theoretical bound

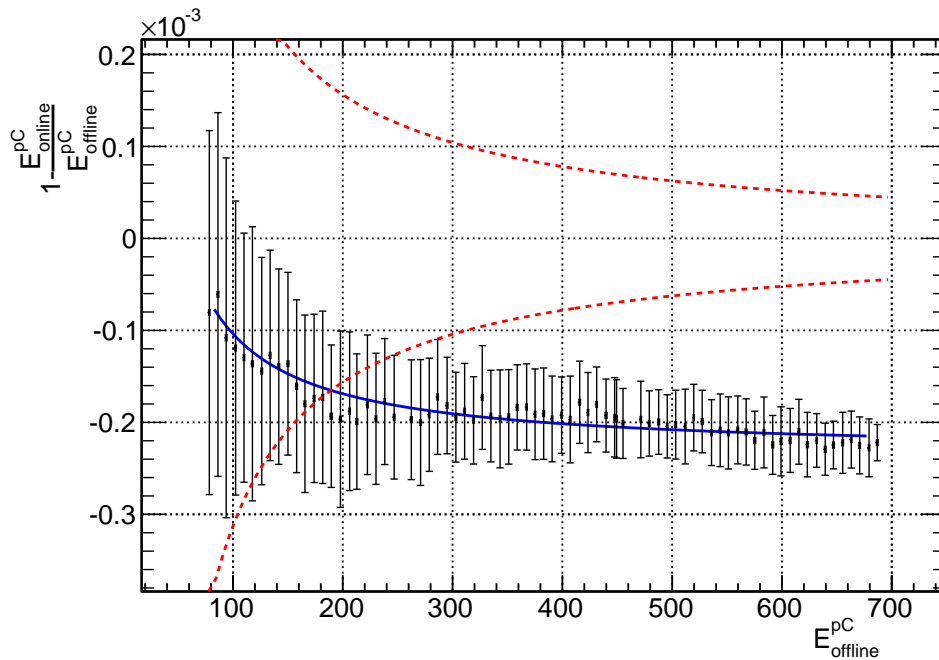


Figure 5.1: Relative differences between the online and the offline *OF-NI* reconstruction for a single channel using the Low Gain branch; the dashed red lines are the maximum overall precision expected from the DSP word length; the solid blue line is a fit to the points with the function $k_1 - \frac{k_2}{E_{offline}^{pC}}$.

inside which the data points should be found if the only difference between the reconstructions is the digit truncation inside the DSP. The experimental points show a sort of systematics that shift the average as the charge increases. This effect is present for each channel in TileCal, and its origin has been traced in the online unit change from ADC to pC at DSP level, described by equation 4.3, with the proper coefficients from ADC to pC.

The online calculation for the unit change is performed by means of a DSP internal look-up table, in which also the conversion factors have limited precision. Therefore, the online and the offline reconstructed quantities include this difference

²The RMS is considered and not the error on the mean, because the RMS gives an idea of the spread of the data around the mean value.

if units other than ADC are used.

Assuming that ϵ_a , ϵ_b and ϵ_A ($\epsilon_A = 0.03125/A$) are the rounding errors respectively for the coefficients a , b and the DSP amplitude A in ADC units, the inherent error of equation 4.3 is at the first order in the rounding errors:

$$\epsilon_{inh} \doteq \epsilon_a + \frac{b\epsilon_b + A\epsilon_A}{b + A}$$

The amplitude offset b is implemented exactly with with the same digits both online and offline; ϵ_b is zero, hence a further approximation can be made:

$$\epsilon_{inh} \simeq \epsilon_a + \frac{0.03125}{A}$$

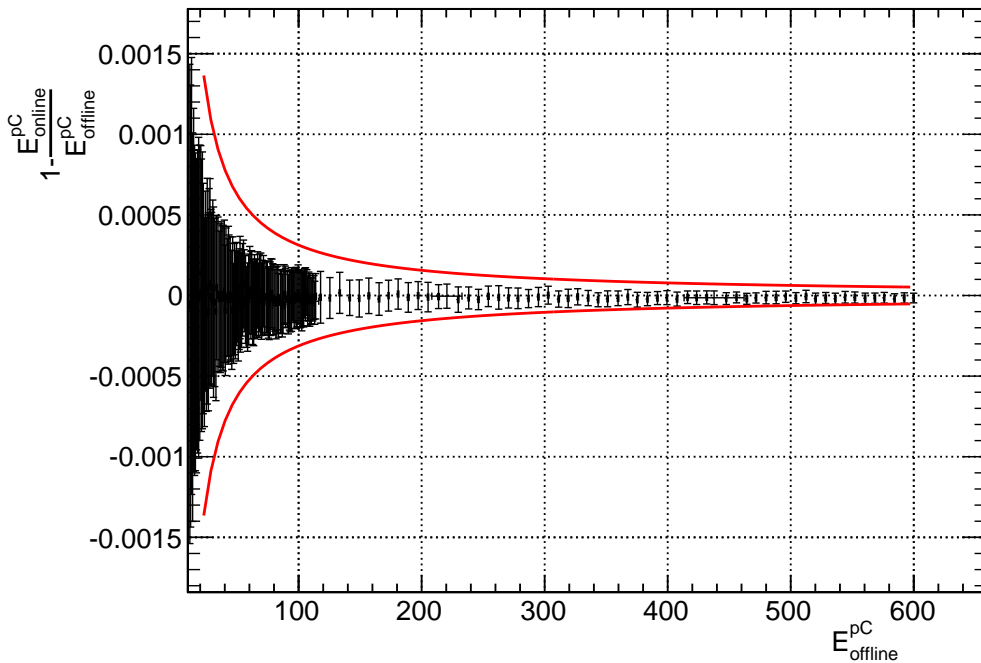


Figure 5.2: Relative differences between the online and the offline *OF-NI* reconstruction for a single channel using the Low Gain branch after the shift described in the text has been performed; the red lines are the maximum overall precision allowed due to the DSP word length.

The inherent error is the propagation of the error due to the digit approximation regardless the error induced by the used algorithm (*algorithmic error* ϵ_{alg}), which in the case of equation 4.3 is limited by the machine precision u . The errors in ϵ_{inh} are not summed in quadrature, since in this case the goal is to consider the maximum error due to a difference in the less significant bits. Hence the relative error in the function in Figure 5.1 is $\epsilon_{tot} = \epsilon_{inh} + \epsilon_{alg}$. Imposing $\epsilon_a = 0$, $\epsilon_b = 0$ and $u = 0$ the result in Table 4.1 is recovered.

The point is now to understand if the new contributions to the relative error ϵ_{tot} are important and degrade the resolution. This can be simply calculated, because E_{online}^{pC} is a linear function of $E_{offline}^{pC}$ (see Appendix A); data are fitted with the function $k_1 - \frac{k_2}{E_{offline}^{pC}}$ in Figure 5.1; the blue line is the fit result.

If the above assumptions are correct, since the k_2 offset is small at higher energies, data points can be shifted of k_1 , aligning the higher energy points to the zero line.

With such a shift the points are not expected to be all aligned, especially at lower energies; however, if ϵ_{inh} is greater than ϵ_A , the error bars should exceed the $\epsilon_A = 0.03125/A$ red lines in Figure 5.1.

This is shown in Figure 5.2: the error bars do not exceed the red lines. The above trend has been verified for all the channels in one of the LBA partition, and the results are shown in Figure 5.3 for a set of channels. Again the overall behavior is consistent with what expected. In the same Figure it seems quite clear that at the beginning of the energy range the point trend is slightly towards the negative values. This has been interpreted as if the approximations discussed in Appendix A do not hold anymore (see the final discussion in the Appendix). As a conclusion, it

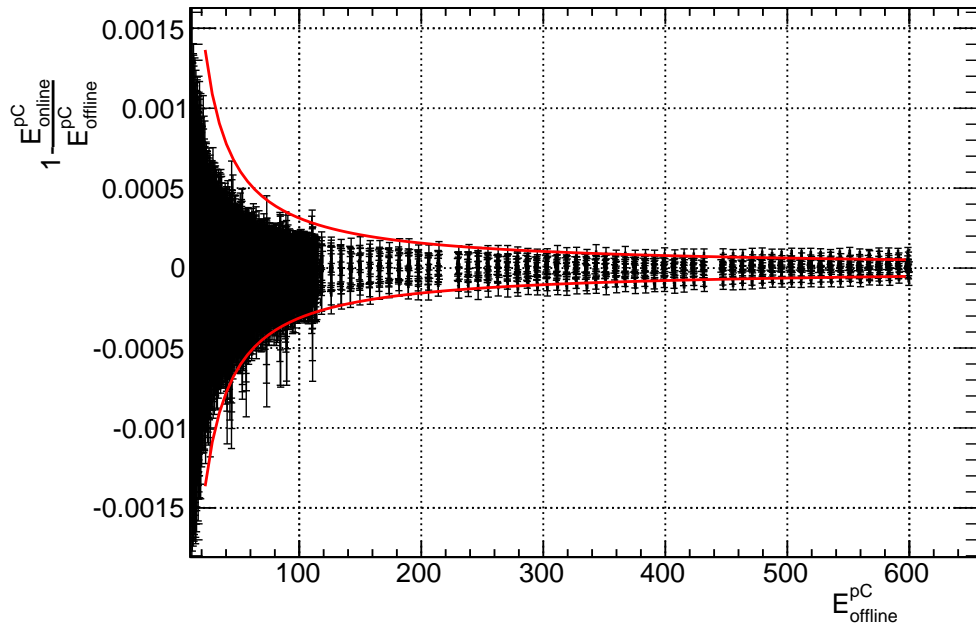


Figure 5.3: Relative differences between the online and the offline *OF-NI* reconstruction for a chunk of channel using the Low Gain branch after translation; the red lines are the maximum overall precision allowed due to the DSP word length. The missing points around ~ 220 pC and ~ 435 pC have been cut due to bad reconstruction flag.

can be stated quite safely that the round-off errors introduced in the look-up table for the online unit conversion are dominated by the hardware limitations due to the finite number of digits inside the DSP. The precision is worst than 0.1% for charges smaller than ~ 20 pC, that is about ~ 20 KeV over 20 GeV.

5.3 Fit linearity and resolution

Being the Fit method the reference method for the TileCal signal reconstruction, it is important to verify that the Non-Iterative Optimal Filtering behaves the same as the Fit. It were not the case, the unit conversion $\text{ADC} \rightarrow \text{pC}$ would be affected by this error.

Figure 5.4 shows the Fit linearity for a single channel in the Low Gain using CIS signals. As pointed out in Section 3.5.1 and shown in Figure 5.4, the Fit is not linear for small injected charges; the non-linearity is recovered inside the DSPs with the Calibration Factors, calculated for $Q_{inj} \geq 300$ pC, and by applying a second order correction which corrects the behavior for small injected charges.

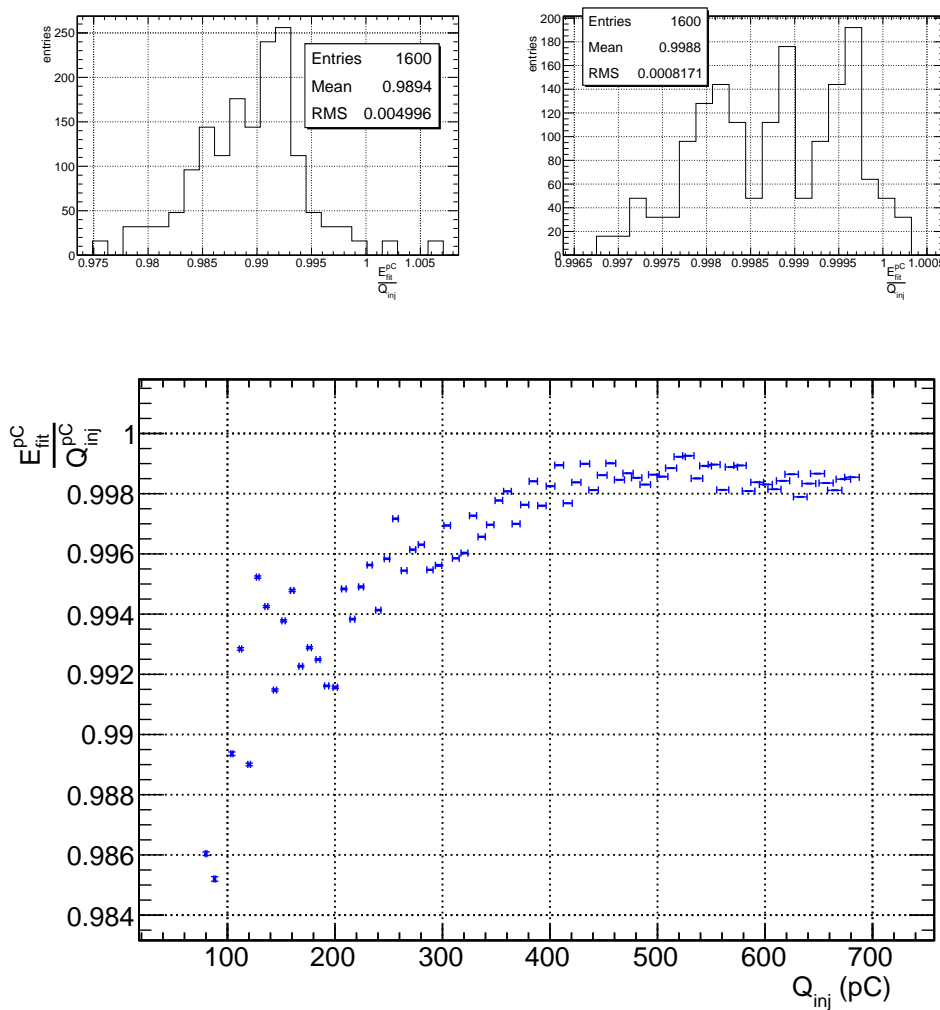


Figure 5.4: Fit linearity in the Low Gain region for one channel. On the top plots, the distributions at fixed Q_{inj} : on the left $Q_{inj} = 80$ pC, on the right $Q_{inj} = 560$ pC. In the bottom plot, the Fit linearity for different injected charges. The vertical error bars are the errors on the mean. As reported in [25] the Fit method is non-linear in the small-injected charge region, near the transition between the High and Low Gain.

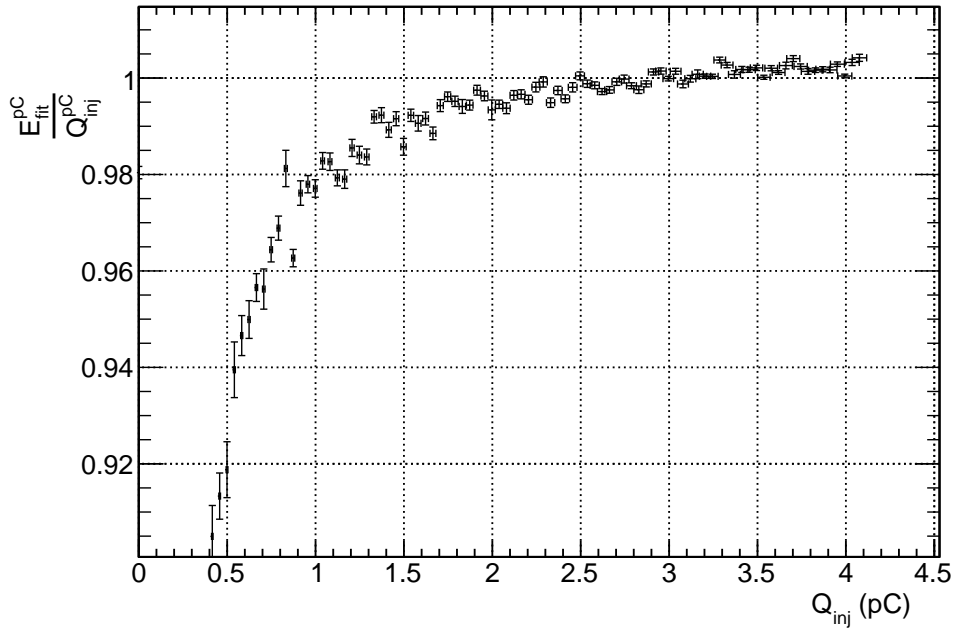


Figure 5.5: Fit linearity in the High Gain region in a very thick scan of low injected charge. The error bars are the errors on the mean. The fit method loses linearity below $Q_{inj} = 1$ pC, most probably this is due to a variation in the pulse shape for small injected charges.

All the corrections described in Section 3.5.1 have been calculated for the Fit method, and here they are assumed to be correct and properly working. The same kind of plot has been made for the High Gain branch for small injected charges: Figure 5.5 shows that in this region the Fit is linear for $Q_{inj} \geq 1$ pC within 1%; the loss in linearity is most probably due a variation in the pulse shape at small Q_{inj} which is not taken into account by the Fit.

Another important point is the resolution of the Fit method, since it sets the intrinsic Fit method limit to the accuracy with which the reconstruction can be achieved.

The Fit resolution can be easily obtained by measuring the E_{fit} distribution for fixed values of the injected charge. The RMS and mean of this distributions are used to build the resolution. The procedure is repeated for each available injected charge, and the results are shown in Figures 5.6 and 5.7, respectively for High and Low Gain, for a whole module.

The vertical axis reports the method resolution $\sigma(E_{fit}) / \langle E_{fit} \rangle$, the horizontal axis the value of the injected charge for which the reconstruction was performed. The Figures 5.6 and 5.7 show that for both gains and for all the channels the resolution is better than 0.7% over the whole Q_{inj} range; the constant term is around 0.1%. The Fit contribution to the resolution is about 600 MeV at 300 GeV. If compared to the goal resolution limit for TileCal $\frac{\sigma_E}{E} = \frac{50\%}{\sqrt{E}} \oplus 1\%$ it is clear that the reconstruction

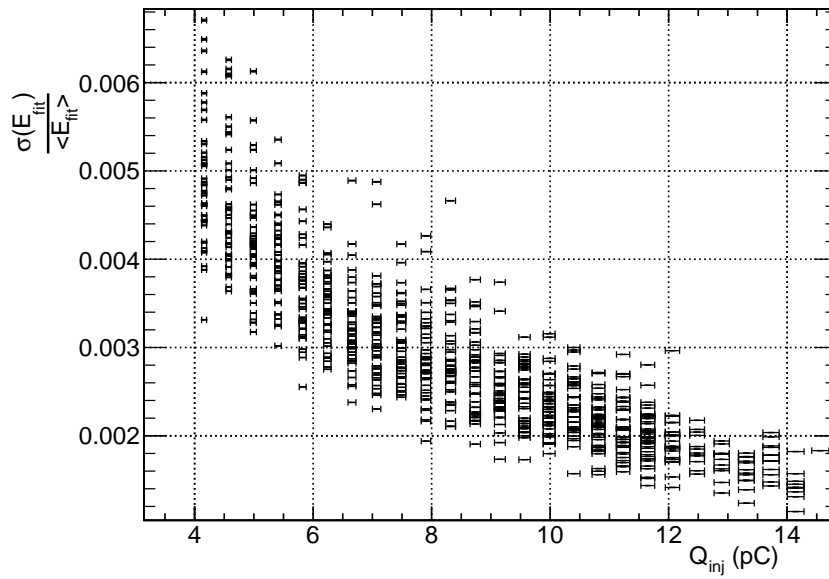


Figure 5.6: Fit resolution in the High Gain branch for a whole module.

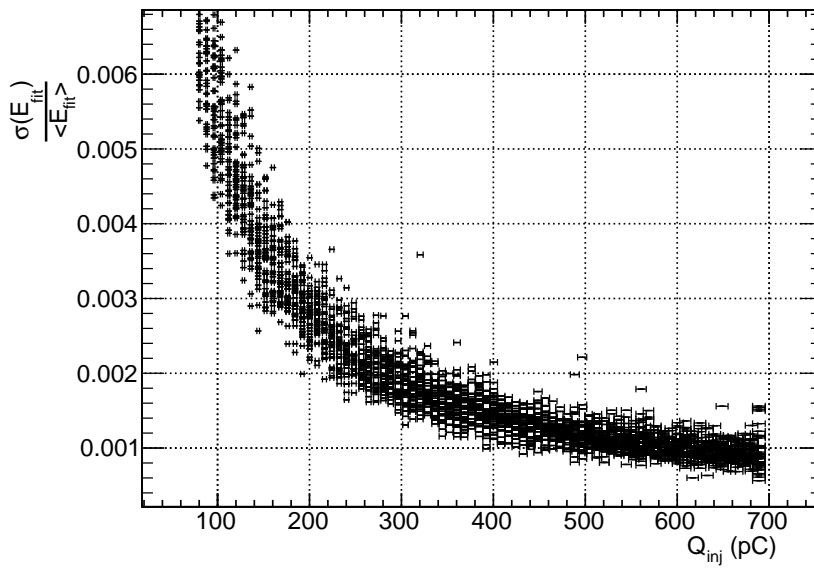


Figure 5.7: Low Gain Fit resolution for a whole module.

does not degrade the resolution.

5.4 Comparison between amplitudes

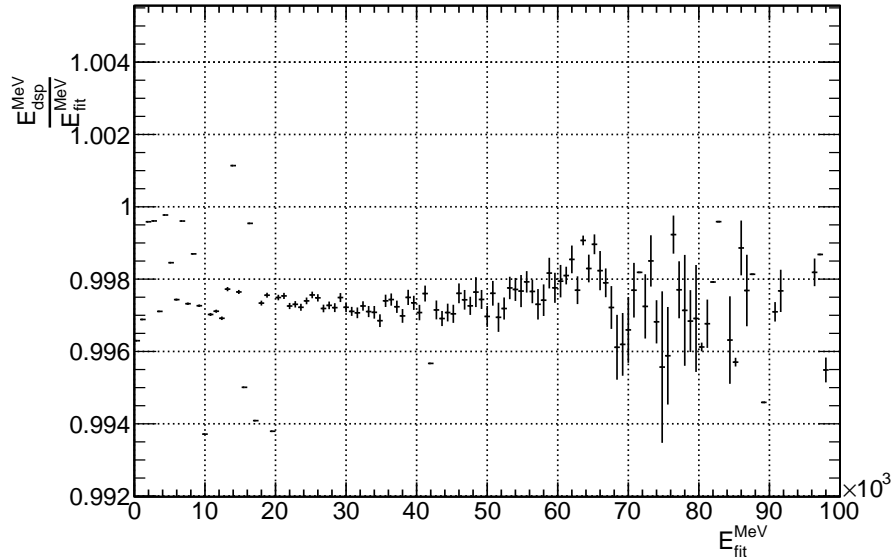


Figure 5.8: Ratio $\frac{E_{dsp}^{MeV}}{E_{fit}^{MeV}}$ as a function of E_{fit}^{MeV} for Physics events at $\sqrt{s} = 7$ TeV; almost all TileCal modules have been used. The full range is shown; the transition region between the High Gain and the Low Gain is visible in the gap around 13 GeV.

In the previous Sections the *OF-NI* resolution limitations due to digit truncation and the Fit intrinsic linearity and resolution have been studied; in this Section the comparison between the two methods is introduced. It is important to stress that for this comparison to make sense each channel has to be properly synchronized as explained in Section 3.6.

A first look at the comparison can be achieved using data obtained from proton-proton collisions at $\sqrt{7}$ TeV which pass the Minimum Bias trigger (Section 3.1): in this case the problem of the leakage pulse is absent. On the other hand, there is no sure reference for the released energy but the Fit amplitude and the energy range that can be studied is limited at smaller energies because of poor statistics.

The Figure 5.8 is a profile plot where on the vertical axis is shown the ratio E_{dsp}/E_{fit} as a function of the reconstructed E_{fit} ; the adopted units are MeV. The analysed events are selected by requiring the correct BCID for each event, and a small value for the reconstructed τ by the *OF-NI*: $|\tau| \leq 3$ ns (see Figure 4.4). This last requirement is to a certain extent equivalent to a cut on the *OF-NI* reconstruction quality, as discussed in Chapter 6. The error bars represents the errors of the mean, and are larger at higher energies due to the poor number of entries; all the TileCal modules and channels with reasonable settings have been used.

The Non-Iterative Optimal Filtering amplitude is linear with respect to the the Fit reconstruction at the level of a few per cent on Physics. The High Gain branch is the most populated region, since in most of events there is a very small energy in

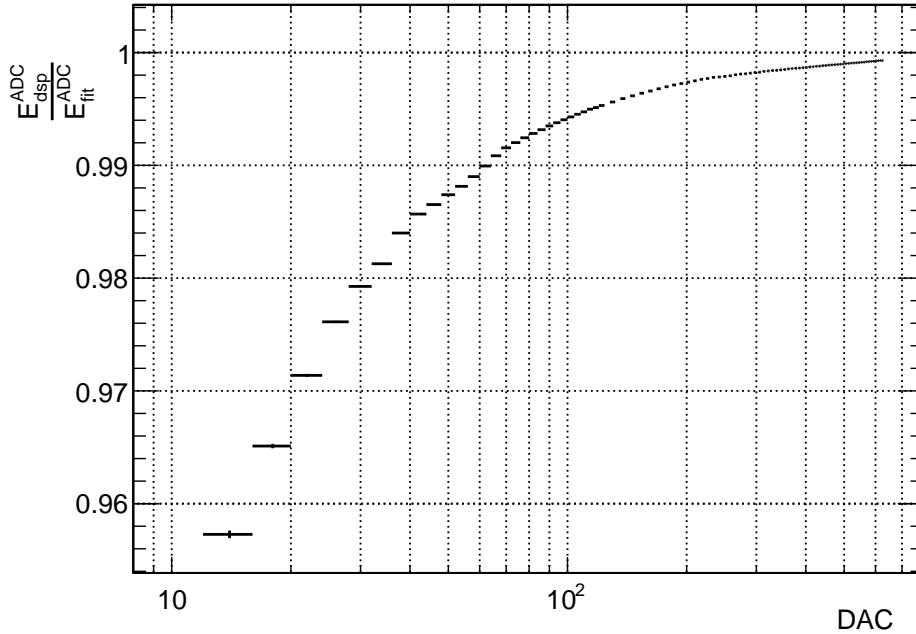


Figure 5.9: Ratio between the *OF-NI* and the Fit amplitudes for a single channel in the Low Gain region using CIS.

the Tile Calorimeter. The higher the energy, the larger the errors on the average, but the two algorithm are equivalent to a level of about 0.4% below 70 GeV.

Figure 5.8 is encouraging, since it implies that the application of the Calibration Factors to the *OF-NI* amplitudes is correct within 0.4% at higher energies, and maybe even better when more statistics is available.

It is therefore quite a surprise to see that the same plots for CIS signals behave very differently. Figure 5.9 $E_{dsp}^{ADC} / E_{fit}^{ADC}$ shows as a function of the CIS DAC settings. At low injected charge the Fit and the *OF-NI* methods are highly non-linear, and the trend improves slightly with increasing charge. This behavior is present for all the channels in TileCal, even if some differences are present.

5.4.1 Understanding the CIS behavior

The great difference between the Fit and the *OF-NI* method is the way the leakage pulse is treated. The leakage pulse for each capacitor and gain is shown in Figure 3.11 and as explained in Section 4.2 only the Fit algorithm takes into account for it.

Therefore the first source of discrepancy between the two methods has to be found in this difference: the Fit method subtracts the leakage pulse before minimizing the χ^2 , the standard *OF* does not. A part of this thesis has been the understanding and the treatment of these differences.

Assuming that the synchronization has been properly set for one channel, the T_{COOL} values (Section 4.2) for that channel are assumed to be the times at which the maximum occurs for both the High and Low Gain after injection. Since the

leakage pulse is synchronous with the charge injection, the T_{COOL} time is also the time for the injection of the leakage pulse.

The leakage pulse shape shown in Figure 3.11 can then be used to evaluate the amplitude at each sample and then subtracted from the signal. After this procedure has been applied, the standard reconstruction can be performed in more reliable conditions.

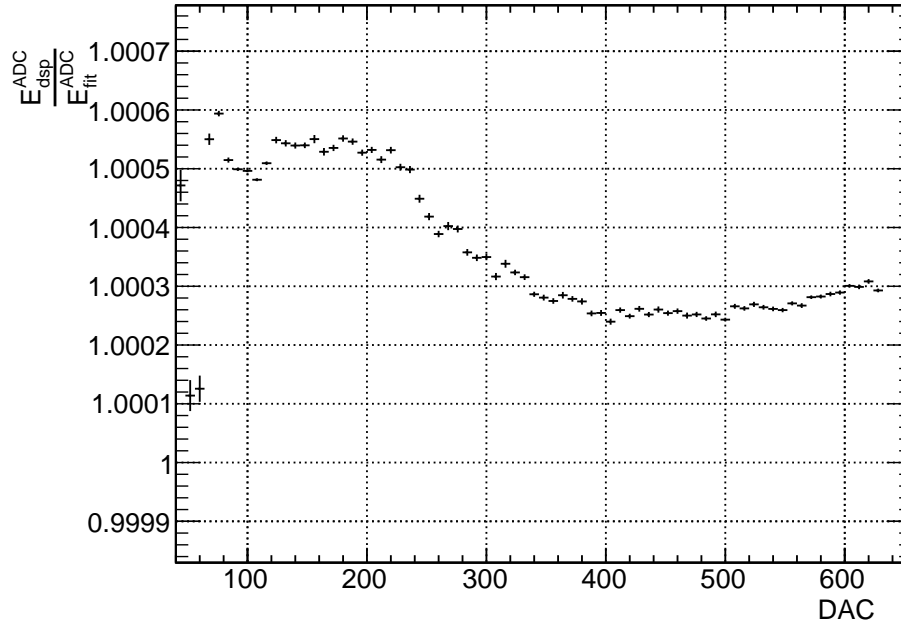


Figure 5.10: Ratio between the *OF-NI* and the Fit amplitudes for a single channel in the Low Gain region using CIS after leakage pulse subtraction.

In Figure 5.10 this task has been executed for one channel in the Low Gain branch for CIS signals as a function of the DAC setting.

It is noticeable that after such a correction the linearity between the two methods is recovered at the level of a few per mille: the maximum gap is about 0.5%. It can thus be stated that the leakage pulse is responsible for a non-linearity of a few per cent between the Fit and the *OF-NI* when looking at the Low Gain region.

The same procedure can be applied to the High Gain branch. In Figure 5.11 the results are shown: the red points are the comparison between the methods without the leakage subtraction, while the blue ones are after the subtraction. The linearity is recovered, but not completely, especially at very low injected charges the difference is still up to 10%.

This is an important point, since if the difference is due to a difference in the algorithm, then the application of the Calibration Factors to the High Gain branch using the CIS signals would in this case create a bias in the measured energy.

A possible solution is to be searched in the leakage pulse. Figure 5.12 is the pulse shape for the leakage in the High Gain region with the 100 pF capacitor. There are

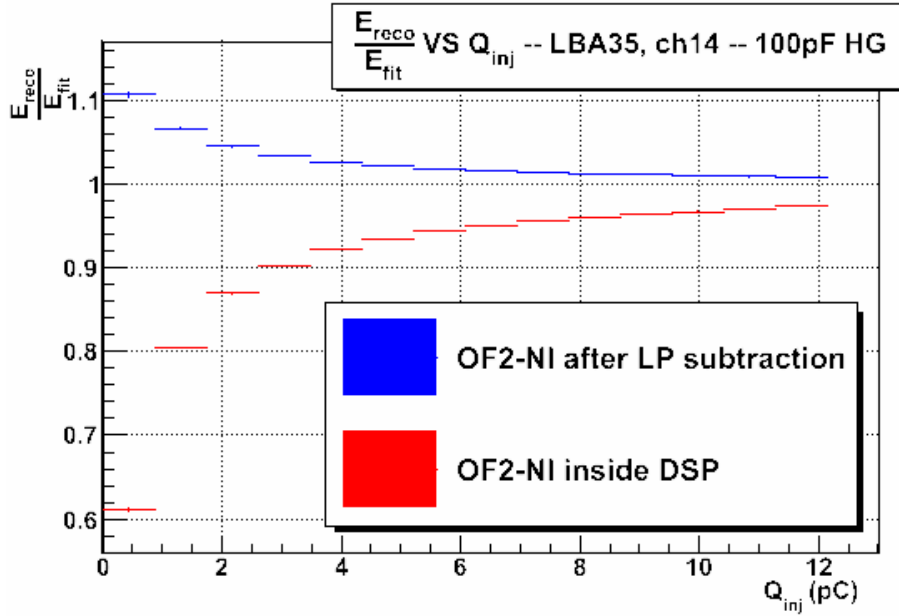


Figure 5.11: Ratio between the *OF-NI* and the Fit amplitudes for a single channel in the High Gain region using CIS; the red points refer to the standard *OF-NI*; the blue points are the results after leakage pulse subtraction.

two remarkable points here. First of all, between the maximum and the minimum, the leakage pulse can be easily described as a linear function; second, the leakage pulse amplitude does not scale with the injected charge, and the number of ADC counts at fixed time is always constant.

These two points could lead the *OF* reconstruction to some mistakes. In particular, a little shift in the timing can result in a large wrong subtraction of the leakage pulse, especially when the injected charge is small. Therefore, an improvement may appear if the value of T_{fit} is used instead T_{COOL} for the leakage pulse subtraction. It should be stressed that such a procedure is not a proposal for changing the algorithm; it is instead a way to try a recovery and to understand the discrepancies observed in the signal reconstructions.

Figure 5.13 shows the result of this second correction. Apart the very low injected charge, for $DAC > 2$, that is $Q_{inj} \geq 1.5$ pC, the two algorithms return results that are consistent within 0.5%, at least for this channel.

In conclusion, the effect of the leakage pulse deteriorates the *OF* reconstruction at the level of a few per cent in the Low Gain region and up to 10% in the High Gain. A raw treatment of the leakage pulse, on the other hand, allows for a great improvement in both the region, thus confirming to a certain extent the agreement between the two methods obtained with Physics data in Figure 5.8.

5.4.2 The reverse correction

For the Low Gain branch only it has been possible to reverse the correction described in Section 5.4.1 by turning off the leakage pulse treatment in the Fit method

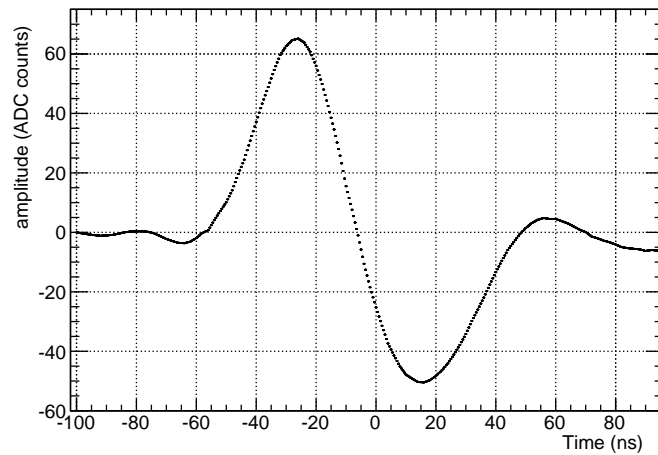


Figure 5.12: Leakage pulse for the High Gain branch using the 100 pF capacitor.

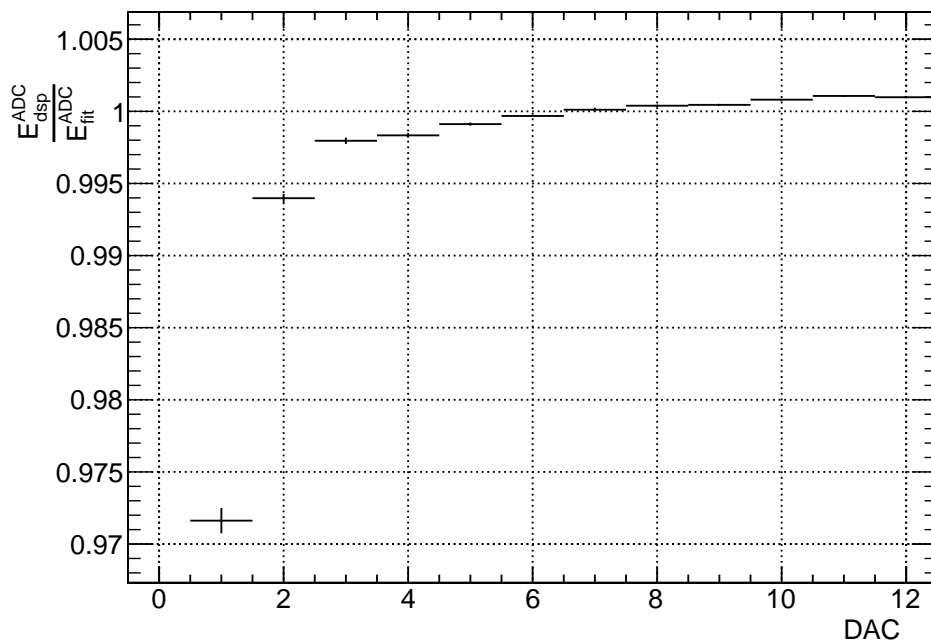


Figure 5.13: Ratio between the *OF-NI* and the Fit amplitudes for a single channel in the High Gain region using CIS after optimal leakage pulse subtraction.

algorithm. If the interpretations and the corrections proposed are correct, then this reverse correction³ should give the similar results as those in Figure 5.10. The com-

³ *Reverse correction* is not an official name. It is used here to stress the fact that the Fit method has been worsened in order to be comparable with the *OF-NI*. This is the opposite of what has

parison with Figure 5.10 is not strictly correct, since the Fit method is anyway iterative; the reverse correction should be taken as an indication of the importance of the leakage pulse for what concern the amplitude reconstruction.

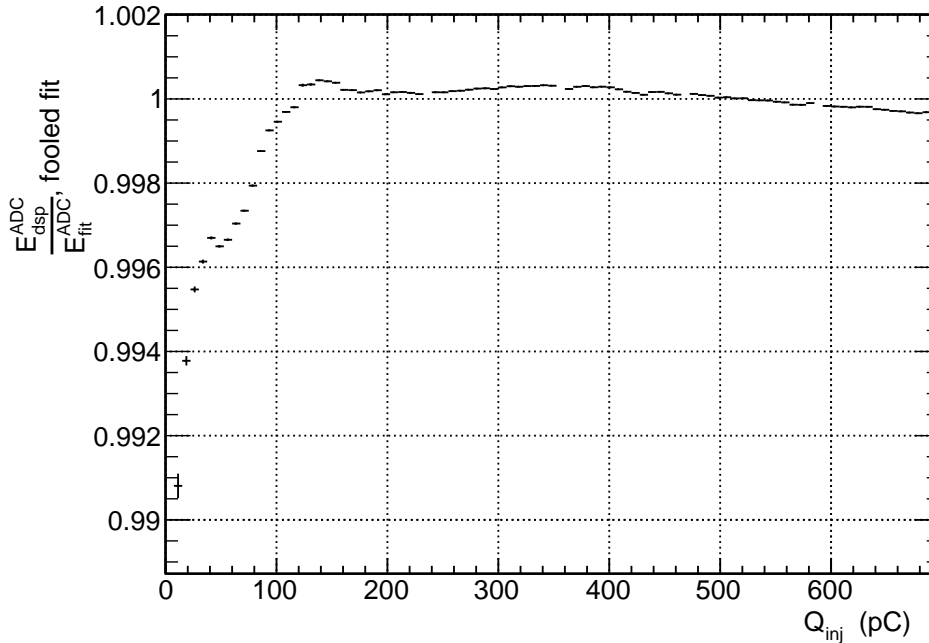


Figure 5.14: Ratio between the *OF-NI* and the Fit amplitudes for a single channel in the Low Gain region using CIS. The Fit method has been fooled and do not consider the leakage pulse. The results are in accordance with what shown in Figure 5.10.

The result is shown in Figure 5.14 for a single channel. The linearity between the two methods is recovered again at the level of a few per mille, thus this is a confirmation that the leakage pulse biases the *OF* reconstruction and as a consequence the time for which the weights are calculated are heavily affected, especially in the High Gain region. The reverse correction for this region is currently not available, but it would be interesting to have a feed-back response also for this configuration.

5.5 Systematics

The linearity of the two methods is not recovered at the beginning of both the Low Gain and the High Gain regions as depicted in Figures 5.10 and 5.13. This introduces a systematic error when the Calibration Factors are applied, unless a deeper understanding of the two algorithms is achieved.

The point is now to quantify the systematics due to the application of the Calibration Factors. Since the level of equivalence between the *OF-NI* and the Fit methods is a function of the injected charge, the systematic error itself decreases as the charge is larger.

been proposed in Section 5.4.1.

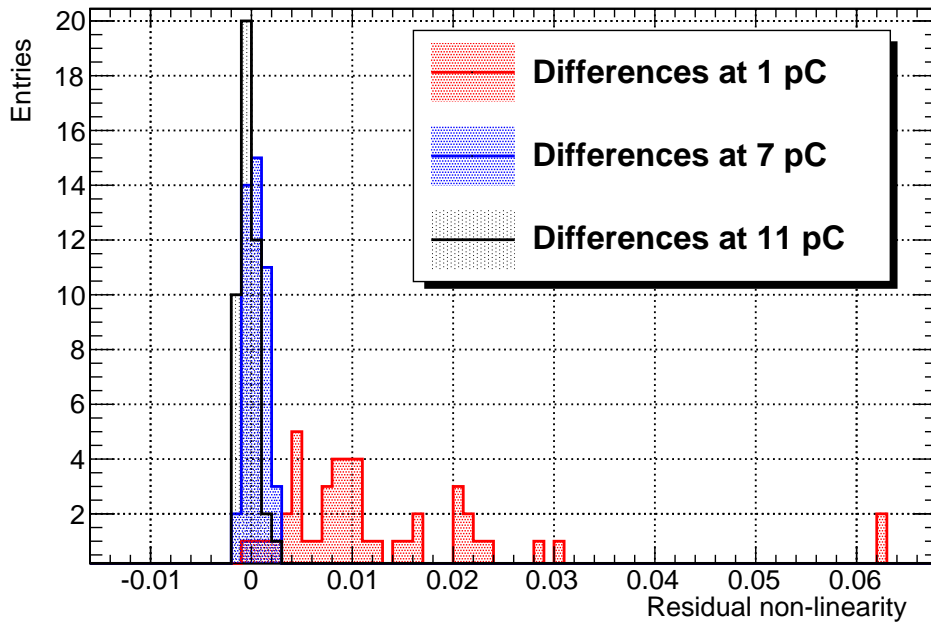


Figure 5.15: Residuals of non-linearities inside a module for the High Gain branch.

The improved reconstruction described in the Section 5.4 has been performed for an entire partition. After that, the non-linearity for each channel has been evaluated at three injected charge values, namely 1 pC, 7 pC and 11 pC for the High Gain, 40 pC, 200 pC and 500 pC for the Low Gain. The values for a whole module are summarized in three different distributions: the smaller the mean value for a distribution, the better the accordance between the Fit and the *OF-NI* for that module near the Q_{inj} . The expectation is that the lower the injected charge, the larger the disaccordance, that is, the larger the introduced systematics.

Figures 5.15 and 5.16 show respectively the distributions for the High Gain and the Low Gain.

The red distributions are for the smallest charges, 1 pC and 40 pC respectively, and are the largest in their groups; this is consistent with what expected and described in Figures 5.15 and 5.16; anyway, the Low Gain region does not require a second order correction, the distributions in this region are more similar than in the High Gain range. Moreover, for the smallest charges, the residual non-linearities are always greater than zero for both gains. This is an important indication, since the *OF-NI* that takes into account the leakage pulse reconstructs always a smaller amplitude than the Fit method at low injected charges.

In conclusion, the systematics introduced by the non complete understanding of the Optimal Filtering and the Fit method is always in the same direction (at least for this module) for small q_{inj} .

For higher charges the residual non-linearity between the methods is more symmetric with respect to the ideal zero value and narrower; this again is compatible

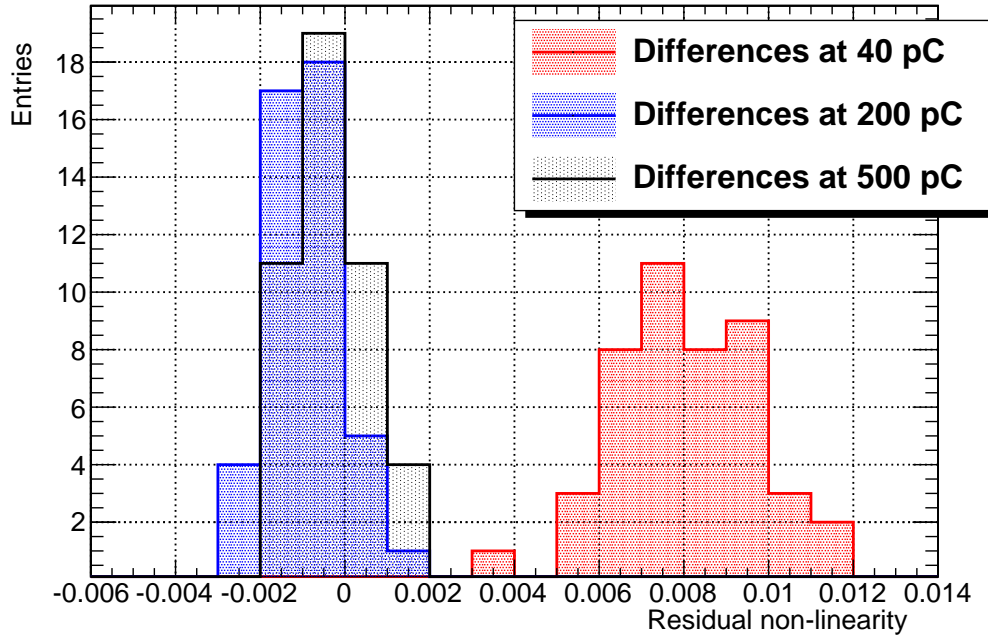


Figure 5.16: Residuals of non-linearities inside a module for the Low Gain branch.

with Figures 5.15 and 5.15.

The distributions of the residual non-linearities suggest also a method to quantify on a larger scale the equivalence between the algorithms. The average and the RMS of each distribution can be interpreted as the mean residual and its spread for a single module; for example, the expectation from Figure 5.16 is that at about 40 pC the mean discordance between the two methods is about 0.8%-1%, with a spread between channels equal to $\sim 0.5\%$; therefore, it is reasonable that for this module some channels have slightly larger residuals, and thus a more important contribution to the systematics.

Figures 5.17 and 5.18 show the mean residuals and their RMSs for a whole partition for $Q_{inj} = 1$ pC and $Q_{inj} = 40$, respectively for High Gain and Low Gain.

The Low Gain sector is more stable than the High Gain one, but the spread for very low injected charges is the same for the two branches. This could be interpreted as an effect of a non complete understanding of the two methods; in particular, the Fit method makes use also of the leakage derivative information in order to subtract its contributions to the data samples, while the improved *OF-NI* presented in Section 5.4 treats only the pulse shape.

According to Figures 5.17 and 5.18 the systematics introduced by the Calibration Factors is around 2% for the High Gain, about 0.5% in the Low Gain region.

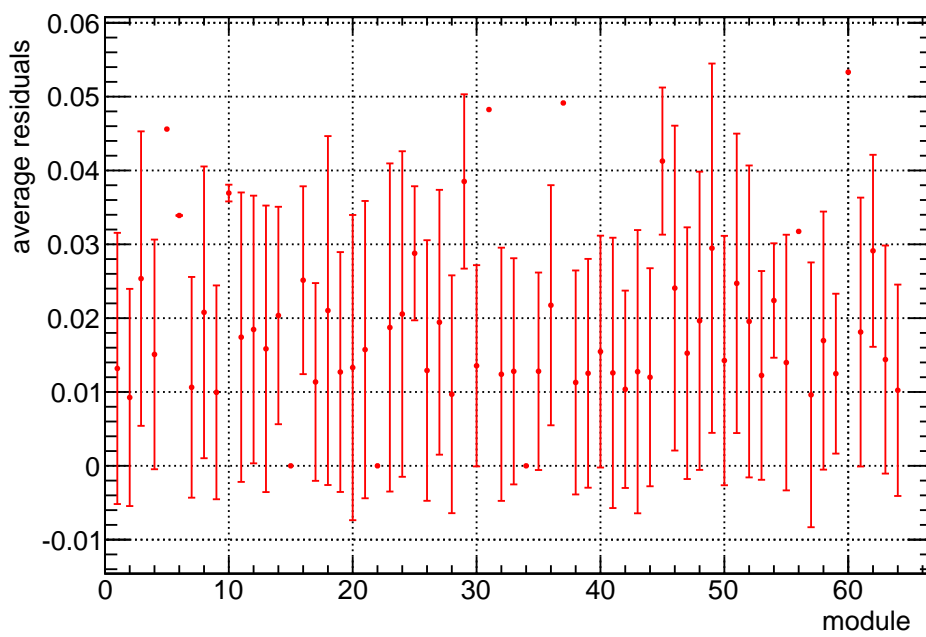


Figure 5.17: Residuals of non-linearities as a function of the module number for the High Gain branch. The three isolated points with zero residuals are the channels non-equipped with electronics (see Section 3.3.1); the others outliers with no error bars have a very large RMS; these are still to be understood, and for the moment only the residuals are shown.

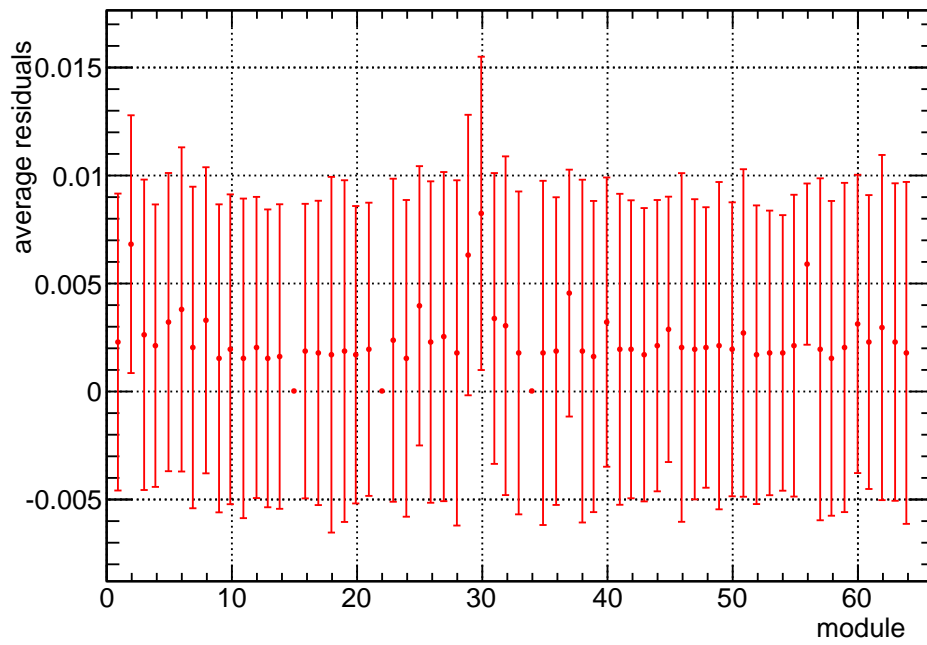


Figure 5.18: Residuals of non-linearities as a function of the module number for the Low Gain branch.

Chapter 6

A proposal to monitor the time setting

The Non-Iterative Optimal Filtering method implemented for TileCal relies on an appropriate synchronization of signals and samplings. Moreover, the reconstruction quality with respect to the Fit method depends strongly on a good choice for the OF weights.

In this Chapter some studies on the reconstructed time with the Fit method are presented; the results will lead to the importance of the time stability for each single channel.

In the second part of the Chapter, a proposal to monitor the time setting is described, together with the most important variables to look at in order to assure the stability over time.

6.1 Timing behavior

In the previous Chapter the validation of the TileCal signal reconstruction has been described; as illustrated in Chapter 4 the Optimal Filtering performances are deeply correlated to the time prior used to calculate the *OF* weights. In particular, if the timing is not correct for one channel, the reconstructed amplitude for that channel will not be correct, since the weights are wrongly chosen. The error scales with the distance between T_{fit} and τ .

It is therefore important to have under control or at least understand the most important sources of systematics that may lead to a wrong weight choice.

In this Chapter the importance of the time stability is presented, and the relation between the timing and the quality of the reconstructed amplitude is shown. It is also shown how the peak time and the peak amplitude are correlated.

The synchronization described in Section 3.6 makes use of a MonoCis run for High and Low Gain, that is, for each channel two numbers are calculated at fixed injected charge. The relation between the peak time and the peak amplitude can be studied by means of the time reconstructed by the Fit method as a function of Q_{inj} .

Figure 6.1 shows the trend of T_{fit} as a function of the injected charge for a CisRamp run in the Low Gain region. The plot refers to a single channel; different channels behave almost the same, with data points merely translated on the vertical

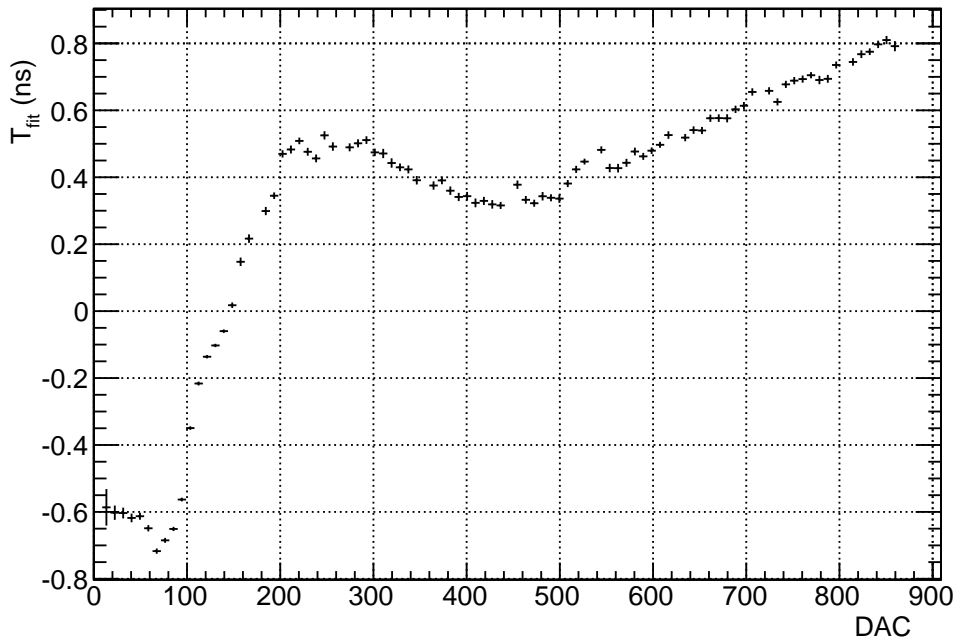


Figure 6.1: T_{fit} trend as a function of the injected charge for a single channel, Low Gain. The total time range is about 1 ns.

axis. In the ideal case T_{fit} should not depend on the injected charge, while it is evident that the reconstructed time increases for increasing injected charge. Three regions can be depicted: the low-energy region, the central region and the increasing region.

The low-energy region refers to the injected charge range from ~ 20 pC (DAC=25) to ~ 160 pC (DAC=200), and it is characterized by the 2% energy non-linearity reported in Section 3.5.1 and [25]. As a rule of thumb, in this region T_{fit} increases of about one nanosecond if the Fit gets rid of the leakage pulse.

The central region is in the range between DAC $\simeq 250$ and DAC $\simeq 500$, where T_{fit} is constant within $0.3 \div 0.4$ ns. Thus this is quite an optimal region, since the time of the signal peak is expected to be constant here, and the calculated weights can be safely applied.

The increasing region is the final part of Figure 6.1 for higher injected charges. The timing reconstructed by the Fit method increases more or less linearly with Q_{inj} , and the range of reconstructed timings is about $\Delta \simeq 0.5$ ns.

The T_{fit} trend has been interpreted as a slight pulse shape variation as the charge increases plus a possible effect of the Fit non-linearity in the low- Q_{inj} region. These effects provide for a global T_{fit} drift of about 1 ns or more if the leakage pulse is subtracted.

A standard MonoCis run for timing correction in the Low Gain branch is typically taken at $Q_{inj} \simeq 96$ pC (DAC = 120), in the middle of the non-linear region. Therefore, it has been proposed to take MonoCis runs at a higher Q_{inj} ; currently the

TileCal T_{COOL} values are calculated at $DAC = 512$, that is at $Q_{inj} \simeq 410$ pC, and the leakage is subtracted. This choice has been preferred because it sets the T_{COOL} for the Low Gain branch more or less in the middle of the T_{fit} flat region. The T_{COOL} value for Low Gain and for the channel in Figure 6.1 is about $T_{COOL}^{LG} \simeq 0.53$ ns.

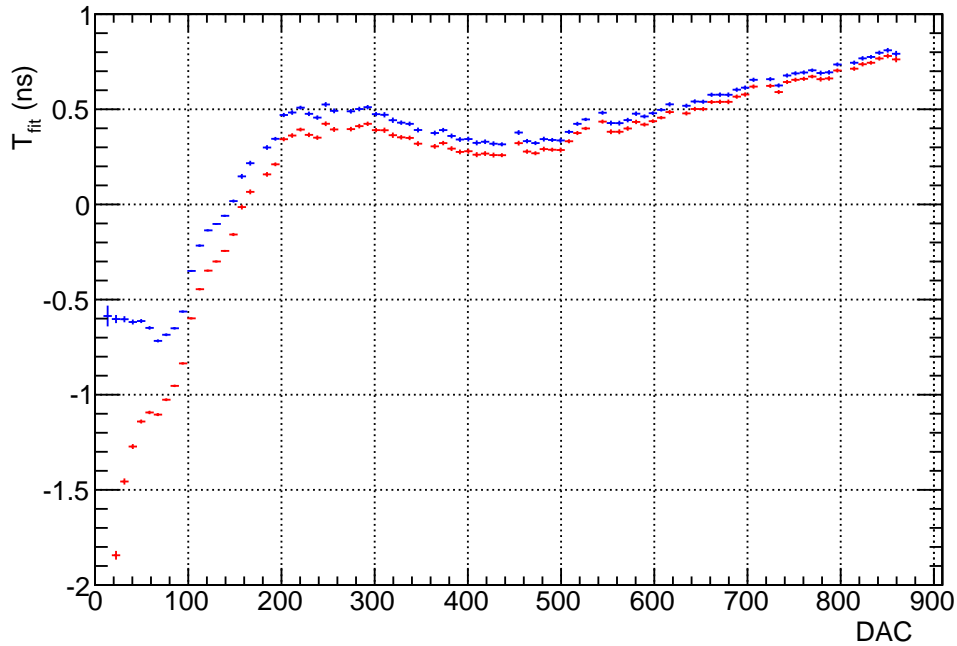


Figure 6.2: T_{fit} for a the standard CisRamp run as a function of the injected charge; the result refers to a single channel, Low Gain. The blue points are the same of Figure 6.1; for the red points the Fit method has been fooled and does not take care of the leakage pulse. The effect of the leakage pulse is clearly to enlarge the time drift of T_{fit} at low injected charges.

The effect of the leakage pulse on the peak time variation as a function of the injected charge varies of a few hundredth picoseconds. The effect of this drift given on the OF reconstruction for which the weights are chosen at a fixed time is discussed at the end of this Section.

This is shown in Figure 6.2, which refers to the same channel of Figure 6.1. The red points refers to the Fit time reconstruction when the leakage pulse is not taken into account. The effect of the subtraction is more evident for $DAC < 100$.

If the leakage pulse is not subtracted, the time is wrongly estimated only for very low injected charges in the Low Gain region. The expectation is that, even if the pulse shape is not correctly treated (due to the leakage pulse contribution), if an injection occurs in which $T_{fit} \simeq T_{COOL}^{LG}$ and Q_{inj} is sufficiently large to forget the leakage pulse, then the *OF-NI* reconstruction should be optimal. In conclusion, if $T_{fit} \simeq T_{COOL}^{LG}$ and $Q_{inj} \geq 200$ pC (central region), T_{dsp} is zero and E_{dsp} is optimal.

Figure 6.3 verifies this assumption using the fooled-Fit in order to properly com-

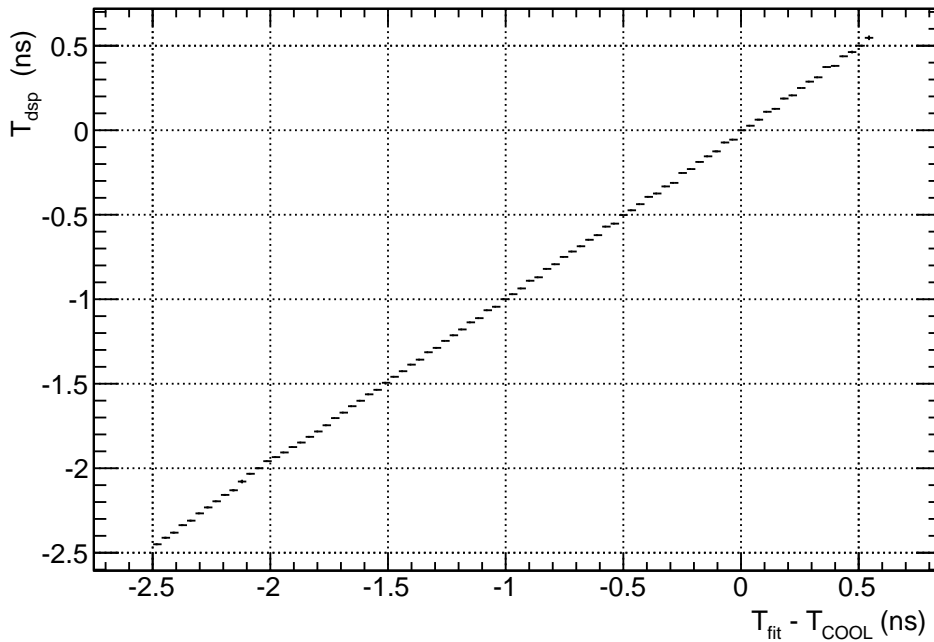


Figure 6.3: The comparison between the T_{dsp} and the difference $T_{fit}^{fooled} - T_{COOL}$ for a standard CisRamp run; the result refers to a single channel, Low Gain.

pare the two reconstruction methods. On the vertical axis the *OF-NI* reconstructed time is reported, in abscissa the difference $T_{fit} - T_{COOL}$, restricted at the region $T_{fit} \geq -2$. The requirement that $|T_{fit} - T_{COOL}| \leq 0.5$ ns fixes the Q_{inj} approximately greater than ~ 100 pC ($0 < T_{fit} < 1$ ns), see Figure 6.1, so it is quite a loose cut.

The difference $T_{fit} - T_{COOL}$ is equal to T_{dsp} , as expected; for example, if $T_{fit} = -0.5$ ns, the Fit information means that the signal has been injected half a nanosecond before the central sampling has occurred, that is, 1 ns before the expected time. Therefore $T_{dsp} = -1$ ns, as correctly reported in Figure 6.3. This result is not to be taken for granted, since the leakage pulse has not been subtracted from the samples and the cut on the charge is loose.

Figure 6.4 shows the effect on the reconstructed *OF-NI* amplitude given by the time drift. The vertical axis reports the ratio between the Fit and the *OF-NI* amplitudes, when none of them deals with the leakage pulse; this is the same ratio shown in Figure 5.14. On the horizontal axis T_{dsp} is reported. The red points are relative to the whole range of injected charge, and it is clear that the accordance between the Fit and the *OF-NI* amplitudes is a function of the time reconstructed inside the Digital Signal Processors; in particular, the two methods give the same results within 0.5% if $T_{dsp} > -2$ ns, that is, if the signal peak is less than 2 ns in advance with respect to the expected value; this in its turn means that the $E_{dsp}/E_{fit} > 0.995$ if the signal peak is less than 1.5 ns in advance with respect to the sampling instant for the central sample.

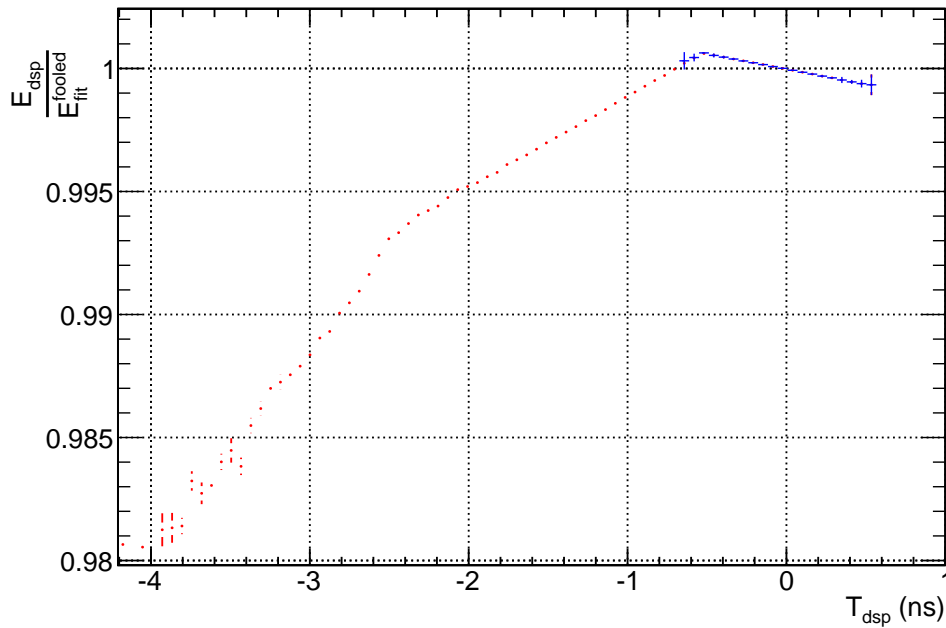


Figure 6.4: The ratio between the *OF-NI* and the Fit method amplitudes for a single channel in the Low Gain branch. The Fit reconstruction is the one described in Figure 5.14, for which the leakage pulse has not been subtracted. The horizontal axis reports the time reconstructed by the *OF-NI* algorithm. The red points refers to the whole Q_{inj} range, the blue points are for $Q_{inj} \geq 160$ pC. It is evident that a cut on the charge is equivalent to a cut in time, and therefore also in the reconstruction quality.

The blue points in Figure 6.4 represent the entries for $DAC > 200$ ($Q_{inj} > 160$ pC). This cut is very efficient to select the region with a good linearity between the methods (see Figure 5.14), and also selects the region in which T_{dsp} is near zero. It is very important to stress that if $T_{dsp} = 0$, then $T_{fit} = T_{COOL}^{LG}$, thus the signal is sampled exactly when expected; therefore the application of the weights is strictly correct, and the amplitude is reconstructed exactly like in the Fit method¹.

In conclusion, the Non-Iterative Optimal Filtering and the Fit methods are equivalent if they have the same implementations and if the T_{COOLS} are correctly set. Although the first point can be quite easily reached, and it holds for sure when dealing with Physics events instead of CIS, the timing requirements depend on the fluctuations of the time of arrival of the signals and on the time stability of the system.

¹This has to be verified also for the High Gain region. This part is quite unlucky, since the High Gain region is the most populated in terms of number of events, and it is mostly affected by timing problems due to the leakage pulse, as described in Section 5.4.1. Furthermore, it seems to be difficult to fool the Fit method for the High Gain region and force it to not care about the leakage pulse.

6.2 The Timing Monitor for TileCal

The last discussion in the previous Section has pointed out the importance of a good timing setting together with a reliable timing stability in order to trust the *OF-NI* reconstruction. Also, since the T_{COOL} values depend on the $\langle T_{fit} \rangle$ calculated using MonoCis runs, it is vital to monitor and understand the behavior of T_{fit} for each channel over time.

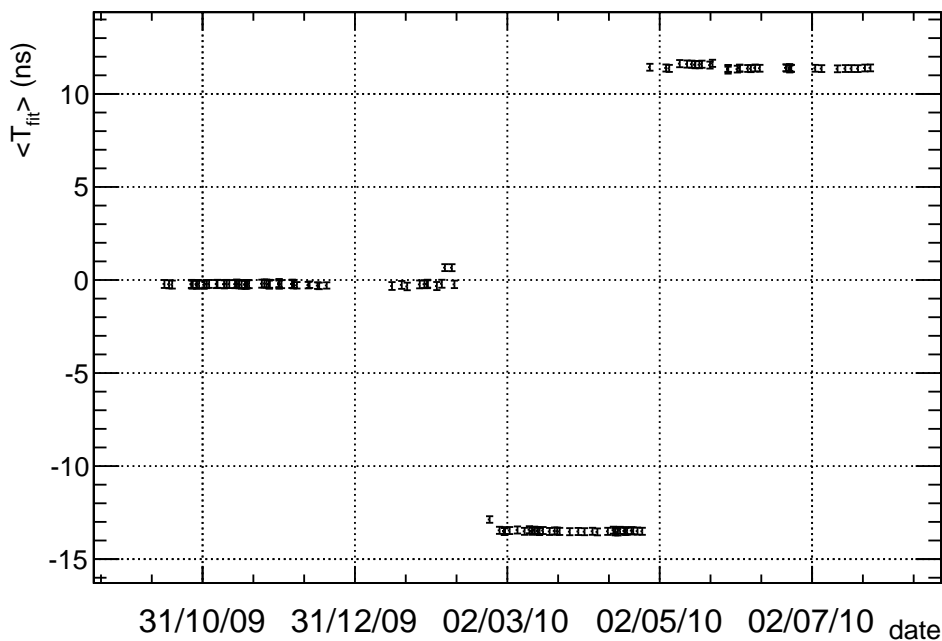


Figure 6.5: Example of a time monitor for a single channel: the horizontal axis is the date at which the run has been acquired, the vertical axis refers to the $\langle T_{fit} \rangle$ for that run. Two *dskew2* update are evident at the end of February and at the beginning of May for the Digitizer to which this channel belongs.

The most simple way to do this is the proposed Timing Monitor of Figure 6.5. Only standard MonoCis runs taken in Low Gain mode are used for this kind of plots, so it must be clear that, although T_{COOL} is calculated using MonoCis runs with $DAC = 512$, the setting is monitored using MonoCis runs with $DAC = 120^2$. This is not a big trouble, since the important feature is the stability of the settings, and not the absolute value of the timings.

The Monitor (plotted for a single channel in Figure 6.5) has on the horizontal axis the date at which the runs have been acquired, while on the vertical axis the T_{fit} average is depicted with its RMS for each MonoCis run that have been used.

²The best choice would have been to set the standard MonoCis runs to the same DAC used to calculate the T_{COOL} values. This is currently not possible, since many monitoring and data quality tools depends on the standards. Moreover, the proposed Timing Monitor can quite easily suffice for this difference and it is able to detect possible setting failures as shown in Section 6.3.

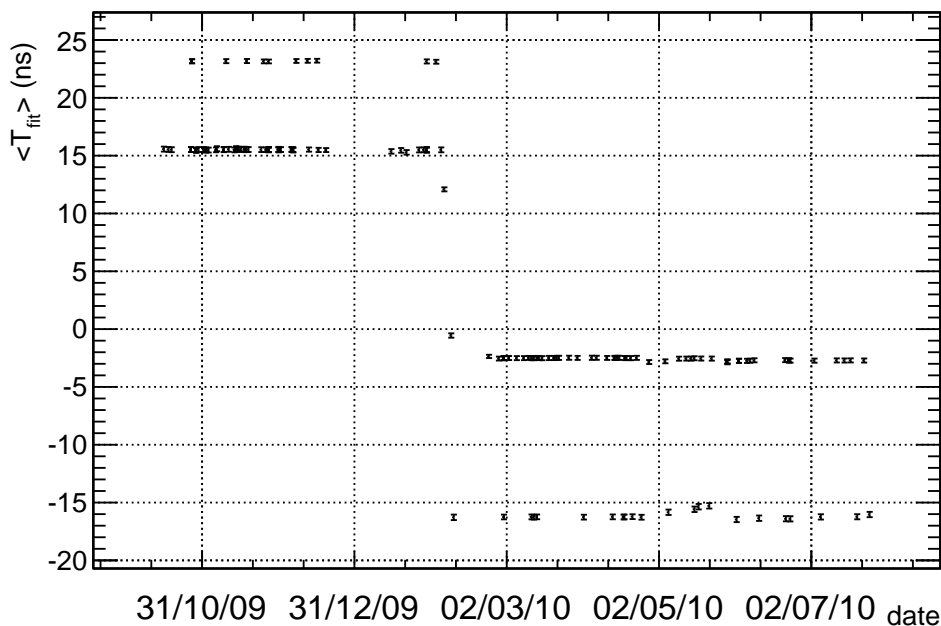


Figure 6.6: Example of a time monitor for a very strange channel; apart the *dskew2* update before March, some abnormal time structure is evident. It is peculiar that the jump are always in the same direction and always of the same amount. The used events are not bad-flagged ones.

Three large lapses of time are easily seen because of the coherent drifts at the end of February and at the beginning of May. Such large vertical gaps are both due to updates in the hardware settings (the *dskew2* and the *clock40des2* described in Section 3.3.3), after which the sampling time had been shifted: in February the sampling time has been advanced, while in May it has been delayed. The effect on T_{fit} is a consistent shift first towards negative timings, and then towards positive ones. The *dskew2* updates are applied to a whole Digitizer, and it is consistently seen for all its six channels. Therefore, it can be said quite safely that the timing for the channel in Figure 6.5 is stable.

Figure 6.6 is an equivalent Timing Monitor for another channel. Here again a *dskew2* update had taken part in the timing drift before March, but the most remarkable effect is a sort mis-timing that happens from time to time.

Two observations are important for this plot: the first is that if it is accepted that the most populated lines refer to the true values of T_{fit} , than the observed T_{fit} drift is always of the same amount, and it is always in the same direction. The second observation is that no evident flags (such as read-out errors or wrong settings) or requests on the MonoCis entries are able to cut off this kind of events, which therefore appear as completely standard events.

Such a strange behavior is present in some channels for the entire TileCal, but it is quite a rare occasion (on average, ~ 20 channels per partitions); nonetheless, it

is important to understand this point-shifts in order not to bias the *OF-NI* reconstruction: Figure 6.4 highlights that if $T_{dsp} \neq 0$, the Optimal Filtering amplitude is different from the Fit one.

6.2.1 Quantification of TileCal timing stability

Apart for the sake of the rare occasions of Figure 6.6, it may be anyway interesting to have a global view of the stability of the timing settings. In this respect two quantities can be extracted from all the Timing Monitor plots like the ones of Figure 6.5 and 6.6: the *global stability* and the *global scatter*.

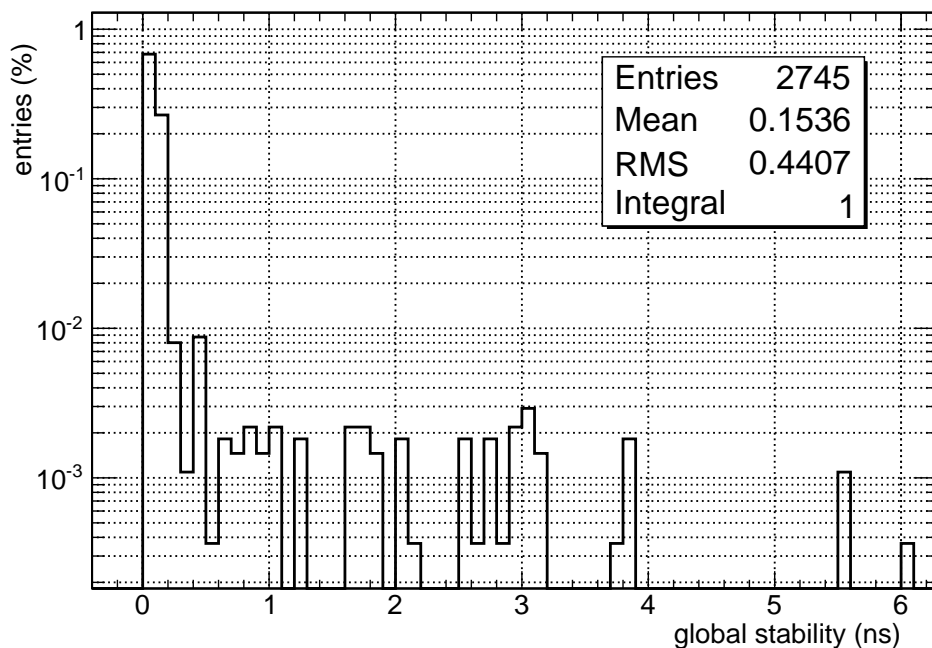


Figure 6.7: The global stability variable distribution for the LBA partition; the distribution is normalized to the number of entries. About 95% of channels are stable (in the sense described in the text) within 200 ps.

The first measurement is an estimate of the stability for all the channels in one partition. For a single channel, the stability can be defined as the distance of T_{fit} from the expected value T_{COOL} : the smaller the distance, the more stable the channel. Since the monitor is supposed to use more than one run, for each channel a distribution of the distances $d \doteq T_{fit} - T_{COOL}$ is built. The mean value of the distribution is the mean distance for that channel, while the distribution RMS is a measure of the spread of differences around $\langle d \rangle$. Therefore, the less stable is a channel, the larger the distribution RMS is. The RMS of the distances is hence a good variable to appreciate the global stability for a single channel; for this reason, the RMS of the distances in one channel is called *global stability* for that channel.

Figure 6.7 is the distribution of the global stabilities for the LBA partition, where

almost all the modules have been used. The resulting distribution shows that almost all channels are stable within a few nanoseconds. To be more precise, about 95% of channels in LBA are stable within 200 picoseconds, that is, the global stabilities are less than 0.2 ns for 95% of channels.

It is important to note that the distribution in Figure 6.7 is integrated over time (about 8 months), therefore it is not susceptible to temporary instabilities. This is the same to say that if a channel behaves like the one in Figure 6.6 but just occasionally, then is marked as *stable* or *meta-stable*, because the RMS of the distances is not amplified too much.

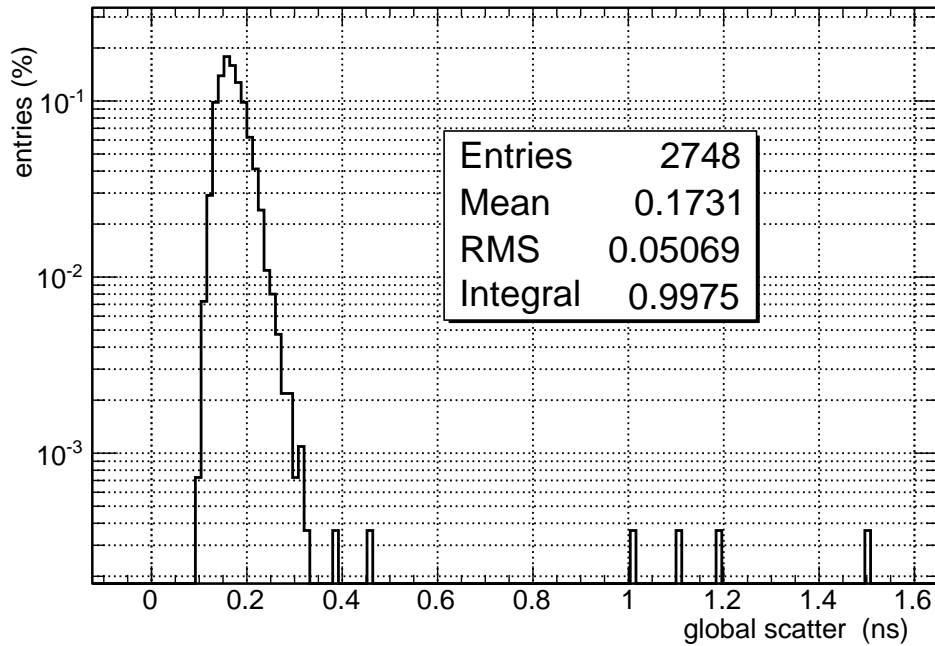


Figure 6.8: The global scatter variable distribution for the LBA partition; about 99.5% of channels are characterized by a scatter smaller than 350 ps, but minor entries are well above 3 ns.

The second variable studied to control the timing settings is called *global scatter*, and it is built in a similar way to the global stability. For each channel the distribution of $\text{RMS}(T_{fit})$ is taken into account. The mean value of this distribution is the mean value of the spreads in that channel, and it is large if many entries have large RMSs.

The global scatter is important, because it measures how the channel is reliable even if it is considered stable, therefore it is a sort of resolution, in the sense that it measures the spread of the timings.

Figure 6.8 shows the distribution of the global scatter variables for almost all the LBA partition. On average the LBA channels have a T_{fit} spread of about 0.17 ns, and 95% of channels are characterized by a global scatter of less than 350 ps. It is also important to highlight that some channels have very large RMSs, even more than 3 ns; they are not channels like the one in Figure 6.6, and these large RMSs

have been observed also on Physics and Laser runs.

Again it is important to note that the global scatter too is a variable that is integrated over time, therefore it is sensitive to eventual trends in data and not to occasionally strange behaviors.

6.3 The Time-Line Monitor

In order to easily mark and take care of channels like the one in Figure 6.6, a different approach is also proposed to monitor the channel stability: the *Time-Line Monitor*.

In an effective way, the difference with the global stability method of Figure 6.7 is that the Time-Line Monitor is not integrated over time.

For each channel and for each run the difference between the measured T_{fit} and the expected T_{COOL}^{LG} is calculated event by event, and the residuals are summed. It is therefore easy to depict a table in which at each channel and each run corresponds the sum of residuals.

Figure 6.9 shows such a table for an LBA module, using hottest colours for largest sums, and cooler colours for smallest sums. The black colour means that no run have been taken in the corresponding date. This map allows for a lot of information. First of all, almost all channels in the module have a stable timing settings, since they are not too hot. Second, the yellow channels around channel number 30 have been fixed and the proper timings have been recovered after the *dskew2* update in February. The *dskew2* update applied only to Digitizer4 and Digitizer3, and this is the reason why immediately after the update the channels from 24 to 35 switched on. The MotherBoard timings were soon fixed 3.3.2. The first use of the Time-Line Monitor is therefore to verify the fixed and to-be-fixed channels.

The second observation concerns the flashing group of channels from 12 to 17, the whole Digitizer6. It has been verified that the flashing channels present all the same behavior of the one in Figure 6.6 (to tell the truth, Figure 6.6 is about one of the flashing channels in Figure 6.9).

Also, all the flashing channels in TileCal have shown a trend similar to the one of Figure 6.6. The Time-Line Monitor is therefore useful to detect such a behavior and to cut it off in absence of other flags.

The suggested hypothesis, still to be verified, about the flashing channels is that they do not receive a correct TTC signal 3.6, therefore they fall in a non-synchronization status. This in its turn force them to inject the CIS signal at a given standard time, different from the expected T_{COOL} . This simple explanation takes into account the fact that the shifts in Figure 6.6 are always of the same amount and always in the same direction when the sampling time is fixed. It also implies that some channels are not working properly, therefore it could be a hardware problem (of channels or even digitizers) and not simply a setting error.

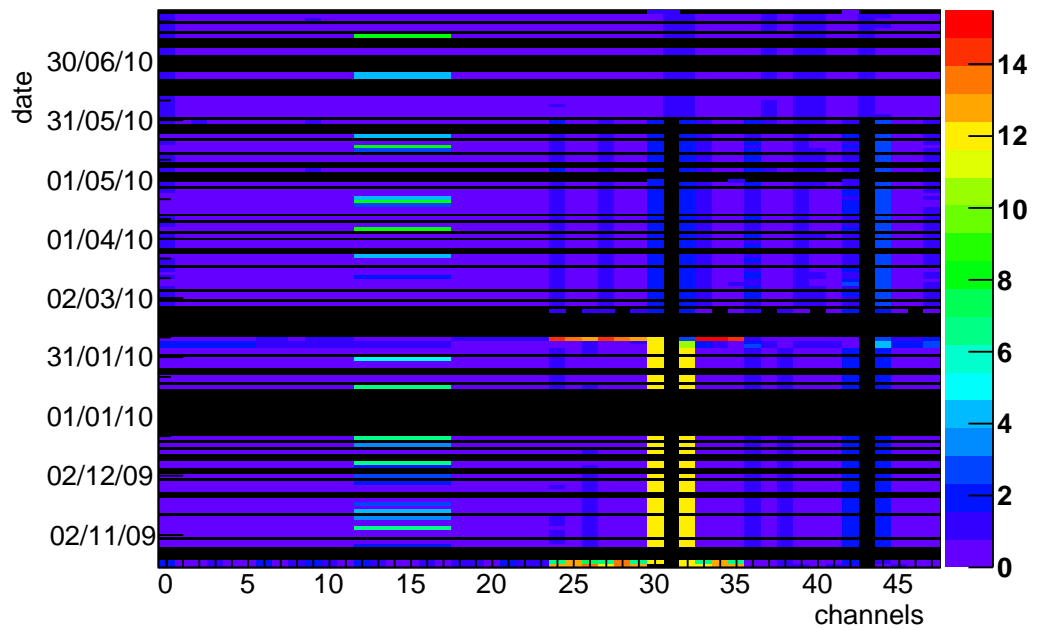


Figure 6.9: The proposed Time-Line Monitor for a module. On the vertical axis the date at which the runs have been taken; on the horizontal axis the channel number. Black entries means that no runs is available, or the channel has been masked. The hotter , the more out of time the channels are. A proper *dskew2* update is visible for channels around 30 in February; all the channels from 11 to 17, that is, the whole Digitizer6 shown the strange behavior of the channel in Figure 6.6. Such a behavior is dangerous, because it could fool the MotherBoard timing settings, and moreover seems to rely on some hardware problem.

Chapter 7

Conclusions

In current conditions (October 2010) the LHC luminosity is such that both the full data samples and the *OF-NI* reconstructed parameters can be extracted and stored. Therefore, up to now the TileCal signal has been reconstructed for monitoring purpose using the offline Fit method applied to the samples. With increasing luminosity, it will be no more possible to retrieve all the information from the RODs, and only the *OF-NI* quantities calculated online inside the DSPs will be available because of time constraints. The goal of this thesis is therefore to verify that the two methods, currently implemented assuming no correlation between samples, are equivalent using both data from proton-proton collisions and CIS events.

The first important step has been the understanding of the effects related to the hardware constraints and those due to the algorithm implementations. It has been demonstrated that the precision of the amplitude reconstruction, limited by the fixed-point arithmetic and by the maximum number of available bits in the DSPs, does not affect the precision over the whole energy range. The effect is larger at smaller charges, but it contributes with only 0.1% at 20 GeV per single channel.

Particular stress has been posed on the comparison between the amplitudes reconstructed using the Fit and the *OF-NI* methods. The first results using Physics data are encouraging, since the linearity between the two algorithms is within a few per mille; on the other hand, using the CIS data special care must be dedicated to the differences between the implementations. It has been proved that in particular the time information to be provided to the Optimal Filtering method is critical in this respect. The CIS events for which the data sample time has been optimized show that the two methods are consistent within a few per mille, but the residual differences are still to be understood.

The equivalence between the Fit and the *OF-NI* methods is fundamental, since the Calibration Factors applied for unit conversions are obtained using CIS signals reconstructed with the Fit method. Therefore, the systematics introduced by the Calibration Factors have been studied in the full energy range. The systematics introduced by the application of the Calibration Factors are a function of the injected charge; in the High Gain region, the residual difference between the Fit and the *OF-NI* methods is on average between 1% and 2% at $Q_{inj} = 1$ pC, and less than 0.3% at $Q_{inj} \geq 7$ pC; in the Low Gain region the residuals are about 0.3% at $Q_{inj} = 40$ pC and below 0.2% at higher Q_{inj} .

The last part of this work is concentrated on the importance of a good and stable

time setting. In particular, some variables useful for monitoring purpose have been analysed. As a first result, it has been verified that globally the TileCal time setting is stable over a period of about 9 months.

Moreover, some problematic channels have been isolated, but there is no sure interpretation for their behavior. The most plausible explanation is that a hardware problem in passing the time information to some Digitizers forces them to sample the signal pulses at times different from what expected, and therefore the *OF* reconstruction is completely fooled.

In conclusion, it has been demonstrated that the *OF-NI* is equivalent to the Fit method within a few per mille if good time conditions are met.

Further improvements to the understanding of the *OF* performances may be achieved by a better comparison between the algorithm implementations, especially in the low injected charge region of both gain branches. Also, being the time stability a very important issue, a more systematic study of the reconstructed T_{dsp} may help to improve the understanding of the method in its simpler implementation. Furthermore, these studies should be extended assuming correlation between data samples and thus using the complete autocorrelation matrix in the Optimal Filtering implementation.

Appendix A

Precision errors due to digit truncation

The error due to the digit truncation in representing the real numbers in machine numbers is usually called *rounding error* or *precision error*. For example, if a is a real number and \tilde{a} is its machine representation, the precision error is given by $\tilde{a} - a$. The percentage or relative precision is therefore $\epsilon_a = \frac{\tilde{a} - a}{a}$.

Using the same notations and assumptions of Section 5.2, the problem is the comparison between the online and offline amplitudes when units are changed; the offline quantities are not affected by rounding errors. The *native* units are ADC, and the offline amplitude is E^{ADC} ; the conversion in pC units is performed by means of Calibration Factors a and b : $E^{pC} = a \cdot (b + E^{ADC})$. The Calibration Factors are represented in finite-length words in look-up tables by \tilde{a} and \tilde{b} , with relative precisions ϵ_a and ϵ_b with respect to the offline quantities. In the particular example discussed in Section 5.2, b is implemented as a power of 2 with a large enough number of bits, therefore $\epsilon_b = 0$ and the $\tilde{\cdot}$ -sign is dropped in the following for b .

The offline and online quantities are therefore:

$$\begin{cases} E_{off}^{pC} &= E^{pC} &= a \cdot (b + E^{ADC}) \\ E_{on}^{pC} &= \tilde{E}^{pC} &= \tilde{a} \cdot (b + \tilde{E}^{ADC}) \end{cases}$$

From the first equation:

$$aE^{ADC} = E^{pC} - ab$$

The second equation can be rewritten as:

$$\begin{aligned} \tilde{E}^{pC} &= (1 + \epsilon_a)a [b + (1 + \epsilon_E)E^{ADC}] \\ &= -\epsilon_E(1 + \epsilon_a) \cdot ab + (1 + \epsilon_a)(1 + \epsilon_E) \cdot E^{pC} \end{aligned}$$

where the relative precisions ϵ_a and ϵ_E have been used for a and E^{ADC} respectively and the worst case, in which the rounding errors are maximal, has been considered. The online amplitude is a linear function of the offline amplitude:

$$\begin{cases} \tilde{E}^{pC} &= \alpha - \beta E^{pC} \\ \alpha &= -\epsilon_E(1 + \epsilon_a) \cdot ab \\ \beta &= -(1 + \epsilon_a)(1 + \epsilon_E) \end{cases}$$

The above relations are useful if the relative difference between E^{pC} and \tilde{E}^{pC} is considered: $z \doteq 1 - \frac{\tilde{E}^{pC}}{E^{pC}} = (1 + \beta) - \frac{\alpha}{E^{pC}}$.

In the context of Section 5.2 the \tilde{E}^{pC} and E^{pC} are random variables which depend on the injected charge, therefore it makes sense to consider the z expectation value and its error:

$$\left\{ \begin{array}{l} \langle z \rangle = (1 + \beta) - \alpha \langle \frac{1}{E^{pC}} \rangle \\ \sigma_z = |\alpha| \langle \frac{1}{E^{pC}} \rangle \cdot \sqrt{1 + \frac{\langle \frac{1}{(E^{pC})^2} \rangle}{(\langle \frac{1}{E^{pC}} \rangle)^2}} \end{array} \right.$$

The term under the square root in the σ_z expression is limited by some constant κ at higher energies ($E^{pC} \gg 1$ pC):

$$\sigma_z \leq \kappa |\alpha| \cdot \langle \frac{1}{E^{pC}} \rangle$$

Figures 5.1 and 5.2 confirm these last calculations.

If the reconstructed amplitude is very small, the above approximation does not hold anymore, and the ratio $\langle \frac{1}{(E^{pC})^2} \rangle / (\langle \frac{1}{E^{pC}} \rangle)^2$ in the σ_z square root may not be limited by a constant; this can be an explanation of the origin of the outlier points in Figure 5.3.

Bibliography

- [1] Ernest S. ABERS and Benjamin W. LEE:
Gauge Theories,
Phys. Lett. C **9**, No 1 (1973) 1 – 141.
- [2] David J. GRIFFITHS:
Introduction to Elementary particles,
John Wiley & Sons, 1987.
- [3] G. BERNARDI, M. CARENA, T. JUNK:
Higgs boson: theory and searches,
PDG review, 2010.
- [4] TEVNPH Working Group:
Combined CDF and D0 Upper Limits on Standard Model Higgs-Boson Production with up to 6.7 fb^{-1} of Data,
FERMILAB-CONF-10-257-E, 2010.
- [5] Various Authors:
The CERN Large Hadron Collider: Accelerator and Experiments, Vol 1,
Amos Breskin and Rüdiger Voss, 2009
- [6] H. WIEDEMANN:
Particle Accelerator Physics,
Springer, 2007
- [7] John D: JACKSON:
Classical Electrodynamics. Third Edition,
John Wiley & Sons, 1999.
- [8] PDG
- [9] Fabiola GIANNOTTI:
Collider Physics: LHC,
Olshevskii A., European School of High-Energy Physics, (1999)
- [10] R. K. ELLIS, W. J. STIRLING, B.R. WEBBER:
QCD and Collider Physics,
Cambridge University Press, 1996.

-
- [11] ATLAS Collaboration:
ATLAS - Letter of Intent for a General-Purpose pp Experiment at the Large Hadron Collider at CERN,
CERN/LHCC/92-4 LHCC/I 2
- [12] ATLAS Collaboration:
ATLAS Technical Proposal. Technical Design Report,
CERN, 1994
- [13] R. WIGMANS:
Calorimetry - Energy Measurement in Particle Physics
Oxford Science Publications, 2000
- [14] C. W. FABJAN and F. GIANNOTTI:
Calorimetry for particle physics
Review of Modern Physics, vol 75, Oct 2003
- [15] P. B. CUSHMAN:
Electromagnetic and Hadronic Calorimeters
Instrumentation in High Energy Physics, 1992
- [16] ATLAS/Tile Calorimeter Collaboration:
Tile Calorimeter. Technical Design Report,
CERN, 1996
- [17] ATLAS Collaboration:
The ATLAS Experiment at the CERN Large Hadron Collider,
Jinst 3 S08003, 2008
- [18] ATLAS/Level-1 Trigger Group:
Level-1 Trigger. Technical Design Report,
ATLAS TDR-12, 1998
- [19] K. ANDERSON et al.:
Design of the front-end analog electronics for the ATLAS tile calorimeter,
NIM Phys Res A 551 (2005) 469-476, 2005
- [20] S. BERGLUND et al.:
The ATLAS Tile Calorimeter digitizer,
Jinst 3 P01004, 2008
- [21] C. BOHM et al.:
ATLAS TileCal Timing,
ATL-TILECAL-2004-008, 2004
- [22] K. J. ANDERSON et al.:
Calibration of ATLAS Tile Calorimeter at Electromagnetic Scale,
ATL-TILECAL-PUB-2009-001, 2009

- [23] C CLÉMENT et al.:
Time Calibration of the ATLAS Hadronic Tile Calorimeter using the Laser System,
ATL-TILECAL-PUB-2009-003, 2009
- [24] J. A. VALERO Biot:
TileCal Read-Out Drivers Production and Firmware Production,
Master Thesis, 2007, available on web - TileCal Valencia Group
- [25] K. J. ANDERSON et al.:
Performances and Calibration of the TileCal Fast Readout Using the Charge Injection System,
ATL-TILECAL-INT-2008-002, 2008
- [26] M. Volpi, L. Fiorini, I. Korolkov:
Time inter-calibration of the TileCal/ATLAS hadronic calorimeter with the first LHC beam data,
ATL-COM-TILECAL-2009-008, 2009
- [27] B. SALVACHUA et al.:
Online energy and phase reconstruction during commissioning phase of the ATLAS Tile Calorimeter,
note waiting for approval, 2008
- [28] C. RODA, F. SARRI:
Reconstruction of the time shape of TileCal signals,
ATL-TILECAL-2003-007, 2003
- [29] F. SARRI:
Studio di un algoritmo per studiare jet di altissime energie con il calorimetro adronico di ATLAS ad LHC,
Master Thesis, available on web - TileCal Pisa Group
- [30] W. E. CLELAND, E. G. STERN:
Signal processing considerations for liquid ionization calorimeters in a high rate environment,
NIM Phys Res A 338 (1994) 467-497, 1994
- [31] B. SALVACHUA et al.:
Online energy and phase reconstruction during commissioning phase of the ATLAS Tile Calorimeter,
ATL-COM-TILECAL-2008-004, 2008
- [32] G. USAI:
Signal Reconstruction of the ATLAS Hadronic Tile Calorimeter: implementation and performance,
ATL-COM-TILECAL-2010-024, 2010
- [33] The ROOT Team:
ROOT - An Object-Oriented Data Analysis Framework,
user guide manual, available on web:
<http://root.cern.ch/drupal>